Dual-phase polycrystalline crystal plasticity model revealing the relationship between microstructural characteristics and mechanical properties in additively manufactured maraging steel

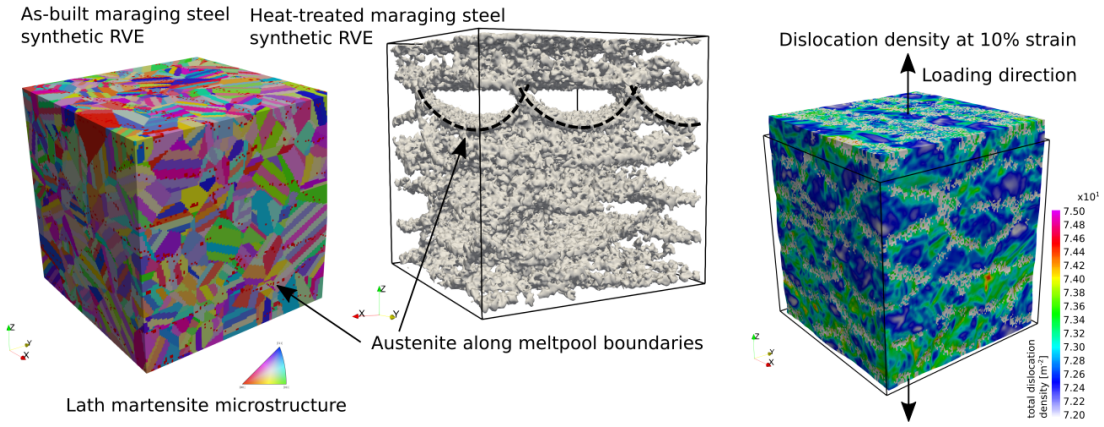
Jakub Mikula[a,*], Guglielmo Vastola[a], Zhang Yong-Wei[a]

[a]*Institute of High Performance Computing, Agency for Science, Technology and Reasearch, 1 Fusionopolis Way #16-16, Singapore 136832*

Abstract

To elucidate the relationship between microstructural characteristics and mechanical properties in additively manufactured (AM) maraging steel, this study introduces a computational approach that addresses two fundamental challenges. Firstly, it addresses the creation of representative volume elements (RVEs) that mimic the observed microstructural complexities, such as meltpool boundaries, prior austenite grains, packets and blocks of lath martensite. This is accomplished through the application of Potts Monte-Carlo methods and grain segmentation techniques in accordance with the Kurdjumov-Sachs orientation relationship. Secondly, this study develops a comprehensive crystal plasticity (CP) model encompassing both bcc and fcc plasticity. Inspired by atomistic and discrete dislocation dynamics studies, the proposed CP model incorporates characteristics intrinsic to bcc plasticity, including non-Schmid effects, dislocation and precipitate strengthening, and Hall-Petch type strengthening of elongated martensitic blocks. Utilizing the created RVEs and the proposed CP framework, finite element simulations are conducted based on an update-Lagrangian formulation. The purpose of this study is to investigate the deformation behavior, texture evolution, tension-compression asymmetry, and evolution in dislocation density in RVEs representative of as-built and heat-treated samples of maraging steel. This computational approach and its findings deepen our understanding of the intricate interplay between microstructural characteristics and mechanical properties in maraging steel and also provide valuable guidelines for refining its additive manufacturing and heat treatment processes.

Keywords: crystal plasticity, maraging steel, dislocation, simulation, additive manufacturing



Graphical abstract

*Corresponding author
Email address: jakubm@ihpc.a-star.edu.sg (Jakub Mikula)

Contents

1 Introduction **4**

2 Methods **5**

3 As-built samples of maraging steel M300 **5**

4 Synthetic RVEs of additively manufactured maraging steel **6**
4.1 Prior austenite grain microstructure . . . 7
4.2 Lath martensite . . . 8
4.3 Meltpool boundaries . . . 9
4.4 Assignment of orientation relationship . . . 10

5 Crystal plasticity model for bcc phase (martensite) **12**
5.1 Flow kinematics . . . 12
5.2 Constitutive model . . . 13
5.3 Kinetics of dislocation slip . . . 13
5.4 Slip system strength . . . 14
5.5 Slip systems . . . 16
5.6 Non-Schmid effects . . . 16
5.7 Dislocation interactions . . . 17

6 Crystal plasticity model for fcc phase (austenite) **17**

7 Summary of material parameters **18**

8 Simulations of mechanical loading of as-built RVEs **21**
8.1 Uniaxial loading in tension . . . 21
8.2 Tension-compression asymmetry . . . 24

9 Simulations of mechanical loading of heat treated RVEs **26**

10 Conclusions **31**

11 Acknowledgements **32**

Appendix A Kurdjumov-Sachs orientation relationship for tetragonality ratio $r = 1$. **40**

Appendix B The group $\mathcal{P}_{24}$ **41**

Appendix C Notes on rotation matrices **42**

Appendix D Notes on analytical solutions of flow stress **43**

Appendix E Recursive algorithm for grain cluster identification **44**

Appendix F Directions associated with slip systems **46**

Appendix G Fitting of non-Schmid coefficients **47**

Appendix H Numerical implementation **48**
Appendix H.1 Finite element formulation within the updated-Lagrangian framework . . . 48
Appendix H.2 Integration of the constitutive model . . . 50

Appendix I Pseudo-code for solving the governing elasto-plastic equations **52**

Appendix J Effect of temperature and strain-rate **54**

Appendix K Heat treated RVEs **55**

Notation

In this work, we denote vectors using lowercase bold symbols, such as $\boldsymbol{v}$, or occasionally represent them with arrows, as in $\vec{v}$. Second-order tensors are represented by uppercase bold symbols, like $\boldsymbol{T}$, while higher-order tensors are styled using blackboard bold font, as in $\mathbb{C}$. Tensors in Voigt notation are enclosed within curly brackets, as seen in $\{\boldsymbol{v}\}$. The dot product is defined as $\boldsymbol{u} \cdot \boldsymbol{v} = u_i v_i$, and the double contraction is expressed as $\boldsymbol{A} : \boldsymbol{B} = A_{ij} B_{ij}$. The dyadic (tensor) product is denoted by $\boldsymbol{u} \otimes \boldsymbol{v} = u_i v_j$. The average over volume is indicated by $\langle \boldsymbol{v} \rangle = \frac{1}{V} \int_V \boldsymbol{v}(\vec{x}) dV$. The time derivative is denoted by a dot, as in $\dot{\boldsymbol{v}} = \frac{\partial \boldsymbol{v}}{\partial t}$, while the spatial derivative is explicitly written as $\frac{\partial}{\partial \boldsymbol{X}}$ with respect to the material coordinate or $\frac{\partial}{\partial \boldsymbol{x}}$ with respect to the spatial coordinate. The operator for the generalized derivative in terms of gradient is represented by $\boldsymbol{\nabla}_0$ with respect to the material coordinate and $\boldsymbol{\nabla}$ with respect to the spatial coordinate. $\boldsymbol{I}$ is reserved for the identity matrix.

1. Introduction

Maraging steel is a low carbon steel renowned for its exceptional mechanical properties, primarily deriving its strength from a martensitic matrix comprising Fe-Ni laths interspersed with intermetallic nano-sized precipitates (Hall et al., 1968). This distinctive blend of martensite formation ("-mar") and aging ("-aging") yields the extraordinary mechanical strength, often exceeding 2GPa. Furthermore, the highly dislocated and precipitated martensitic body-centered cubic phase (bcc) may be endowed with austenitic face-centered cubic phase (fcc) where under certain conditions such system can yield both high strength and high ductility (Raabe et al., 2009a), (Raabe et al., 2009b), (Kwiatkowski da Silva et al., 2022). Such combination creates a complex multi-phase system with intricate hierarchical microstructure spanning multiple lengthscales presenting exciting prospects for tailoring the mechanical properties for desired industry application.

From a manufacturing perspective, the appeal of maraging steel lies in its weldability, attributed to its low carbon content and thus its printability (Jägle et al., 2017), (Takata et al., 2023), (Zhao et al., 2022), enabling the production of complex near-net shape components with applications in aerospace, tooling, and structural industries (Kizhakkinan et al., 2023). Maraging steel has been successfully printed using various technologies, including Powder Bed Fusion (PBF), Directed Energy Deposition (DED), and Wire Arc Additive Manufacturing (WAAM), as reviewed by (Guo et al., 2022). Comprehensive reviews on additive manufacturing (AM) of maraging steel have been also presented by (Bajaj et al., 2020), (Fayazfar et al., 2018), and more recently by (Kizhakkinan et al., 2023). Additionally, components made of additively manufactured maraging steel have demonstrated properties of the same or even higher quality than those produced using conventional methods (Kempen et al., 2011), adding to the material's significant potential. However, establishing the relationship between process, microstructure, and property poses a significant challenge, impeding the wider adoption of this material. This difficulty stems primarily from the intricate multi-phase microstructure, whose various aspects are challenging to explore through experimentation alone and require more in-depth simulation tools.

The complexity of steel may result into various pathways of martensitic phase transformation (Liu et al., 2023). Additively manufactured maraging steel exhibits the formation of a unique microstructure characterized by lath martensite (typical of low carbon steels (Morito et al., 2003), (Morito et al., 2006)), augmented with unique attributes inherent to the AM process. This involve mainly (1) the absence of precipitates in the as-built state when manufactured through PFB, while some precipitation may be observed in DED or WAAM (Mooney et al., 2019); (2) Small volume fraction of retained austenite typically observed in dendritic regions, cellular structures, or along meltpool boundaries (Bai et al., 2019), (Jägle et al., 2017) with austenitic grains growing along the $\langle 100 \rangle$ direction aligned with the maximum thermal gradients; (3) Unlike in other materials, studies on plastic anisotropy reveal no significant texture or directionality regardless of the process parameters (Mooney et al., 2019), (Zhao et al., 2022), (Kannan and Nandwana, 2022).

Understanding the process of plastic deformation in such systems would require a multiscale modelling approach (Liu et al., 2020) tackling the complex microstructure in addition to the peculiar phenomena driving plasticity in bcc metals, typically associated with the complex non-planar cores of screw dislocations resulting into the breakdown of Schmid's law (Gröger et al., 2008a). Recent advancements in AM have brought forth intricate microstructures featuring nano-sized precipitates, where crystal plasticity models have emerged as valuable tools in examining the mechanical response in nickel-based superalloys (Xi et al., 2023), (Ghorbanpour et al., 2017), (Ghorbanpour et al., 2020) stainless steels (Lindroos et al., 2022), (Hu et al., 2024), or titanium alloys (Liu et al., 2020), (Pinz et al., 2022), with very few studies covering lath-martensitic steels.

While significant efforts have been devoted to crystal plasticity modelling of fcc steels (Motaman et al., 2020), (Eghtesad and Knezevic, 2020), little work currently focuses on bcc steels. Initial crystal plasticity work on single crystals of bcc α-iron was presented by (Yalcinkaya et al., 2008), (Koester et al., 2012), (Narayanan et al., 2014), (Patra et al., 2014) all comparing results to the experimental data by (Keh, 1965). A crystal plasticity model of bcc polycrystals considering non-Schmid effects was presented by (Savage et al., 2017). A plasticity model for a dual-phase steel has been recently proposed utilizing the self-consistent polycrystal homogenization (Daroju et al., 2022). Plasticity models for low carbon steels considering the lath martensite microstructure have been recently presented by (Schäfer et al., 2019), (Gallardo-Basile et al., 2021), and more

recently by (Fischer et al., 2023), focusing on cyclic deformations and the analysis of the power-law kinetics. These studies, however, do not consider the effects associated with non-planar dislocation cores, dislocation interactions, precipitates, or dislocation pile-up at martensitic block boundaries. A comprehensive model for lath martensite microstructure informed by atomistic simulations, capturing important aspects of bcc plasticity, and featuring inherent properties of AM is lacking. Therefore, the objective of this study is to provide a framework for additively manufactured maraging steel (specifically M300, M350 grades), a material garnering significant attention in PBF process, involving synthetic RVEs for both as-built and heat-treated samples. Development of such framework has also relevance as a key component of integrated multiscale modelling, such as (Mikula et al., 2021).

The paper is organized as follows: In Sec.2, we briefly introduce the methods used in this work. In Sec.3, we introduce the characteristic microstructure of maraging steel produced through additive manufacturing, highlighting the presence of lath martensite and small austenitic grains along the meltpool boundaries. Moving on to Sec.4, we elaborate on a methodology designed to generate synthetic Representative Volume Elements (RVEs) that closely mimic experimental observations, employing segmentation methods and a Monte Carlo approach. In Sec.5 and Sec.6, we present the governing equations for the updated-Lagrangian finite element crystal plasticity model, focusing on the martensite and austenite phases, respectively. Material properties utilized in the simulations are summarized in Sec.7. Subsequently, Sec.8 encompasses the presentation and discussion of simulation results for as-built samples, while Sec.9 is dedicated to the simulation results and discussion of heat-treated samples. A concise conclusion in Sec.10 is succeeded by several appendices incorporating more detailed derivations and algorithms.

2. Methods

All simulations were conducted using an in-house C++ code, which implements a finite element crystal plasticity model developed within a finite strain updated-Lagrangian framework. The C++ code is constructed in connection with several existing open-source libraries, namely VTK (Schroeder et al., 2006), Trilinos (Trilinos Project Team), utilized as an iterative solver for solving a linear system of equations, and Eigen3 (Guennebaud et al., 2010) for matrix and vector operations. Data visualization is performed using Paraview 5.10.0. Color mapping of orientation fields is achieved through the use of an open-source utility MTEX (Nolze and Hielscher, 2016). The theoretical background is provided in the following sections. Pseudo-code of various subroutines is presented in Appendix. All simulations were conducted on a computer cluster with 8 nodes each consisting of *Intel 8268 48-Cores@2.9*. The total simulation time up to 10% of strain took 72 hours for one RVE.

3. As-built samples of maraging steel M300

Motivated by recent experimental investigations into additively manufactured maraging steels, we aim to delineate the key characteristic features essential for the construction of synthetic Representative Volume Elements (RVEs) used in the simulation. To illustrate, in Fig.1 we showcase the results presented by (Takata et al., 2018); with analogous findings reported by (Chadha et al., 2020), (Tan et al., 2018), and (Wei et al., 2022).

Experimental observations reveal that additively manufactured maraging steel comprises of a large volume fraction of martensite, likely attributed to the rapid cooling rates inherent to the manufacturing process (Jägle et al., 2014), (Kempen et al., 2011), (Mooney et al., 2019), (Vishwakarma et al., 2020). Notably, it is discerned that the martensite evolves into a lath martensite microstructure (Maki, 2012), a pattern commonly observed in low-carbon steels (Morito et al., 2003), (Morito et al., 2006), (Kitahara et al., 2006). This intricate microstructure exhibits a highly hierarchical arrangement spanning various length scales, from prior austenite grains to packets, blocks, and martensitic laths, with specific crystallographic orientations, often adhering to the Kurdjumov-Sachs (Kurdjumow and Sachs, 1930) or Nishiyama-Wasserman (Nishiyama, 1934), (Wassermann, 1935) orientation relationship.

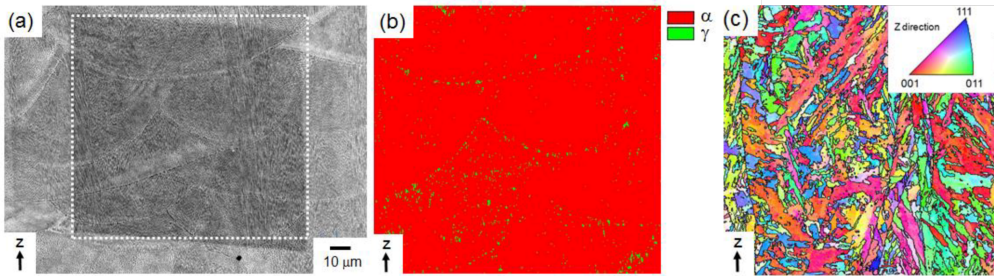


Figure 1: Experimental observation of the SLM fabricated microstructure of maraging steel by (Takata et al., 2018) depicting (a) meltpool boundaries, (b) small austenitic grains along the meltpool boundaries, and (c) lath martensite microstructure. (Reused under an open access Creative Common CC BY license).

Additionally, the microstructure of additively manufactured maraging steel, as revealed by Electron Backscatter Diffraction (EBSD) analysis in Fig.1 unveils a small volume fraction of austenitic grains along the meltpool boundaries. This relationship is clearly visible when comparing Fig.1(a) with Fig.1(b). Intriguingly, it has been reported that all austenitic grains exhibit an orientation along $\langle 001 \rangle$ in alignment with the build direction. Analogous traces of austenite have been reported by (Mutua et al., 2018), while other studies noted a significant presence of retained austenite in interdendritic regions (Jägle et al., 2017). Hypotheses have been proposed regarding the existence of thin films of austenite between individual martensitic laths (Maresca, 2015), (Maresca et al., 2014); however, this surpasses the resolution and objectives presented in this study. The complex martensite microstructure emerges in Fig.1(c) where it is also observed that the individual crystals have no dominant orientation (Takata et al., 2018).
In summary, the key characteristic features of interest to this work which are modelled explicitly are the lath martensite microstructure (considering prior austenite grains, packets and blocks of martensite) and meltpool boundary austenite. In the subsequent section, we outline a set of algorithms for generating synthetic three-dimensional RVEs that emulate the experimental observations depicted in Fig.1.

4. Synthetic RVEs of additively manufactured maraging steel

Motivated by the experimental observations of the intricate microstructure consisting of lath martensite and the complex features inherent to additive manufacturing of maraging steel, we have devised a set of algorithms for the generation of synthetic Representative Volume Elements (RVEs) used for the purpose of full field finite element crystal plasticity simulation. Below we detail the individual algorithms, while we also note that similar features of such synthetic RVEs may generated through existing software such as DREAM.3D (Groeber and Jackson, 2014) or Neper (Quey and Kasemer, 2022).
The overall methodology of generating the synthetic RVEs involves initially creating a prior austenite grain microstructure, which is subsequently segmented into packets and blocks of martensite. In this work, the block is considered the smallest explicitly resolved microstructural feature. Following this, a meltpool RVE is generated, serving as a template for seeding small austenitic grains along the meltpool boundaries. Finally the proper orientation relationship between austenite and martensite is assigned. The parameters associated with each microstructural feature are obtained from the literature. Table 1 compiles some typical SLM conditions proven effective for printing maraging steel, along with the characteristic length-scales developed during the printing process.
Drawing from the collected data, we pinpoint the following printing conditions for fabricating the synthetic meltpool RVE that are discussed in the subsequent subsections: hatch spacing (h) of 82.5μm, rotation angle of scan pattern ($\Delta\theta$) of 67°, layer height (w) of 30μm, and cylinder (meltpool) radius (r) of 62.5μm. The average prior austenite grain size is chosen at 35μm and the dimensions of the RVE are specified as $200 \times 200 \times 200\mu\text{m}^3$ that is also approximately ⅔ of the size depicted in Fig.1. In additive manufacturing, density of maraging steel depends on process parameters. However, a relatively large process parameter window can be identified where a high-density steel can be manufactured (Mutua et al., 2018). Throughout

Table 1: Typical process parameters and characteristic length-scales of 3D printed maraging steel available in the literature. Default values selected for the purpose of generating the simulation RVEs are shown in the third column (*default simulation RVE).

Parameter	Value (literature)	Value*	Unit
Prior austenite grain size	20-50 (Suryawanshi et al., 2017)	35	μm
Volume fraction of retained austenite	Fig.1 (Takata et al., 2018)	$\sim$2.1	%
Meltpool size	$\sim$50 -100 (Takata et al., 2018)	$r = 62.5$	μm
Lath width	200 (Takata et al., 2018)	-	nm
Block size	$0.067 \times 20 = 1.4$ (Galindo-Nava et al., 2016), 0.5-3 (Suryawanshi et al., 2017)	2.0	μm
Hatch spacing	50-150 (Tan et al., 2018), 105 (Suryawanshi et al., 2017), 140 (Casalino et al., 2015)	82.5	μm
Layer thickness	30 (Takata et al., 2018), (Casalino et al., 2015), (Suryawanshi et al., 2017), 50 (Chadha et al., 2020), 40 (Tan et al., 2018)	30	μm
Printing strategy	90 (Takata et al., 2018), (Suryawanshi et al., 2017), 50 (Chadha et al., 2020), 67 (Tan et al., 2018),	67	$^\circ$

the manuscript we consider this to be the case and we neglect the properties associated with porosity, while directing readers to other relevant studies that have investigated correlations between porosity and mechanical response (Mutua et al., 2018), (Kempen et al., 2011), (Bhardwaj and Shukla, 2018) or even provided corrective mechanisms (Demir and Previtali, 2017) to achieve high density maraging steel.

4.1. Prior austenite grain microstructure

The initial phase of fabricating the simulation RVEs involves the generation of the prior austenite grain microstructure which is then segmented into martensite. To achieve a more authentic representation of grains, we employed a Potts Monte Carlo method (Holm and Battaile, 2001), (Miodownik, 2007). This model offers the advantage of producing grains with a more realistic appearance compared to a Voronoi tessellation, while also remaining computationally manageable and easy to implement. While the method can provide fundamental insights into the evolution of grains in a polycrystal (Miodownik, 2007), in our work, it is used purely as a design tool for generating synthetic RVEs.

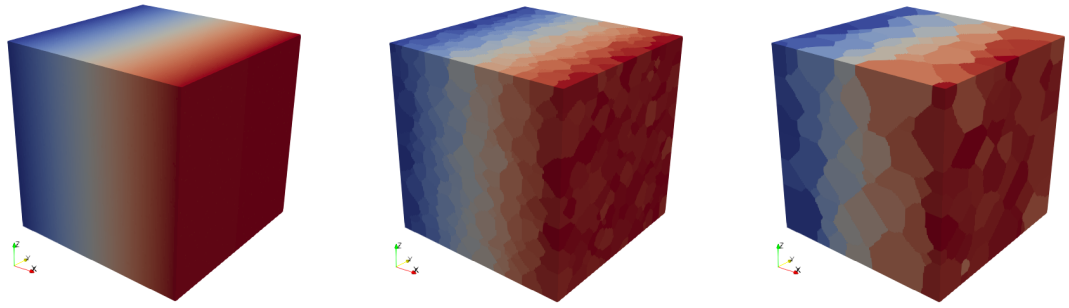
Monte-carlo methods operate on a structured grid of cells. The Potts Hamiltonian H that defines the total energy of the system can be expressed in the form

$$H = \sum_{i=1}^{N} \left\{ \sum_{j=1}^{n} \frac{\gamma(s_i, s_j)}{2} + F(s_i) \right\}, \tag{1}$$

where γ is related to grain boundary energy, specifically the interface energy between the two cells s_i and s_j, while F is related to the bulk chemical energy of the cell s_i. At every iteration, a random cell is selected and the state of the cell is changed to one of the unlike neighbours. The change in the total energy associated with this change is calculated $\Delta E = H(t) - H(t-1)$, where $H(t-1)$ is the Hamiltonian from the previous time step. The probability of retaining this new state (which can be here interpreted as a crystal orientation) can be specified by

$$P = \frac{p_0}{2} \left[1 - \tanh\left(\frac{\Delta E}{2kT} \right) \right], \tag{2}$$

where k is the Boltzmann constant, p_0 is related to the grain boundary mobility, and T is the temperature. ΔE is the energy associated with the reorientation of the cell from one state to another. As our model serves purely as a design tool for generating isotropic single-phase grain microstructures, the parameter choices are exclusively numerical. Our objective herein does not involve modelling grain growth. The following set of parameters were identified to capture the grain growth process: $p_0 = 1$, $T = 300$K, $\gamma = 10^{-20}$J, $k = 1.38 \cdot 10^{-23}$J/K. The choice of these parameters was decided through a trial and error exercise to achieve visually appealing RVEs such as presented in (Holm and Battaile, 2001) in a unit cube RVE of 128^3 cells. With this choice, the snapshots of the simulation evolving in time are presented in Fig.2.



(a) 128^3 grains at time t_0. (b) 2617 grains at time $t_1 > t_0$. (c) 565 grains at time $t_2 > t_1$.

Figure 2: Snaphots of the monte-carlo simulation for obtaining the prior austenite grain microstructure. Each grain index is assigned a random lattice orientation defined by a set of three Euler angles (see Eq.3).

In the initial configuration, as depicted in Fig.2(a), each cell is assigned a unique index from 1 (blue color) to 128^3 (red color). Over time, these cells undergo state reassignments based on the probabilities defined in Eq.2, resulting in a system that forms clusters and physically exhibits a resemblance to an equiaxed grain microstructure. The evolution continues as seen in Fig.2(b) and (c) until an adequate average grain size d is achieved. Having considered isotropic γ, the morphology remain equiaxed, while the grain growth rate is proportional to t^n, requiring more computational time for obtaining larger grain microstructures. The average grain size is easily quantified by counting the number of cells with the same index, and converting it into a diameter of a sphere with an equivalent volume. The final prior austenite grain microstructure is presented in Fig.3(a) where prior austenite grain boundaries are outlined in black.

Subsequently, random orientations are assigned to each grain cluster using a set of Euler angles (ϕ, θ, ψ). It is important to note that random Euler angles do not yield random orientations (Miles, 1965). Therefore, to obtain truly random crystal lattice orientations, the Euler angles (ϕ, θ, ψ) are generated according to

$$\begin{aligned} \phi &= 2\pi i \\ \theta &= \text{acos}(2j - 1), \\ \psi &= 2\pi k \end{aligned} \tag{3}$$

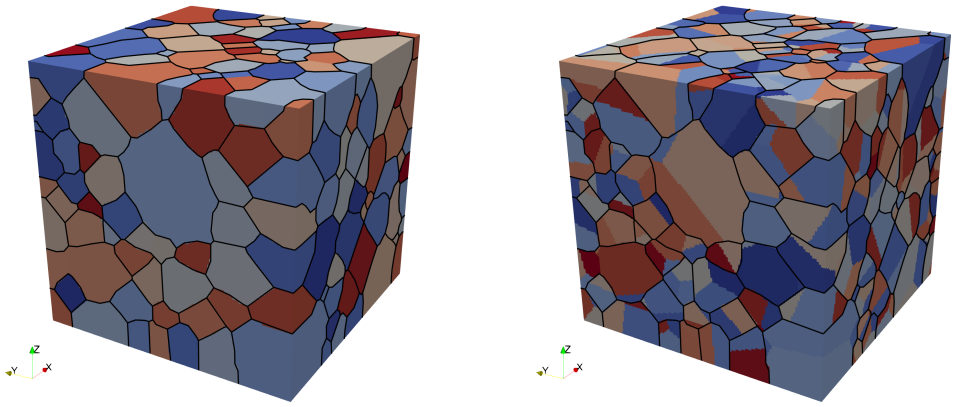
where i, j, and k are real numbers randomly picked from the (0,1) interval.

The generated prior austenite grain RVE serves as a foundational structure for subsequent segmentation into lath martensite.

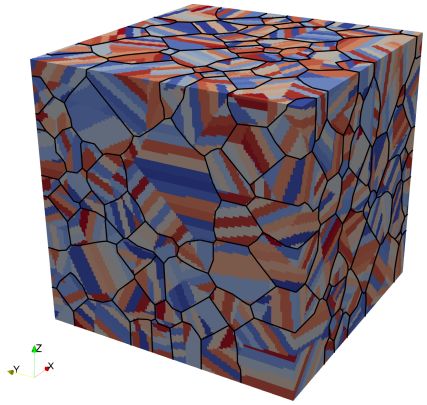
4.2. Lath martensite

Maraging steels exhibit a lath martensite microstructure - a characteristic feature shared with low carbon steels. A prior austenite grain transforms into a hierarchical pattern consisting of four packets of variants sharing the same habit plane, each with six possible martensitic variants sharing a common axis of lattice distortion (Kitahara et al., 2006). The blocks can be further subdivided into laths which are in the form of elongated structures with a very similar lattice orientation. In this work, we consider blocks to be the smallest explicitly resolved microstructural features. Segmentation of the synthetic RVE is presented in Fig.3.

Generating the martensite microstructure involves a segmentation procedure applied to the prior austenite grains presented in Fig.3(a). In this figure, each grain is assigned a random color. Similarly to (Schäfer et al., 2019), (Gallardo-Basile et al., 2021), the volume of each prior austenite grain depicted in Fig.3(a) is divided into three packets $\Omega_\gamma = U_{p=1}^{3} \Omega_p$ of a similar volume. Each packet is assigned a unique index and one of the planes $\{(111), (\bar{1}11), (1\bar{1}1), (11\bar{1})\}$ picked by random. Algorithmically, the subdivision operates such



(a) Prior austenite grain RVE consisting of 161 grains. (b) Martensite packet RVE consisting of 482 packets.



(c) Martensite block RVE consisting of 3106 blocks.

Figure 3: Grain, packet and block RVE with random asignment of unique index to each cluster. Prior austenite grain boundaries are outlined in black.

that first the centre of the grain $\vec{x}_c^g$ is identified as $\vec{x}_c = \frac{\sum \vec{x}_{s_i}^g}{n^g}$, where n^g is the number of cells belonging to grain g, and $\vec{x}$ represents the position vector of each cell of the grain with respect to a fixed coordinate system. Three planes are then drawn from the centre of the grain at an angle of 120° creating three volumes (packets) of approximately equal size, in line with the findings stating $d_{packet} \approx 0.4 D_g$ (Galindo-Nava et al., 2016). The result of this segmentation is illustrated in Fig.3(b). Each packet is subsequently subdivided into blocks of martensite by drawing parallel planes separated by the block size. Each segmented volume is assigned a unique index, as shown in Fig.3(c). Approximately 15 laths per grain, as reported by (Galindo-Nava et al., 2016), further characterize this segmented microstructure. The resultant RVE consists of 161 grains, 482 packets, and 3016 blocks.

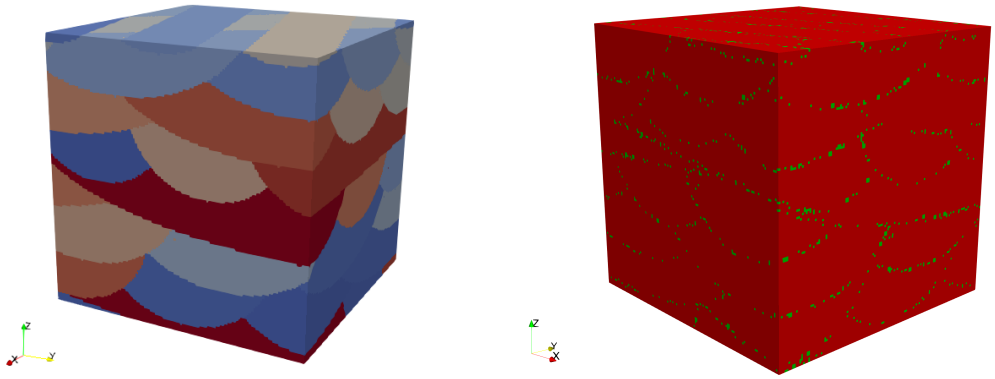
4.3. Meltpool boundaries

In the Powder Bed Fusion (PBF) process, a near-net shape component is fabricated by a sequential deposition of layers of powder which are each selectively melted using a focused laser beam. The printing sequence is typically divided into stripes, each consisting of multiple line vectors separated by the distance of hatch

spacing h. The scan strategy undergoes a rotation of these lines with each successive layer by a certain angle.

A distinctive microstructural feature of PBF is the formation of meltpool boundaries, resembling overlapping semi-cylinders. Notably, in the case of maraging steel, these meltpool boundaries serve as sites for retaining the austenite in the form of small grains with a $\langle 001 \rangle$ orientation (refer to Fig.1).

To incorporate the meltpool boundaries within the simulation RVE, a simple algorithm is devised: First a uniform pattern of line segments evenly spaced by the distance of hatch spacing h is created and attributed with the first layer. This pattern is duplicated by shifting it along the build direction by the distance of layer thickness w and incrementally rotated by an angle $\Delta\theta$ with each layer shift. This establishes the line segments of the printing strategy within the volume of the RVE. Subsequently, a cylinder is projected on the the volume of the RVE with its axis aligned with one of the line segments. The cells of the RVE within the cylinder are then assigned a unique index. As the cylinder transverses from the first to the last line segment following the direction of moving heat source (scan vector), individual volumes of meltpool are identified. The resulting meltpool RVE is depicted in Fig.4(a) and was generated using the specific parameters outlined in Table 1, such as a hatch spacing of $h = 82.5\mu$m , layer thickness $w = 30\mu$m, scan strategy rotation angle $\Delta\theta = 67°$, and a cylinder radius $r = 62.5\mu$m. The colors in the figure are assigned randomly to each index to better visualize each meltpool.



(a) Meltpools for a given hatch scan strategy, each represented by a different color.

(b) Dual-phase RVE with the martensite phase (red) and the austenite phase (green) in the form of small grains along the meltpool boundaries. Colors are assigned to match Fig.1(b).

Figure 4: Synthetic RVEs of meltpool and meltpool boundaries for a given set of process parameters (see Table 1). Build direction is along the z coordinate.

Meltpool boundaries can be now easily identified as the cells which neighbor cells of a different meltpool index. The state of the boundary cell is switched from martensite into austenite with the chosen probability of $P = 20\%$ wich was devised through a trial and error exercise to visually match Fig.1(b). This creates a dual-phase RVE presented in Fig.4(b), with color-coding corresponding to Fig.1(b): red for the martensitic bcc phase and green for the austenitic fcc phase.

4.4. Assignment of orientation relationship

To complete the RVE setup, correct orientation relationship needs to be applied to individual blocks, in this case respecting the Kurdjumov-Sachs (KS) orientation relationship (Kurdjumow and Sachs, 1930). The pole figures and the inverse pole figure of an individual prior austenite grain with its martensitic variants is presented in Fig.5.

Following the KS orientation relationship, 24 martensitic variants can be identified belonging to four packets sharing the same habit plane. Each packet in Fig.5 is assigned a different color and each martensitic variant

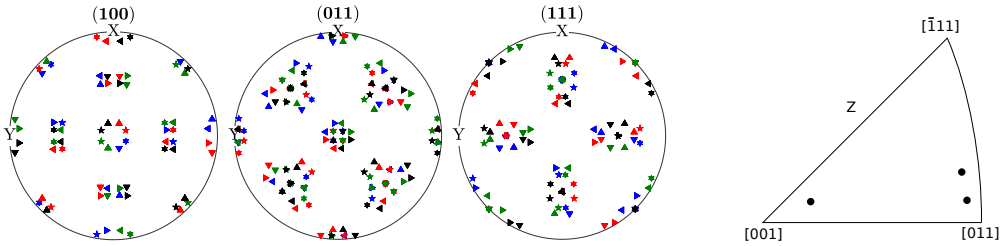


Figure 5: Pole figures and inverse pole figure of the 24 martensitic variants within an austenitic grain assuming the tetragonality ratio $r = 1$. The four packets are each colored differently, while the individual variants of the packet are indicated using different symbols.

of the packet is assigned a unique marker shape. The generation of rotation matrices for each variant follows the work by (Koumatos and Muehlemann, 2017) and the algorithm details following the case with the tetragonality ratio $r = 1$ are presented in Appendix A.

The lattice orientation is assigned to each variant within the local coordinate system based on the packet and block index adhering to KS orientation relationship. This orientation is then mapped onto the prior austenite grain microstructure depicted in Fig.3(a) with a random assignment of Euler angles (see Eq.3). This is achieved through matrix multiplication $\boldsymbol{R} = \boldsymbol{R}_b\boldsymbol{R}_g$, where $\boldsymbol{R}_g$ is the rotation matrix of the prior austenite grain g and $\boldsymbol{R}_b$ is the calculated rotation matrix of block b with respect to the grain (see Appendix A). The resultant RVE is presented in Fig.6 with the colorcoding indicating the lattice orientation given by the stereographic triangle. Color mapping has been achieved through the use of an open-source utility MTEX written in Matlab (Nolze and Hielscher, 2016). The physical size of the RVE is $200^3 \mu\text{m}^3$ and the structured finite element mesh consists of 128^3 ($\sim 2.1{\cdot}10^6$) elements. Notice that the retained austenite can be recognized alongside with the meltpool boundaries having the $\langle 001 \rangle$ (red) orientation.

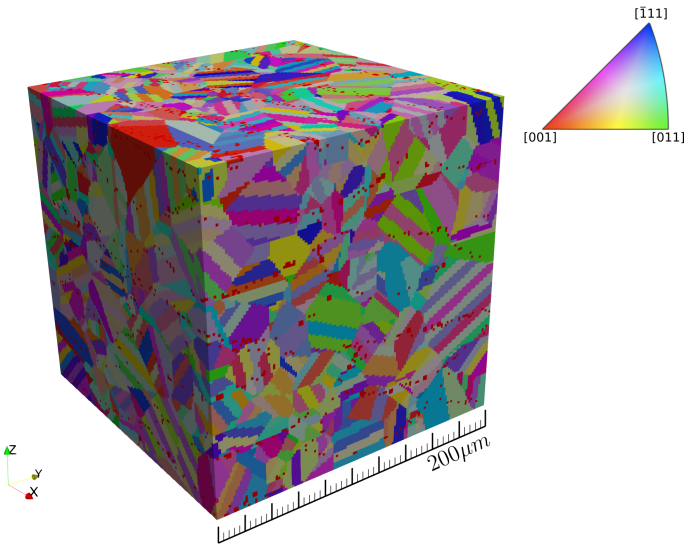


Figure 6: Martensite RVE with the Kurdjumov-Sachs orientation relationship interspersed with small austenitic grains along the meltpool boundaries with the orientation of $\langle 001 \rangle$ along the build direction. The physical size of the RVE is 200^3 μm^3 while the structured finite element mesh consists of 128^3 elements. Build direction is along the z coordinate.

The proposed methodology is applicable to any low-carbon steel exhibiting the lath-martensite microstructure. Various aspects of this microstructure can be tailored through adjustments in the block size, packet size, prior austenite grain size, precipitate volume fraction and size or the volume fraction of reverted

austenite (discussed in Sec.9). Minor adjustments will be needed if different orientation relationship is to be applied, for instance Nishiyama-Wasserman.
The presented RVEs are employed in connection with the crystal plasticity model discussed in the subsequent section to explore various aspects of plastic deformation. In this study we focus solely on plastic deformation and do not consider the evolution of the martensite microstructure. Addressing letter would necessitate a complex phase field model (Ahluwalia et al., 2020), which is beyond the scope of this study.

5. Crystal plasticity model for bcc phase (martensite)

In this section, we detail the governing equations devised for the martensitic phase. The crystal structure of iron-nickel martensite is bcc as observed by XDR diffraction patterns, (Zhao et al., 2022), (Takata et al., 2023), which is similar to iron-carbon steels where the tetragonality ratio tends to 1 for low carbon concentration (Hall et al., 1968). Metals with bcc crystal structures often manifest some of the most peculiar and anomalous phenomena in their dislocation plasticity (Christian, 1983). This peculiarity stems from the absence of closed-packed planes (Morsdorf et al., 2016), (Raabe, 1995), (Seeger, 2001), (Seeger, 2004) and the intricate nature of dislocation non-planar cores (Gröger and Vitek, 2005), which bring about mechanisms vastly distinct from those observed in closed-packed crystals (such as fcc or prismatic hcp slip). The following subsections establish a dislocation based temperature and rate dependent crystal plasticity model of maraging steel. In this work, properties of nickel-iron martensite are associated with those of α-iron.

5.1. Flow kinematics

We assume the multiplicative decomposition of the deformation gradient into the elastic and the plastic part in the following multiplicative order

$$\boldsymbol{F} = \boldsymbol{F}^e \boldsymbol{F}^p, \tag{4}$$

where the deformation gradient is defined by $\boldsymbol{F} = \frac{\partial \boldsymbol{x}}{\partial \boldsymbol{X}} = \boldsymbol{\nabla}_0 \boldsymbol{x}$, with the assumption that the Jacobian determinant $\det \boldsymbol{F} = J > 0$ satisfying the mass conservation law, and $\det \boldsymbol{F}^p = 1$ which makes plastic deformation volume preserving. Here, $\boldsymbol{x}$ refers to the spatial coordinate, while $\boldsymbol{X}$ refers to the material coordinate, and $\boldsymbol{\nabla}_0$ is the gradient with respect to the material coordinate.
It is assumed that the decomposition is performed such that $\boldsymbol{F}^e$ encompasses the elastic lattice distortion together with the lattice rotation while $\boldsymbol{F}^p$ describes the lattice-invariant plastic distortion.
It can be shown that the velocity gradient $\boldsymbol{L}$ can be additively decomposed into two parts

$$\boldsymbol{L} = \boldsymbol{\nabla} \dot{\boldsymbol{x}} = \dot{\boldsymbol{F}} \boldsymbol{F}^{-1} = \boldsymbol{L}^e + \boldsymbol{L}^p. \tag{5}$$

Here, $\boldsymbol{L}^e = \boldsymbol{F}^e \boldsymbol{F}^{e^{-1}}$ and $\boldsymbol{L^p} = \boldsymbol{F}^e \bar{\boldsymbol{L}}^p \boldsymbol{F}^{e^{-1}}$, where $\bar{\boldsymbol{L}}^p = \dot{\boldsymbol{F}}^p \boldsymbol{F}^{p^{-1}}$ is the plastic velocity gradient in the intermediate configuration.
It is assumed that the plastic velocity gradient $\boldsymbol{L}^p$ originates purely from the dislocation slip on a set of crystallographic planes in which case it can be expressed through a sum of the dyadic product

$$\dot{\boldsymbol{F}}^p \boldsymbol{F}^{p^{-1}} = \sum_\alpha \dot{\gamma}^\alpha \vec{m}_0^\alpha \otimes \vec{n}_0^\alpha, \tag{6}$$

where the subscript α indicates the slip system and $\vec{m}_0^\alpha$ and $\vec{n}_0^\alpha$ represent the slip plane direction and slip plane normal with respect to the reference configuration, respectively. $\dot{\gamma}^\alpha$ defines the rate of slip along the active slip system α.
With these assumptions, the deformed configuration of the slip system can be conveniently captured by the elastic deformation gradient

$$\begin{aligned} \vec{m}^\alpha &= \boldsymbol{F}^e \vec{m}_0^\alpha \\ \vec{n}^\alpha &= \boldsymbol{F}^{e^{-T}} \vec{n}_0^\alpha \end{aligned}. \tag{7}$$

5.2. Constitutive model

We introduce the free energy in the following form

$$\psi = \frac{1}{2}\boldsymbol{E}^e : \mathbb{C} : \boldsymbol{E}^e, \tag{8}$$

where $\mathbb{C}$ indicates the fourth-order tensor of elastic constants and $\boldsymbol{E}$ refers the Green-Lagrange measure of strain calculated as

$$\boldsymbol{E} = \frac{1}{2}\left(\boldsymbol{C} - \boldsymbol{I}\right), \qquad \boldsymbol{E}^e = \frac{1}{2}\left(\boldsymbol{C}^e - \boldsymbol{I}\right), \tag{9}$$

where $\boldsymbol{C} = \boldsymbol{F}^T\boldsymbol{F}$ is the Green tensor.
The constitutive model can be derived between the Green-Lagrange strain and the second Piola-Kirchhoff stress

$$\boldsymbol{S}^{\mathrm{2PK}} = \frac{\partial \psi}{\partial \boldsymbol{E}^e} = \mathbb{C} : \boldsymbol{E}^e, \tag{10}$$

where the relationship between the second Piola-Kirchhoff stress and the Cauchy stress is given by $\boldsymbol{S}^{\mathrm{2PK}} = \det\left(\boldsymbol{F}^e\right)\boldsymbol{F}^{e^{-1}}\boldsymbol{\sigma}\boldsymbol{F}^{e^{-T}}$.

5.3. Kinetics of dislocation slip

The kinetics governing the shear rate $\dot{\gamma}^\alpha$ of individual slip systems α can manifest in various forms, encompassing factors such as stress state, material condition, or temperature. In bcc metals, the principal agents of plastic flow are the screw dislocations; however, the intricate nature of the dislocation core (Gröger et al., 2008a), (Gröger et al., 2008b) imparts considerable resistance to dislocation motion. It has been established that dislocations move primarily through the mechanism of kink-pair formation (Kocks et al., 1975), (Hull and Bacon, 2011), (Tang et al., 1998), which is a thermally activated process. For that reason, the kinetics of plastic flow is described by an Arrhenius type equation in the following form

$$\dot{\gamma}^\alpha = \begin{cases} 0 & \text{if} \quad \tau^\alpha_{\mathrm{eff}} \leq 0 \\ \dot{\gamma}^\alpha_0 \exp\left\{-\frac{\Delta G}{kT}\right\} \mathrm{sign}(\tau^\alpha) & \text{if} \quad \tau^\alpha_{\mathrm{eff}} > 0 \end{cases}, \tag{11}$$

where $\dot{\gamma}^\alpha_0$ is the reference shear rate, ΔG is the activation barrier resisting the motion of dislocation through the crystal lattice, k is the Boltzmann constant, and T is temperature. The energy barrier can be reduced by stress, specifically the resolved shear stress τ^α on slip system α. Various forms of activation enthalpy ΔG have been proposed, either based on the kink-pair theory (Hirth et al., 1983), (Seeger, 1981), (Werner, 1987), (Lim et al., 2015), or an empiral fit to atomistic simulation data (Gröger and Vitek, 2008), (Gröger and Vitek, 2009), (Gröger et al., 2017). In this work a simple empiral form is chosen for its simplicity while it also allows for modification of the barrier shape

$$\Delta G = G_0\left[1 - \left(\frac{\tau^\alpha_{\mathrm{eff}}}{s^\alpha_t}\right)^p\right]^q. \tag{12}$$

Here, the coefficients p and q are empirical ($0 \leq p \leq 1$, $1 \leq q \leq 2$), and describe the shape of the barrier obstructing the dislocation motion. As revealed by atomistic simulations, not only the glide component of the stress tensor but also components distorting the dislocation core affect dislocation's resistance to motion (Gröger et al., 2008b), (Gröger and Vitek, 2020). For that reason an effective non-Schmid yield criterion $\tau^\alpha_\eta \leq \tau_{cr}$ needs to be proposed. The most general form can be written following (Dao and Asaro, 1993), (Qin and Bassani, 1992)

$$\tau^\alpha_\eta = \tau^\alpha + \boldsymbol{\eta}^\alpha : \boldsymbol{\sigma}, \tag{13}$$

where τ^α is the resolved shear stress, $\boldsymbol{\eta}^\alpha$ is a second-order tensor which coefficients are related to the non-Schmid effects and $\boldsymbol{\sigma}$ is a stress tensor. The specific form of $\boldsymbol{\eta}^\alpha$ is discussed in Sec.5.6.

The effective resolved shear stress that is the driving force for dislocation movement is defined as the difference between τ_η^α and the athermal strength related to the long-range interactions (such as dislocation cells, grain boundaries, etc.)

$$\tau_{\text{eff}}^\alpha = |\tau_\eta^\alpha| - s_a^\alpha. \tag{14}$$

In the case of small elastic strain, the contribution of the elastic deformation gradient can be neglected and the resolved shear stress can be calculated directly from the second Piola-Kirchhoff stress

$$\tau^\alpha = \underbrace{\boldsymbol{C}^e}_{\approx \boldsymbol{I}} \boldsymbol{S}^{\text{2PK}} : \vec{m}_0^\alpha \otimes \vec{n}_0^\alpha \approx \boldsymbol{S}^{\text{2PK}} : \vec{m}_0^\alpha \otimes \vec{n}_0^\alpha. \tag{15}$$

Considering cubic crystals (fcc and bcc), the tensor of elastic constants in the reference crystal coordinate system $\{\boldsymbol{C}\}$ can be written in terms of three constants C_{11}, C_{12}, and C_{44}, where the curly brackets $\{\cdot\}$ indicate the Voigt notation. Rotation of the tensor of elastic constants can be achieved through the following formula

$$\{\boldsymbol{C}\}' = \boldsymbol{T}\{\boldsymbol{C}\}\boldsymbol{A}\boldsymbol{T}^{-1}\boldsymbol{A}^{-1}, \tag{16}$$

where the rotation matrix $\boldsymbol{T}$ and the Reuter's matrix $\boldsymbol{A}$ are detailed in Appendix C. At this point, an analytical solution can be derived for a single crystal flow stress as presented in Appendix D.

5.4. Slip system strength

In the preceding subsection, we have tacitly considered the division of strength s^α into two components: the athermal component s_a^α, associated with long-range interactions such as dislocation forests, grain boundaries, or precipitates, and the thermal component s_t^α, linked to lattice friction at absolute zero temperature. Here, we proceed with a detailed description of these parameters and their evolution laws.

In this work we introduce the following form of the athermal strength s_a^α

$$\begin{aligned} s_a^\alpha &= f(\rho^\alpha, d_{\text{char}}, f_p, r_p) \\ s_a^\alpha &= \underbrace{\kappa_0 \mu^\alpha b \sqrt{\sum_\beta A_{\alpha\beta}\rho^\beta}}_{\text{mean-field forest dislocations}} + \underbrace{\frac{k_{\text{HP}}\mu^\alpha\sqrt{b}}{\sqrt{d_{\text{mfp}}^\alpha}}}_{\text{microstructure}} + \underbrace{\frac{a^0 b\mu}{M}\frac{\sqrt{f_p}}{r_p}\log\left(\frac{r_p}{b}\right)}_{\text{precipitates}}, \end{aligned} \tag{17}$$

where the total athermal strength is decomposed into the strength due to (1) forest of dislocations, (2) interfaces that obstruct the motion of dislocations such as grain boundaries (block boundaries in case of maraging steel), and presence of (3) fine nano-sized precipitates.

The first part of Eq.17 follows the conventional Taylor model (Taylor, 1934), (Franciosi et al., 1980). Here, κ_0 is a fitting parameter, $\mu^\alpha = s_{ij}^\alpha C_{ijkl} s_{kl}^\alpha$ is the shear modulus (s_{ij}^α is the Schmid tensor) and b is the magnitude of Burger's vector. The matrix $A_{\alpha\beta}$ introduces interaction strengths for various dislocation juntions that form between the slip systems α and β. The second part consists of the Hall-Petch strengthening where k_{HP} is the Hall-Petch coefficient, and d_{mfp}^α is the mean free path a dislocation can travel within the domain until it reaches an impenetrable boundary and starts to pile up. Finally, the third part is the Orowan-Ashby formula for predicting the strength due to the presence of precipitates considering both Orowan mechanism of dislocation loops and Friedel mechanism of precipitate shearing (Matsukawa, 2019), (Schnitzer et al., 2010), where M is the Taylor factor ($M = 2.5$ (Galindo-Nava et al., 2016)).

It is considered that for the maraging steel material system the primary obstacle to dislocations are block boundaries with the strengthening mechanisms which can be described by Hall-Petch like behavior (Du et al., 2016), (Ghassemi-Armaki et al., 2013). In order to calculate the mean free path d_{mfp}^α of the elongated block structures (see Fig.6), we introduce an ellipsoidal representation of blocks. Given an ellipsoid, the mean free path can be calculated following (Beyerlein and Tomé, 2008), (Ghorbanpour et al., 2017)

$$d_{\text{mfp}}^\alpha = \frac{2}{\sqrt{\left((m_x^\alpha/a)^2 + \left(m_y^\alpha/b\right)^2 + (m_z^\alpha/c)^2\right)}}, \tag{18}$$

where $\vec{m}^{\alpha}$ represents the direction of slip in the frame of reference of the ellipsoid. The transformation between the reference and the ellipsoid coordinate system can be expressed through

$$\vec{m}_e^{\alpha} = \boldsymbol{R}\vec{m}^{\alpha}, \tag{19}$$

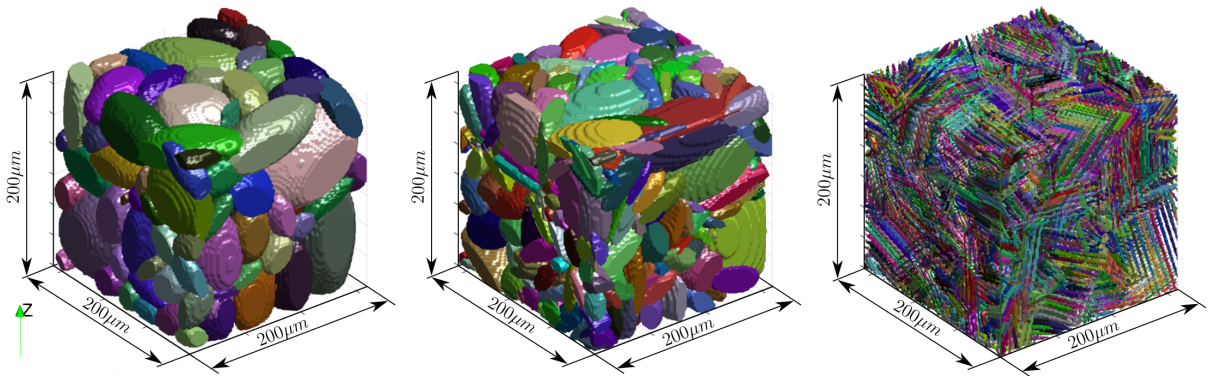
where $\boldsymbol{R} = \begin{bmatrix} \boldsymbol{n}_1 & \boldsymbol{n}_2 & \boldsymbol{n}_3 \end{bmatrix}^T$. Here, $\boldsymbol{n}_i$ vectors represent the directions of the ellipsoid's semi-axis.
In order to establish the ellipsoidal representation of the blocks, it is necessary to identify the domains characteristic of the mean free path d^{α}_{mfp}. For that purpose we have developed a clustering algorithm that identifies regions of misorientation less than $\Delta\theta_c$, typically less than 15°. The recursive framework of such algorithm is presented in Appendix E. Identification of grains (blocks) can be employed at every time step of the simulation, thus allowing for an adaptive Hall-Petch effect having its importance at large plastic deformations with significant grain growth. However, due to the large system size employed in this study and the prohibitively high simulation cost of on-the-fly cluster identification, we will simplify our approach by considering only the initial mean free path of the undeformed system.
Following the identification of individual clusters, the Principal Component Analysis (PCA) is used for approximation of the domain shape using an ellipsoid. The PCA operates on data points of each cluster, which can be collated into a matrix

$$\boldsymbol{X} = \begin{bmatrix} \vec{x}_1 & \vec{x}_2 & \dots & \vec{x}_N \end{bmatrix}^T. \tag{20}$$

With this, the covariance matrix $\boldsymbol{S}$ can be calculated using the following formula

$$\boldsymbol{S} = \frac{1}{n-1}\left(\boldsymbol{X} - \boldsymbol{I}\vec{c}\right)^T \boldsymbol{X}, \tag{21}$$

where $\vec{c}$ represents the centre point of the dataset, $c_i = \frac{1}{n}\sum_j X_{ij}$. The ellipsoid is then uniquely defined by the eigen values and eigen vectors of the covariance matrix $\boldsymbol{S}$, where the eigen values define the centre of the ellipsoid and eigen vectors the orientation of the semi axis.
The results of the principal component analysis applied to the martensite RVE are presented in Fig.7, where for a more comprehensive illustration, the PCA is applied at the level of (a) prior austenite grains, (b) martensite packets, and (c) martensite blocks. The strengthening is; however, considered to take place only at the level of blocks.



(a) 161 grains. (b) 482 packets. (c) 3106 blocks.

Figure 7: Ellipsoidal representation of the grain, packet and block microstructure for the purpose of calculating the mean free path d^{α}_{mfp} on individual slip systems. Colors are assigned randomly to clearly distinguish between different clusters.

It is anticipated that during the plastic deformation the highly dislocated grains will provide most of the strengthening due to the forest of dislocations rather than the pile up of dislocations at grain boundaries.

The evolution of dislocation densities can be captured by the following formula (Mecking and Kocks, 1981)

$$\dot{\rho}^{\alpha} = \left(\kappa_1 \sqrt{\sum_{\beta \neq \alpha} \rho^{\beta}} - \kappa_2 \rho^{\alpha} \right) |\dot{\gamma}^{\alpha}|, \tag{22}$$

where k_1 and k_2 are material constants related to the rate of nucleation and rate of annihilation of dislocations. Here, they are considered to be fitting parameters. It can be shown that the saturation value for dislocation density can attain $\rho_{max} = \frac{\kappa_1 \sqrt{n-1}}{\kappa_2}$, where n is the total number of active slip systems.
Experiments suggest that the martensitic phase is highly dislocated (Chadha et al., 2020) reaching the densities of up to ρ =10^{14} - 10^{16} m^{-2} (Raabe et al., 2009a), (Raabe et al., 2009b), (Cheng et al., 2023) which are close to the saturation value.

5.5. Slip systems

With the absence of close-packed planes, the identification of planes that carry dislocation motion in bcc metals poses a considerable challenge. The candidate planes under consideration are primarily the {110}, {211}, or {123} planes. While the {123} slip is mostly observed at elevated temperatures (Du et al., 2018), some experiments of room temperature deformation indicate slip on {211} planes (Marichal et al., 2013), (Du et al., 2018) together with {110}, the combination of which may further depend on temperature or alloy purity (Seeger, 2001), (Seeger, 2004). The consensus remains elusive even within the modelling community (see for instance single crystal simulations by (Yalcinkaya et al., 2008) and (Koester et al., 2012), who were both able to reproduce the same experimental stress-strain curves each using a different set of slip systems). At the atomistic level of dislocation, slip is constrained to the {110} planes, as evidenced by displacement differential maps of dislocation cores obtained through atomistic simulations (Gröger et al., 2008a). Thus, what is commonly perceived as a {211} slip may actually correspond to a zig-zag motion of dislocations along the {110} planes. Therefore, this study focuses solely on slip occurring on {110} planes. Additionally, the complexity of screw dislocation cores in bcc metals leads to non-Schmid behavior, necessitating the consideration of 24 slip systems on {110} planes instead of 12 to differentiate between the direction of dislocation motion.
The slip systems considered in this work are listed in Table F.5. The Schmid-Boas notation is used (Schmid and Boas, 1950) adopted by (Madec and Kubin, 2017), where A, B, C, D represent the slip directions ($\bar{1}11$), (111), ($\bar{1}\bar{1}1$), ($1\bar{1}1$)), and 1, 2, 3, 4, 5, 6 correspond to the slip planes [011], [01$\bar{1}$], [101], [$\bar{1}$01], [$\bar{1}$10], [110], which is reciprocal to the notation in fcc crystals.

5.6. Non-Schmid effects

In contrast to the conventional assumption of the Schmid's law, the atomistic simulations of screw dislocations in bcc metals firmly establish that the activation enthalpy for dislocation motion ΔG depends on both the stress perpendicular to the slip direction as well as the stress parallel to the slip direction (Gröger et al., 2008a), (Gröger et al., 2008b). This gives rise to the tension-compression asymmetry and twinning-antitwinning asymmetry which is a common characteristic of all bcc metals.
In order to capture such effects in continuum crystal plasticity models, simple non-Schmid criteria were proposed (Dao and Asaro, 1993), (Qin and Bassani, 1992) (see Eq.13), by means of which the resolved shear stress τ^{α} is incremented by an additional term τ^{*} represented as a linear combination of several components of the stress tensor σ_{ij} each given a certain weight η_i, $\tau^{*} = \boldsymbol{\eta} : \boldsymbol{\sigma}$. The drawback of such a general criterion is the large number of fitting parameters η_i, $i = 1 \ldots 9$, each without a clear intuitive physical meaning. A few variations of Eq.13 have been nevertheless proposed within a crystal plasticity framework, (Yalcinkaya et al., 2008), (Kempen et al., 2011), (Lim et al., 2015), (Chen et al., 2013), with (Lim et al., 2013) providing a comprehensive review of the existing yield criteria.
A more physical special form of Eq.13 which is adopted in this work was proposed by (Gröger et al., 2008b), (Gröger and Vitek, 2009), (Gröger, 2021), where the active components of the stress tensor have been identified through a series of atomistic simulations

$$\tau_{\eta}^{\alpha} = \tau^{\alpha} + \eta_1 \tau_{mn'}^{\alpha} + \eta_2 \tau_{tn}^{\alpha} + \eta_3 \tau_{t'n'}^{\alpha}. \tag{23}$$

The appealing feature of Eq.23 is that it operates with only three coefficients η_1, η_2 and η_3 that characterize the non-Schmid effects while these coefficients can be found by fitting to atomistic simulation data. Eq.23 operates with a linear combination of three stress components resolved in the directions of the plane normal $\boldsymbol{n}$, slip direction $\boldsymbol{m}$, dislocation line direction $\boldsymbol{t} = \boldsymbol{n} \times \boldsymbol{m}$ and the directions of a coordinate system that makes the angle $-60°$ with the reference plane $\boldsymbol{n}$, denoted by $'$.
In order to find the coefficients η_i for α-iron, we turn to the atomistic simulation data published by (Chen et al., 2013) and use the least-square method as presented in Appendix G.

5.7. Dislocation interactions

Dislocations moving along different slip systems have the potential to interact with each other, forming various junctions of differing strengths - forest hardening. The characterization of these junctions have been achieved predominantly through discrete dislocation dynamics (DDD) simulations which provide valuable insights into their types and associated strengths Queyreau et al. (2009). These findings can be integrated into a crystal plasticity model, especially when employing the Taylor hardening model as depicted in Eq.17. In particular, (Madec and Kubin, 2004), (Madec and Kubin, 2017) and (Lu et al., 2019) utilized DDD simulations to forecast the interaction coefficients for the five junctions identified in bcc metals, and presented the strengthening coefficients amongst others also for α-iron. The adopted interaction matrix employed in this study is presented in Table 2.

Table 2: Dislocation interaction matrix. Slip systems are labelled using the Schmid-Boas notation (Schmid and Boas, 1950).

	A2	A3	A6	B2	B4	B5	C1	C3	C5	D1	D4	D6
A2	a_0	a_1	a_1	a_2	a_3^*	a_3^*	a_4	a_3	a_5	a_4	a_5	a_3
A3	a_1	a_0	a_1	a_3	a_4	a_5	a_3^*	a_2	a_3^*	a_5	a_4	a_3
A6	a_1	a_1	a_0	a_3	a_5	a_4	a_5	a_3	a_4	a_3^*	a_3^*	a_2
B2	a_2	a_3^*	a_3^*	a_0	a_1	a_1	a_4	a_5	a_3	a_4	a_3	a_5
B4	a_3	a_4	a_5	a_1	a_0	a_1	a_5	a_4	a_3	a_3^*	a_2	a_3^*
B5	a_3	a_5	a_4	a_1	a_1	a_0	a_3^*	a_3^*	a_2	a_5	a_3	a_4
C1	a_4	a_3	a_5	a_4	a_5	a_3	a_0	a_1	a_1	a_2	a_3^*	a_3^*
C3	a_3^*	a_2	a_3^*	a_5	a_4	a_3	a_1	a_0	a_1	a_3	a_4	a_5
C5	a_5	a_3	a_4	a_3^*	a_3^*	a_2	a_1	a_1	a_0	a_3	a_5	a_4
D1	a_4	a_5	a_3	a_4	a_3	a_5	a_2	a_3^*	a_3^*	a_0	a_1	a_1
D4	a_5	a_4	a_3	a_3^*	a_2	a_3^*	a_3	a_4	a_5	a_1	a_0	a_1
D6	a_3^*	a_3^*	a_2	a_5	a_3	a_4	a_3	a_5	a_4	a_1	a_1	a_0

In total, there are seven coefficients governing six potential dislocation interactions, with one exhibiting degeneracy, resulting in two coefficients for the case when the slip systems are swapped.
As highlighted by (Madec and Kubin, 2017), only non-coplanar interactions can be reliably determined through DDD simulations. Consequently, coefficients a_0 and a_2 related to the co-planar interactions remain undetermined, but can be considered weak relative to the remaining interactions.

6. Crystal plasticity model for fcc phase (austenite)

Due to its significantly weaker sensitivity to strain rate and temperature compared to bcc crystals, we opted for a simpler form of a rate-dependent crystal plasticity model for the austenite phase. In this approach, the kinetics of dislocation slip is characterized using a straightforward power-law function (Kocks, 1987), (Dao and Asaro, 1993)

$$\dot{\gamma}^\alpha = \dot{\gamma}_0^\alpha \left(\frac{|\tau^\alpha|}{s^\alpha} \right)^{\frac{1}{m}} \operatorname{sign}(\tau^\alpha) \,. \tag{24}$$

Here, $\dot{\gamma}_0^\alpha$ represents a reference slip rate (distinct from the reference slip rate in Eq.11), τ^α is the resolved shear stress as defined in Eq.15, s^α represents the slip system strength, and m serves as a rate sensitivity

parameter. The strength of the slip system is predominantly influenced by the evolution of dislocation density ρ and can be thus written as

$$s^{\alpha} = \kappa_0 \mu^{\alpha} b \sqrt{\sum A_{\alpha\beta} \rho^{\beta}}. \tag{25}$$

The same formulation as listed in Eq.22 is used for capturing the evolution of dislocation densities in the fcc phase. Unlike bcc crystals, fcc crystals of austenite typically do not exhibit non-Schmid effects, except in special cases for instance involving precipitates (Ghorbanpour et al., 2017). Within our model, no precipitation is assumed to occur in the austenitic phase. The governing equations for the fcc phase largely mirror those introduced in Sec.5, with the exception that only 12 slip systems $\{111\}\langle 110\rangle$ are considered, as specified in Table F.6 below. Additionally, the dislocation interaction matrix is the same as presented in Table 2, albeit considering the Schmid-Boas notation for fcc crystals.
The numerical implementation of the governing equations is presented in Appendix H.

7. Summary of material parameters

Material parameters used in simulations of this study are specified in Table 3 for the case of the martensite phase and in Table 4 for the case of the austenite phase. The citation is given to the parameters that are available in the literature either from discrete dislocation dynamics, atomistic simulation data or earlier crystal plasticity studies. The parameters without the source were fitted through a trial and error exercise to match the experimental stress-strain curves, specifically, the initial dislocation density ρ_0, thermal strength s_t, and Kocks-Mecking coefficients κ_1, and κ_2. An assumption has been made to simplify the energy barrier by setting $p = 1$ and $q = 2$ such as was also done for instance in (Koester et al., 2012). This simplification is also numerically beneficial. The non-Schmid coefficients were fitted as detailed in Appendix G, to match the data obtained from the atomistic simulations.
For the sake of simplicity, we maintain consistent notation for dislocation interactions in fcc and bcc systems, as presented in Table 2. Based on (Madec and Kubin, 2017), distinctions in notation are made between fcc and bcc crystals. In bcc crystals, a_0 denotes weak self-interaction, a_2 corresponds to coplanar interaction, and a_3, a_4, a_5 are associated with colinear interactions. In fcc crystals, a_0 signifies weak self-interaction, a_1 refers to coplanar interaction, a_2 is linked to colinear interaction, and a_4, a_3^*, and a_5 are designated for the Hirth, glissile junction, and the Lomer lock, respectively. Some interactions may exhibit double degeneracy, denoted by an asterisk when the slip systems are switched. Since discrete dislocation dynamics cannot precisely measure the strength of self-interactions (Madec and Kubin, 2017), a relatively weak weight of 0.1 is assigned to them.
In order to determine the ratio between the initial dislocation density of the austenite to martensite phase, we turn to the investigation conducted by (Macchi et al., 2021). This study delves into dislocation densities in austenite and martensite of low carbon steels during quenching, revealing a dependency of average dislocation density on the volume fraction of martensite. Following these findings, it is reasonable to assume that $\rho_{\alpha} \approx 30 \times \rho_{\gamma}$. While some studies have also shown in-situ tempering of martensite during the process of additive manufacturing introducing another length-scale associated with dislocation density variations within the martensite (Kljestan et al., 2024), we make a simplifying assumption considering uniform dislocation density in each phase in the initial RVE configuration.

Table 3: Summary of material parameters for the bcc phase. Values obtained from the literature are cited. The remaining parameters are calculated or fitted to obtain experimentally measured stress strain curve (Wei et al., 2022).

Symbol	Value	Unit	Description	Source
Crystal lattice				
a_0	0.3291	nm	lattice parameter	(Chen et al., 2013)
$b = (\sqrt{3}/2)a_0$	0.285	nm	Burger's vector magnitude	
Elastic properties				
C_{11}	236.0	GPa	elastic constant	# = ((Narayanan et al., 2014), (Koester et al., 2012), (Yalcinkaya et al., 2008))
C_{12}	134.0	GPa	elastic constant	#
C_{44}	119.0	GPa	elastic constant	#
$2C_{44}/(C_{11} - C_{12})$	2.33	-	Zener ratio	
Slip kinetics				
$\dot{\gamma}_0$	2.44e7	s^{-1}	reference slip rate	(Koester et al., 2012)
G_0	1.1536e-19	J	activation energy	(Koester et al., 2012)
p	1.0	-	activation energy shape	(Koester et al., 2012)
q	2.0	-	activation energy shape	(Koester et al., 2012)
Hardening				
k_{HP}	1.0e5	Pa $m^{1/2}$	Hall-Petch coefficient	motivated by (Motaman et al., 2020), (Galindo-Nava et al., 2016), (Ghorbanpour et al., 2017)
s_t	395.5	MPa	thermal strength	(Koester et al., 2012)
ρ_0	3.0e13	m^{-2}	initial dislocation density	motivated by (Raabe et al., 2009a), (Raabe et al., 2009b), (Cheng et al., 2023)
a_0	0.1	-	dislocation interaction constant	
a_1	0.93	-	dislocation interaction constant	& = ((Madec and Kubin, 2004), (Madec and Kubin, 2017))
a_2	0.1	-	dislocation interaction constant	
a_3	0.29	-	dislocation interaction constant	&
a_3^*	0.19	-	dislocation interaction constant	&
a_4	0.34	-	dislocation interaction constant	&
a_5	0.39	-	dislocation interaction constant	&
κ_0	1.0	-	Kocks-Mecking constant	
κ_1	5.0e7	m^{-1}	Kocks-Mecking constant	
κ_2	40	-	Kocks-Mecking constant	
a^0	0.12	-	coefficient in Orowan equation	(Galindo-Nava et al., 2016)
Non-Schmid effects				
η_1	0.4675	-	non-Schmid constant	Appendix G
η_2	0.1034	-	non-Schmid constant	Appendix G
η_3	0.5652	-	non-Schmid constant	Appendix G
τ_c/C_{44}	0.0237			

Table 4: Summary of material parameters for the fcc phase.

Symbol	Value	Unit	Description	Source
Crystal lattice				
a_0	0.3628	nm	lattice parameter	(Govindaraj et al., 2021)
$b = \sqrt{3}/2a_0$	0.2565	nm	Burger's vector magnitude	
Elastic properties				
C_{11}	209	GPa	elastic constant	(Shmulevitsh et al., 2015)
C_{12}	133	GPa	elastic constant	(Shmulevitsh et al., 2015)
C_{44}	121	GPa	elastic constant	(Shmulevitsh et al., 2015)
$2C_{44}/(C_11 - C_12)$	3.18	-	Zener ratio	
Slip kinetics				
$\dot{\gamma}_0$	0.00001	s^{-1}	reference slip rate	
m	0.1	-	rate sensitivity parameter	
Hardening				
ρ_0	1.0e12	m^{-2}	initial dislocation density	motivated by (Macchi et al., 2021)
a_0	0.1	-	dislocation interaction constant	
a_1	0.2	-	dislocation interaction constant	& = ((Madec and Kubin, 2004), (Madec and Kubin, 2017))
a_2	0.32	-	dislocation interaction constant	&
a_3	0.38	-	dislocation interaction constant	&
a_3^*	0.1	-	dislocation interaction constant	&
a_4	0.81	-	dislocation interaction constant	&
a_5	0.3	-	dislocation interaction constant	&
κ_0	1.0	-	Kocks-Mecking constant	
κ_1	5.0e7	m^{-1}	Kocks-Mecking constant	
κ_2	40	-	Kocks-Mecking constant	

8. Simulations of mechanical loading of as-built RVEs

In this section, simulation results are presented that focus on investigations of the mechanical response of the established as-built lath martensite RVE. This include (1) uniaxial loading in tension investigating the effect of the presence of small austenitic grains along the meltpool boundaries, (2) loading in compression investigating the effect of tension-compression asymmetry, as well as (3) demonstrating the effect of temperature and rate of loading.

8.1. Uniaxial loading in tension

First, let us examine the complete as-built lath martensite Representative Volume Element (RVE), which features small austenitic grains along the meltpool boundaries (see Fig.6). The RVE is prescribed to undergo a displacement-controlled loading along the z-coordinate, with a prescribed displacement boundary conditions of $u_z(Z=0)=0$ and $u_z(Z=1)=\hat{u}$, with a loading rate of $\dot{\varepsilon}=\frac{du_z}{dt}=3.3\times10^{-4}$ s^{-1}. In all simulation results (unless otherwise specified), the engineering stress σ^{eng} and engineering strain ε^{eng} components are derived from the volume average of the Cauchy stress in the loading direction, $\langle\sigma\rangle=\frac{1}{V_\Omega}\int\sigma_{zz}d\Omega$, and the volume average of the true strain in the loading direction, $\langle\varepsilon\rangle=\frac{1}{V_\Omega}\int\varepsilon_{zz}d\Omega$, respectively. These metrics are the default outputs in the finite element simulation and utilize the standard stress-strain transformation relationships.

The simulated engineering stress-strain curve is depicted by the bold blue curve in Fig.8, and is accompanied by various markers representing available experimental data sourced from the literature.

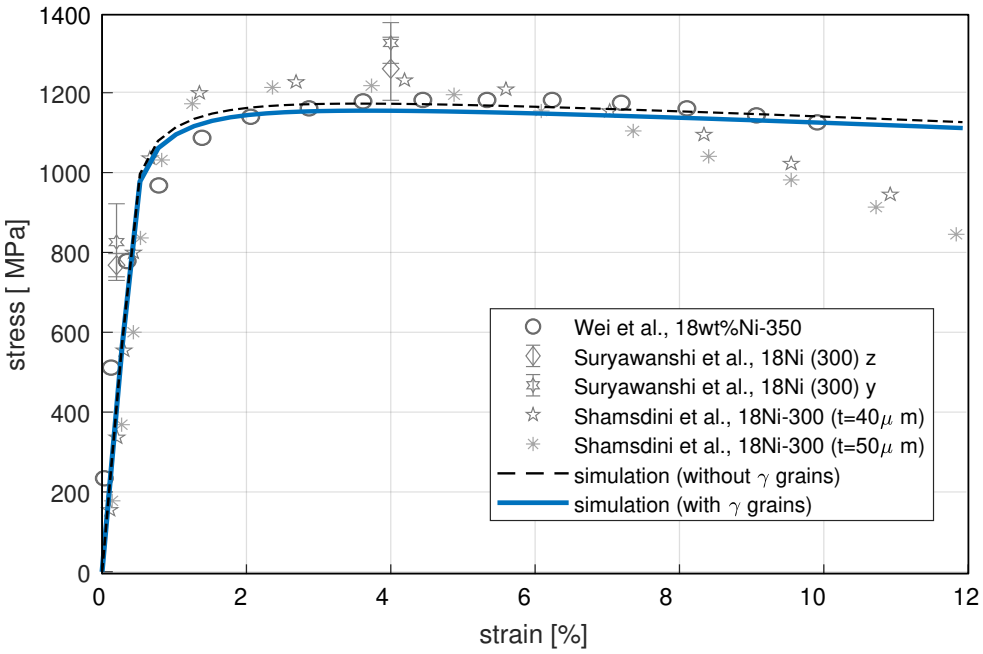
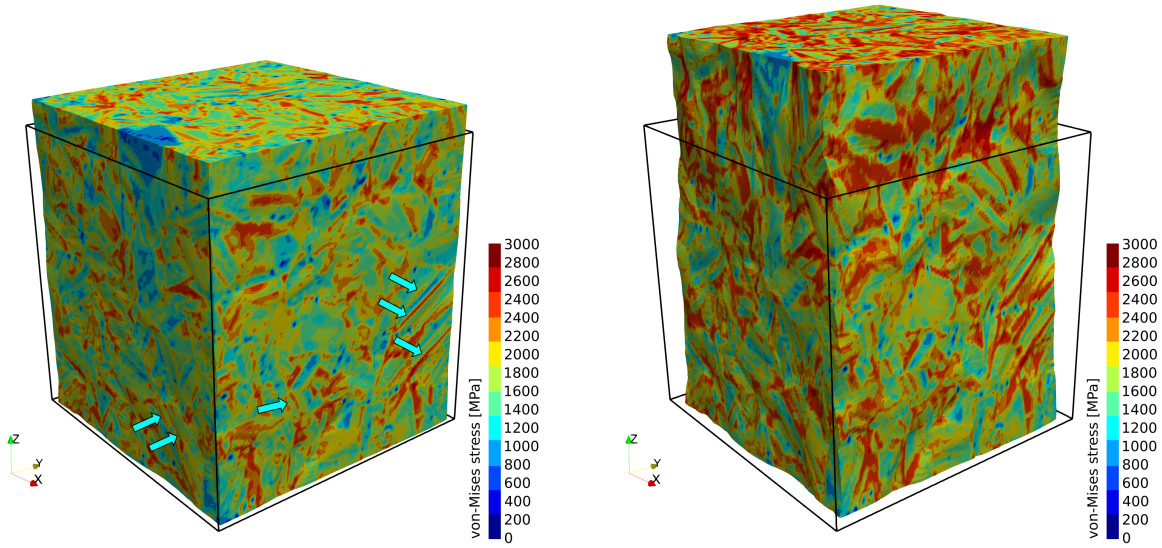


Figure 8: Engineering stress-strain curve predicted using the simulation in companion with available experimental data points from the literature ((Wei et al., 2022), (Suryawanshi et al., 2017), (Shamsdini et al., 2021)).

The predicted stress-strain curve in Fig.8 indicates a very good agreement with the experimental data by (Wei et al., 2022) as well as those measure by (Suryawanshi et al., 2017), (Shamsdini et al., 2021). At larger strains, it is anticipated that the loading behavior will be primarily influenced by void growth and the coalescence of micro-cracks (Shamsdini et al., 2021) which are not part of this study. These phenomena would likely explain the more pronounced deviations in softening behavior observed after 10% strain.

The presence of small grains along the meltpool boundaries raises questions about their contribution to the mechanical response of the martensitic RVE. To address this, another simulation is conducted under identical loading conditions, but without the presence of austenitic grains along the meltpool boundaries. The resulting stress-strain response is illustrated in the same figure (Fig.8) and denoted using the black dashed curve. The findings suggest that the 2.1% volume fraction of austenite does not significantly influence the stress-strain response, with only a minor decrease in flow stress observed due to the presence of the softer austenitic phase, while the overall trends remain consistent.

Snapshots of the simulated RVE are presented in Fig.9 showing the von-Mises stress and in Fig.10 showing the distribution of the total dislocation density $\rho = \sum_\alpha \rho^\alpha$. In addition, Fig.11 depicts the overall deformation, Fig.12 illustrates the texture evolution during the loading with inverse-pole figure coloring. The pole figures of the initial and the deformed configuration are then presented in Fig.13 and Fig.14, respectively.



(a) At 10% engineering strain. Arrows indicate some visible stress concentrations along block boundaries.

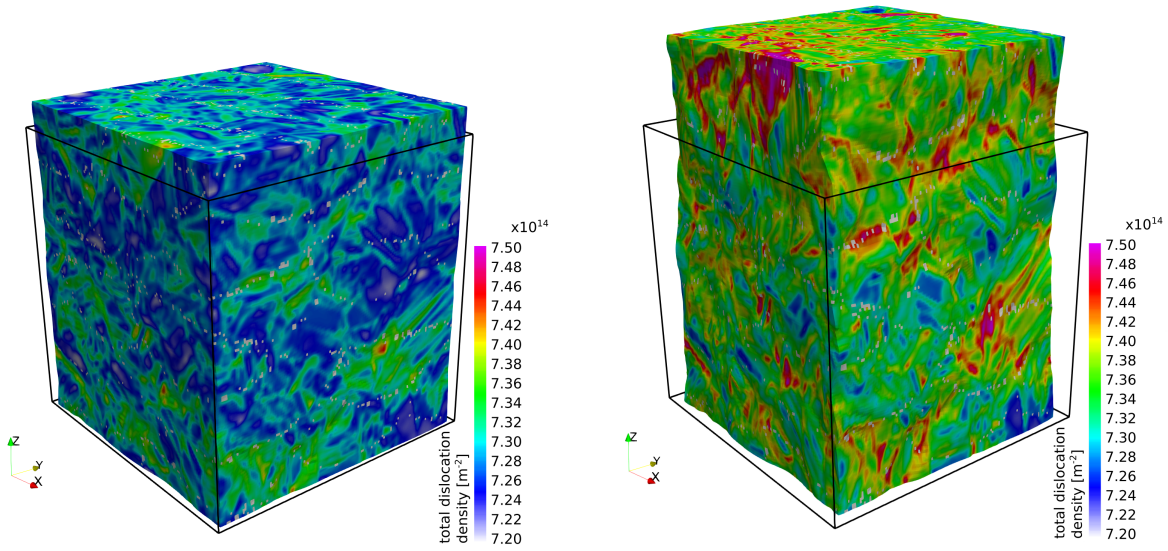
(b) At 30% engineering strain.

Figure 9: Von-Mises stress at different levels of deformation. Loading is along the build direction (z).

The findings in Fig.9 indicate non-uniform von-Mises stress distribution with local stress concentrations appearing near the martensite block boundaries. Some of the clearly visible regions are indicated by the bold arrows. Interestingly, at higher levels of strain, the underlying microstructure pattern becomes more visible where it is appearing through alternating regions of high and low stresses. The presence of the small austenitic grains is not clearly visible in the stress field. While we are able to assess their contribution on the stress-strain response as presented in Fig.8 and later in Fig.19, a more detailed analysis of the stress field near the austenite-martensite interface would necessitate a higher resolution model.

Analysis of the dislocation density field underscores the non-hardening mode observed in the macroscopic stress-strain curve in Fig.8. The initially high strength of the as-built RVE, devoid of precipitates, correlates with the high initial dislocation density of the martensite. During loading, a dislocation density map forms in tandem with the martensitic microstructure as seen in Fig.10(a), albeit with relatively minor variations in total density values. This suggests a saturation level in dislocation densities, as per Eq.22 where the rate of nucleation and anihiliation of dislocation has reached an equilibrium. While dislocation density increases near the block boundaries, the overall distribution remains relatively uniform ranging from 7.2 to $7.5{\cdot}10^{14}\mathrm{m}^{-2}$.

The overall deformation of the RVE as depicted in Fig.11 reveals that the applied uniaxial loading induces a relatively uniform deformation without any significant macroscopic plastic localization. An interesting aspect of the deformation is the emergence of the martensite microstructure at the surface in the form of



(a) At 10% engineering strain.

(b) At 30% engineering strain. Dashed lines indicate the macroscopic deformation mode.

Figure 10: Total dislocation density $\sum_\alpha \rho^\alpha$ at different levels of deformation. Loading is along the build direction (z).

corrugations, a characteristic of anisotropic plastic flow. The individual blocks (or a collection of blocks) are discernible in the deformed RVE some of them highlighted by arrows. The subfigure on the right provides a side view of the y-z front surface, displaying the variations in its deformed shape.

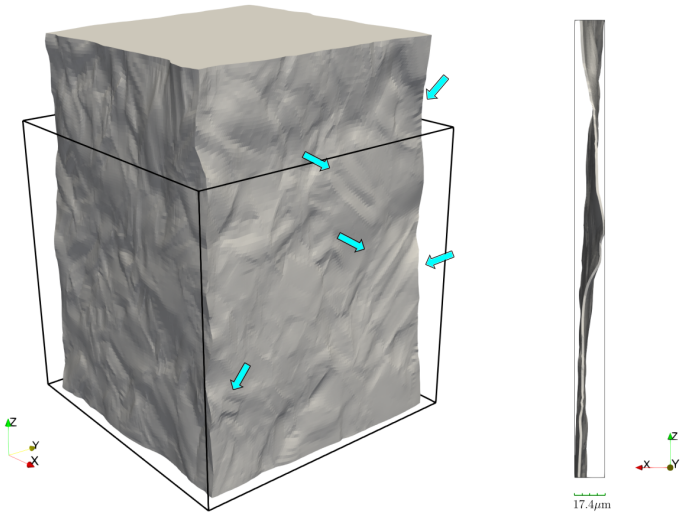
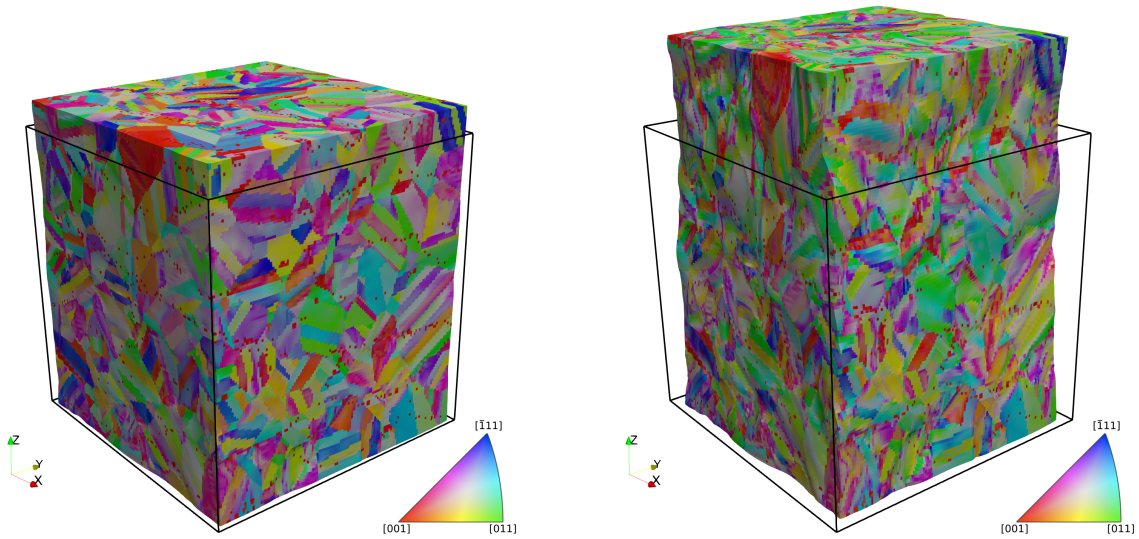


Figure 11: Deformed shape of RVE at 30% of engineering strain depicting the anisotropic plastic flow associated with the crystallographic aspects of individual martensitic variants.

Fig.12 illustrates the rotation of the crystal lattice during deformation due to dislocation slip (Eq.7). It is observed that the martensitic bcc phase aligns with the $\langle 011 \rangle$ direction, indicated by a transition in colors towards green, while the small austenitic fcc phase maintains alignment with the $\langle 001 \rangle$ direction retaining the red color.

Lattice rotation in Fig.12 is directly enticed with stress distribution and changes in dislocation density in

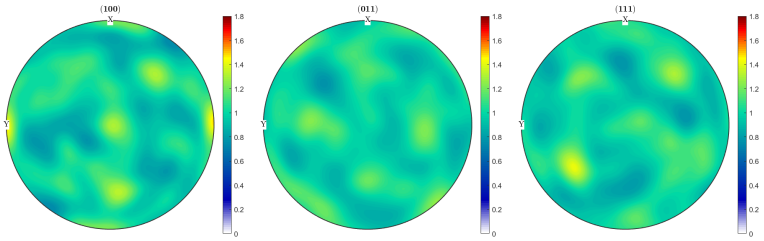


(a) At 10% engineering strain. (b) At 30% engineering strain.

Figure 12: Lattice orientation at different levels of deformation. Loading is along the build direction (z).

Fig.9 and Fig.10, respectively. Regions where the lattice rotates towards a softer orientation relative to the loading direction experience higher stress levels. Contribution of this form of geometric softening can be also revealed by the negative slope of the flow stress in Fig.8.

Finally, the pole figures of martensite (austenite phase is neglected) offer a macroscopic view of texture evolution depicting the initial configuration in Fig.13, showing no preferential lattice orientation and random texture, while at 30% strain in Fig. 14 indicating a stronger preference towards the ⟨011⟩ orientation in agreement with texture evolution in a similar material presented by (Kljestan et al., 2024).

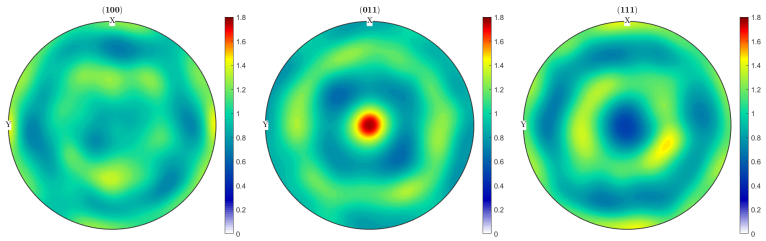


(a) (100). (b) (011). (c) (111).

Figure 13: Pole figures of the initial martensite microstructure of random texture.

8.2. Tension-compression asymmetry

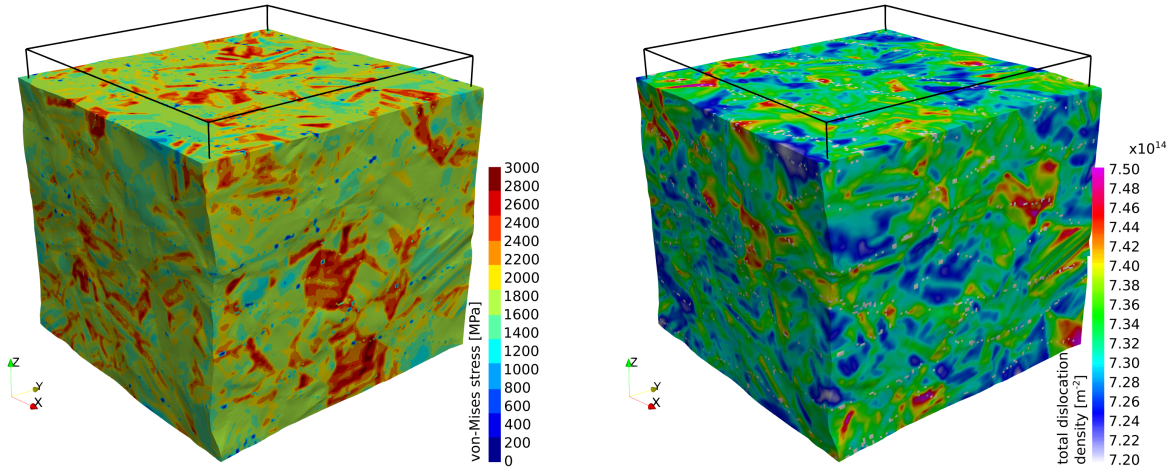
In this study, tension-compression asymmetry is exclusively attributed to the effects stemming from the intricate non-planar core of the screw dislocation (Gröger et al., 2008a), (Gröger, 2014), (Gröger and Vitek, 2009). Such a characteristic is anticipated across all bcc metals, thus also expected in maraging steels (Cyr et al., 2018). It is noteworthy to mention that other studies have also pointed to the contribution of process-induced residual stresses on tension-compression asymmetry (Chen et al., 2019). While various such contributions may play a role, in the first approximation of this study, we will focus only on the intrinsic factors associated with the non-Schmid effects. Residual stresses (as an extrinsic factor) can be easily added on if given, for instance obtained through a process-microstructure-property model.



(a) (100). (b) (011). (c) (111).

Figure 14: Pole figures depicting the orientation distribution function of the martensite microstructure at 30% strain.

Both tension-compression asymmetry and twinning-antitwinning asymmetries are discussed in detail in Sec.5.3. To evaluate the macroscopic stress-strain response, the simulation RVE undergoes the same loading conditions as in the prior case but in the compressive direction. The deformed configuration is depicted in Fig.15, wherein subfigure (a) shows the distribution of von-Mises stress, while subfigure (b) shows the distribution of the total dislocation density.



(a) Distribution of von-Mises stress. (b) Distribution of total dislocation density.

Figure 15: Deformation of the RVE at 10% engineering strain in compression depicting the distribution of von-Mises stress and total dislocation density. Loading is along the build direction (z).

The stress and dislocation density distribution are significantly influenced by the underlying orientation of the crystal lattice, with elevated levels observed in orientations softer relative to the loading direction. No macroscopic localization of plastic deformation is evident, and the formation of local bands along interfaces is less pronounced compared to tensile loading.

The stress-strain curves for the RVE loaded in all three directions (x, y, z) are presented in Fig.16 and are evaluated for both tensile and compressive cases.

It is evident that there is minimal variation in the flow stress among cases loaded along different coordinates, which unlike in a single crystal case is an expected outcome considering the initially random microstructure texture. However, a noticeable difference in the initial value of flow stress between the tensile and compressive stress-strain curves is observed. This difference directly arises from the non-planarity of the screw dislocation core, where the critical glide stress depends on the stress direction perpendicular to the dislocation line

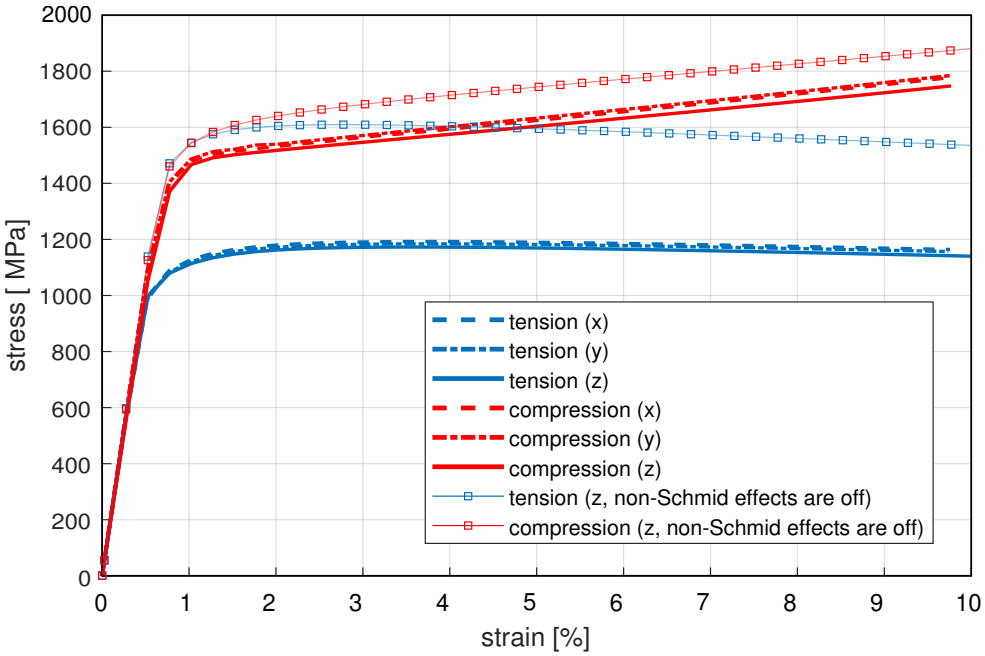


Figure 16: Engineering stress-strain curves depicting the tension-compression asymmetry originating from the effects of non-planar dislocation cores. Here, x, and y indicate the transverse direction, while z indicates the build direction.

(Gröger et al., 2008b), (Savage et al., 2017). Comparable values were experimentally predicted by (Cyr et al., 2018). However, this experimental study also observed stress variations for different loading directions, contrasting with the prevailing notion of isotropic behavior in maraging steel (Mooney et al., 2019), (Zhao et al., 2022), (Kannan and Nandwana, 2022). Hence, further experimental evidence regarding the tension-compression behavior of maraging steel will be beneficial.

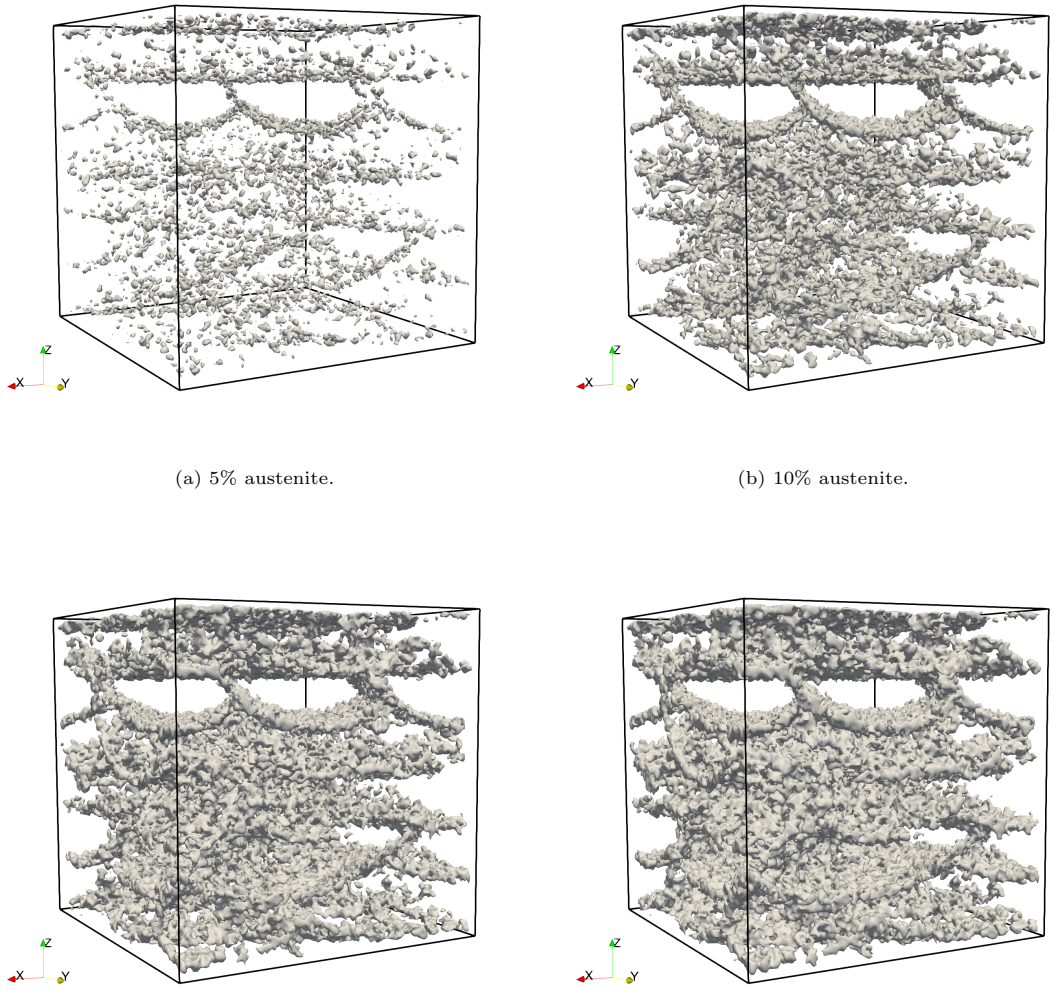
As part of the simulation exercise, we have also evaluated the hypothetical case in which the non-Schmid effects are set to zero. Two simulations, one in tension and one in compression are depicted in Fig.16 using square symbols. It is clear that without non-Schmid effects, the yield stress in both tension and compression is the same. The overall analysis of the stress-strain response indicate that during the tensile loading, the glide of dislocations is easier providing lower value of yield stress. Atomistically speaking, this can be imagined by the dislocation core being elongated and spreading along one single (101) plane, which facilitates easy glide. Unlike in the compressive case, where dislocation core would spread into multiple planes creating significant friction and retaining high values of yield stress. Such distortions of dislocation core were depicted in the atomistic simulation study by (Chen et al., 2013).

For a more comprehensive coverage, the dependence of the stress-strain curve on strain rate and temperature is presented in Appendix J.

9. Simulations of mechanical loading of heat treated RVEs

The heat treatment of maraging steel is associated with an interesting process of reversed phase transformation from martensite into austenite (Jägle et al., 2014), (Conde et al., 2019), (Takata et al., 2023), (Gong et al., 2020), (Ahluwalia et al., 2024), where the newly formed fcc phase is referred to as the reverted austenite (to distinguish it from the retained austenite). This process leads to the development of a multi-phase system, comprising lath martensite, austenite, and nano-sized precipitates. The emergence of reverted austenite and precipitates is anticipated to significantly influence the overall mechanical properties of the steel. To comprehend these effects and visualize the deformation process of RVEs characteristic of a

heat treatment process, four additional RVEs were generated considering the volume fraction of austenite f_γ: 5%, 10%, 15%, and 20%. These RVEs are presented in Fig.17.



(a) 5% austenite.

(b) 10% austenite.

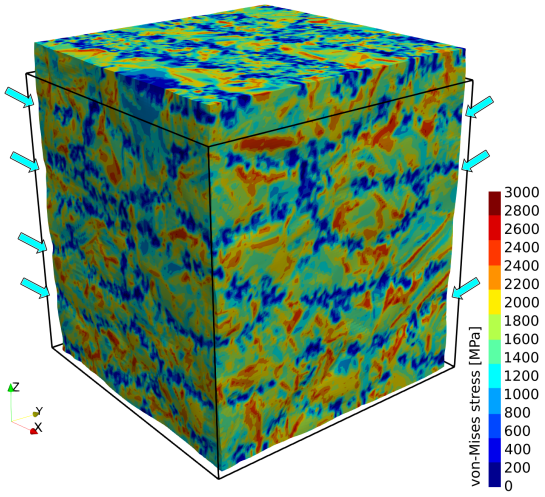
(c) 15% austenite.

(d) 20% austenite.

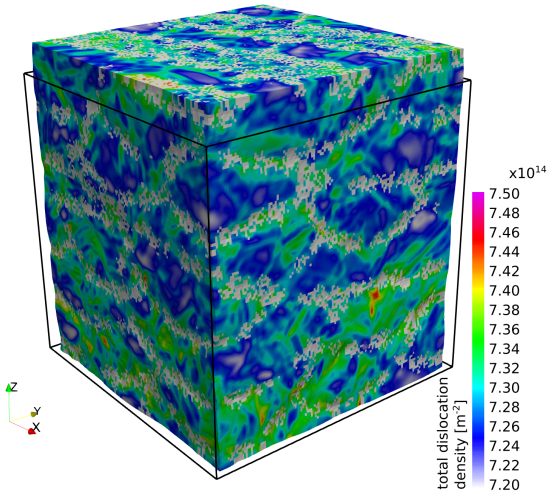
Figure 17: Contour plot depicting the austenite phase for a varying volume fraction f_γ. The reverted austenite grows from the pre-existing austenitic grains seeded along the meltpool boundaries.

These RVEs were created using the Monte Carlo method outlined in Section 4.1, under specific assumptions: (1) Reverted austenite is assumed to form from the pre-existing austenitic grains along the meltpool boundaries, growing with the same $\langle 001 \rangle$ orientation; (2) Nucleation of austenite is not considered; (3) The Monte Carlo method serves solely as a design tool to generate synthetic RVEs resembling experimentally heat-treated RVEs, as observed by (Takata et al., 2023). This approach is more intuitive than alternatives such as Voronoi tessellation and simpler than a phase field model (Ahluwalia et al., 2024), (Shchyglo et al., 2019). To increase the volume fraction of austenite, the Monte Carlo method needs to incorporate the bulk energy difference ΔF between the two phases. In addition to the parameters specified in Sec.4.1, the bulk

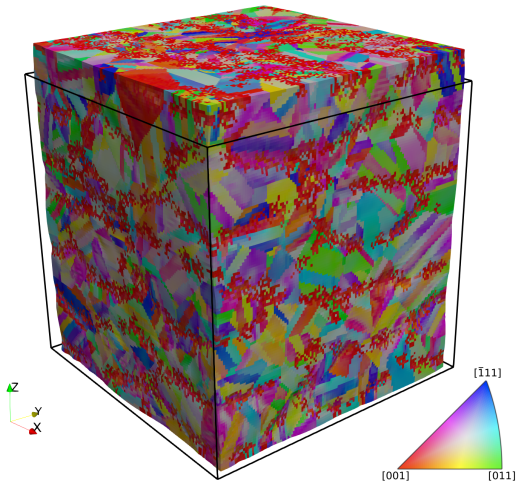
energy difference has been set to $\Delta F = 25$J. The outcomes of the Monte Carlo simulation are recorded and presented in Fig.17. When viewed from the correct perspective, meltpool boundaries can be easily identified. Tensile test simulations were performed up to 10% of engineering strain under the same loading conditions as employed throughout the previous part of the paper. The distribution of von-Mises stress, dislocation densities, and lattice orientation for the case with 20% of austenite is presented in Fig.18. Results for all variations of reverted austenite are collated in Appendix K. It is important to highlight that as in the previous section, the effect of process-induced residual stresses is neglected.



(a) Von-Mises stress. Arrows indicate visible localized deformation in form of corrugations near the austenitic phase.



(b) Total dislocation density.



(c) Lattice orientation.

Figure 18: Von-Mises stress, total dislocation density $\sum_\alpha \rho^\alpha$, and lattice orientation in the RVE with 20% of austenite at 10% strain. Meltpool boundaries are clearly visible as regions with low stress, relatively higher dislocation density and $\langle 001 \rangle$ lattice orientation. Loading is along the build direction (z).

In Fig.18(a), deformation clearly localizes into the meltpool boundaries which can be easily recognized at

the surface in the form of corrugations highlighted by the arrows. Plastic deformation, however, still takes place in both martensite and austenite phase as evident by the dislocation density map and lattice rotation. The findings reveal an elevated level of dislocation activity in close proximity to the block boundaries (as discussed earlier) as well as near the martensite-austenite interface, with the latter being more pronounced in the case of a higher fraction of austenite, as depicted in Fig.18(b). The overall increase in the total dislocation density is not significant. As in the earlier cases, this is attributed to the very high initial dislocation density that makes the nucleation of additional dislocation content difficult. The martensite lattice rotation, presented in 18(c), follows the same trends as elucidated in Sec.8, while the orientation of the austenite phase remains relatively unchanged and retaining the $\langle 001 \rangle$ direction.
The stress-strain curves for varying volume fractions of austenite are presented in Fig.19.

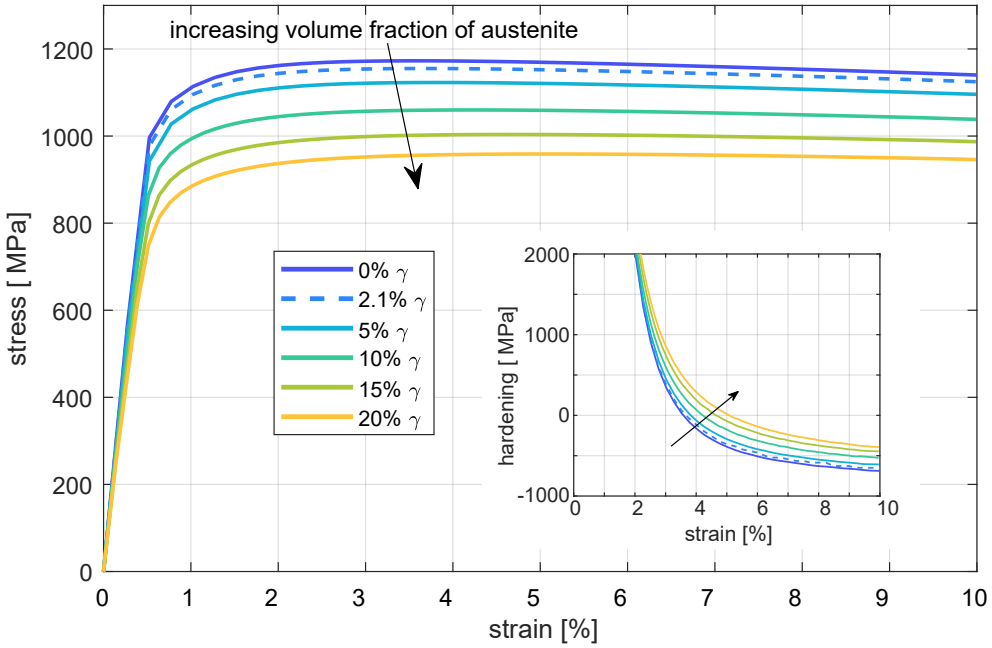


Figure 19: Engineering stress-strain curves for varying volume fraction of austenite (without the presence of precipitates). The subfigure illustrates the strain hardening of the presented stress-strain curves.

As expected, the increased volume fraction of austenite leads to a decrease in flow stress with subtle changes in hardening for varying austenite fractions, as indicated in the subfigure of Fig.19. The increase of volume fraction of austenite to f_γ =20% leads to approximately 200MPa reduction in flow stress.
Up to this point, the consideration of precipitates has been omitted. However, an important aspect of heat treatment is the formation of nanosized precipitates that act as the primary strengtheners, obstructing dislocation motion through the Orowan or Friedel mechanism. Interested in the effect of precipitates on the macroscopic flow stress, the same set of simulations of heat-treated RVEs is performed for varying sizes of precipitates r and precipitate volume fractions f_r. The combinations of $r = 1$nm, $r = 10$nm, $f_r = 10\%$, and $f_r = 20\%$ are considered. Such ranges of fractions and sizes can be obtained, for instance, through isothermal heat treatments as presented by (Ahluwalia et al., 2024).
The resultant stress-strain curves are collated in Fig.20, where the black curves correspond to the RVEs with $f_\gamma = 10\%$, blue curves to $f_\gamma = 15\%$, and green curves to $f_\gamma = 20\%$. The four different cases of volume fraction of precipitates and precipitate sizes are distinguished using different markers.
Having identified the macroscopic response of the twelve RVEs, we can hypothesize the following form of equation for the prediction of macroscopic yield stress σ_y, defined by the conventional 0.2% strain approach

$$\sigma_y^{0.2\%} = \left[\sigma_0 + k\frac{b}{r}\sqrt{f_r}\log\left(\frac{r}{b}\right)\right](1-f_\gamma)^n + \sigma_\gamma f_\gamma^n. \tag{26}$$

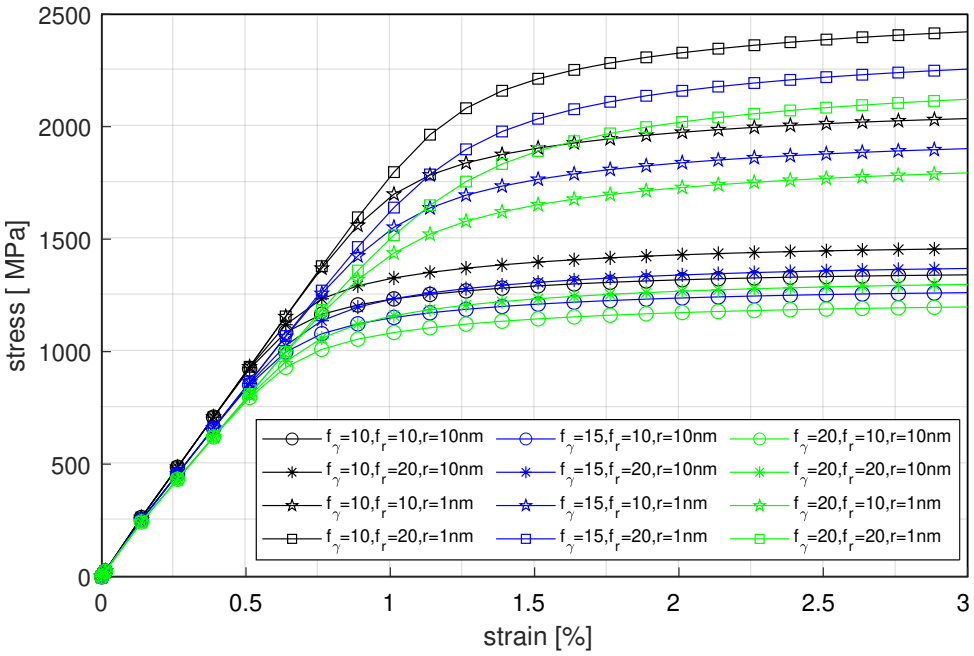


Figure 20: Engineering stress-strain curves for varying volume fractions of austenite f_γ [%], volume fraction of precipitates f_r [%] and precipitate sizes r [nm].

Here, σ_0 represents the solid solution strength together with the strength due to the presence of dislocations, k is proportional to the shear modulus ($\sim 0.1\mu$ (Galindo-Nava et al., 2016)), b is the Burger's vector, r is the average precipitate radius, σ_γ is the yield stress of austenite, and f_γ is the volume fraction of austenite. In a recent phase field simulation study, (Ahluwalia et al., 2024) proposed a rule of mixtures equation with $n = 1$ for predicting material strength based on the volume fraction and size of precipitates, as well as the volume fraction of austenite. Here, we aim to validate the applicability of these predictions to low carbon steel systems by examining the linearity of the homogenized response of the austenite-martensite RVE. Following the application of the least-square method for $n = 1$, the following values can be identified: $\sigma_0 = 1270.55$MPa, $\sigma_\gamma = -1129.38$MPa, and $k = 7210$MPa. Clearly, the extrapolation to $f_\gamma = 1$ in the case of $n = 1$ is not physical, as it results in a negative value of yield stress for austenite, σ_γ. Given the yield stress of a fully austenitic RVE is 130MPa when loaded along the $\langle 001 \rangle$ direction, the least-square method needs to be relaxed to also fit the exponent n. In such a case, $\sigma_0 = 1229.9$MPa, $\sigma_\gamma = 121.26$MPa, $k = 8330$MPa, and $n = 1.89$ with the sum of squared residuals $S = \sum_i r^2 = \sum_i \left(\sigma_y^{0.2\%} - \sigma_y^{LS}\right)^2 = 1.12$MPa. Hence, the overall response as a function of volume fraction of austenite f_γ is showing more of a quadratic rather than a linear trend.

We conclude this section by noting that while our focus has been on investigating the plastic flow while maintaining the microstructure intact (aside from lattice rotation due to plastic deformation), future studies may also explore the motion of martensitic interfaces and phase transformations. Such mechanisms, in systems like those presented here, are associated with the phenomenon of transformation-induced plasticity (TRIP), which has the potential to enhance both strength and ductility, properties that are typically inversely correlated (Raabe et al., 2009a). Research indicating this potential has been recently illustrated by (Zecevic et al., 2019), and (Feng et al., 2021), who employed mean-field self-consistent homogenization models in conjunction with phase fraction models capturing martensitic phase transformations.

10. Conclusions

In this study, we have developed an updated-Lagrangian finite element crystal plasticity model for maraging steel produced through additive manufacturing, specifically the powder-bed fusion (PBF) process. Alongside the crystal plasticity framework, we proposed a method for generating synthetic Representative Volume Elements (RVEs) that incorporate the characteristics of meltpool boundaries, prior austenite grains, and lath martensite microstructure. Using several examples, we have demonstrated the impact of various forms of the typical microstructure (inspired by experimental observations) on mechanical responses during uniaxial tensile and compressive loading. In this work, we focused on the effects associated with the intrinsic properties on the mechanical response. However, it is important to note that the model can also easily incorporate extrinsic properties, such as residual stresses, if given. The model is also applicable to other similar materials of low alloy steels exhibiting lath martensite pattern formations and retained austenite. Several key observations emerged from this study:

- A combination of the Potts Monte Carlo method and a simple segmentation algorithm can provide synthetic high-resolution RVEs of the hierarchical lath martensite microstructure. These RVEs were integrated with a crystal plasticity model for both bcc and fcc phases, providing insights into deformation, texture evolution, tension-compression asymmetry, and dislocation density evolution.

- The presence of small austenitic grains along the meltpool boundaries, typical in PBF, does not have a significant effect on the macroscopic stress-strain response measured up to 10% of strain. However, an increase in the volume fraction of reverted austenite during the heat-treatment process can significantly contribute to the mechanical response by decreasing the yield stress with quadratic rate.

- During tensile loading, plastic deformation occurs both in martensite and austenite, even when the reverted austenite content is as high as 20%). While the crystal orientation tends to align with the $\langle 011 \rangle$ direction in the martensite phase, austenite retains its $\langle 001 \rangle$ orientation.

- During the deformation, visible surface corrugations appear revealing the underlying martensitic microstructure consisting of individual blocks, a characteristic of the crystallographic aspects of martensitic variants.

- Dislocation density tends to localize near the block boundaries and near the austenite-martensite interfaces, especially in cases with large volume fractions of austenite, such as in heat-treated samples, but overall changes in dislocation densities are marginal. This is due to the already high levels of dislocation densities in as-printed samples.

11. Acknowledgements

This work was supported by the Agency for Science, Technology and Research (A*STAR) of Singapore with the Manufacturing, Trade and Connectivity (MTC) Grants "Advanced Models for Additive Manufacturing" (M22L2b0111) and "Industrial Digital Design and Additive Manufacturing Workflows" (A19E1a0097). This work was also supported by the A*STAR Computational Resource Centre through the use of its high performance computing facilities.

References

Ahluwalia, R., Mikula, J., Laskowski, R., Quek, S.S., 2020. Phase field simulation of martensitic-transformation-induced plasticity in steel. Phys. Rev. Mater. 4, 103607. URL: https://link.aps.org/doi/10.1103/PhysRevMaterials.4.103607, doi:10.1103/PhysRevMaterials.4.103607.

Ahluwalia, R., Mikula, J., Zeng, Y., Laskowski, R., Bai, K., Vastola, G., Zhang, Y.W., 2024. Phase field study of heat treatment and strengthening in maraging steels. Computational Materials Science 231, 112590. URL: https://www.sciencedirect.com/science/article/pii/S0927025623005840, doi:https://doi.org/10.1016/j.commatsci.2023.112590.

Bai, Y., Wang, D., Yang, Y., Wang, H., 2019. Effect of heat treatment on the microstructure and mechanical properties of maraging steel by selective laser melting. Materials Science and Engineering: A 760, 105–117. URL: https://www.sciencedirect.com/science/article/pii/S092150931930749X, doi:https://doi.org/10.1016/j.msea.2019.05.115.

Bajaj, P., Hariharan, A., Kini, A., Kürnsteiner, P., Raabe, D., Jägle, E., 2020. Steels in additive manufacturing: A review of their microstructure and properties. Materials Science and Engineering: A 772, 138633. URL: https://www.sciencedirect.com/science/article/pii/S0921509319314194, doi:https://doi.org/10.1016/j.msea.2019.138633.

Beyerlein, I., Tomé, C., 2008. A dislocation-based constitutive law for pure zr including temperature effects. International Journal of Plasticity 24, 867–895. URL: https://www.sciencedirect.com/science/article/pii/S074964190700109X, doi:https://doi.org/10.1016/j.ijplas.2007.07.017.

Bhardwaj, T., Shukla, M., 2018. Effect of laser scanning strategies on texture, physical and mechanical properties of laser sintered maraging steel. Materials Science and Engineering: A 734, 102–109. URL: https://www.sciencedirect.com/science/article/pii/S0921509318310244, doi:https://doi.org/10.1016/j.msea.2018.07.089.

Casalino, G., Campanelli, S., Contuzzi, N., Ludovico, A., 2015. Experimental investigation and statistical optimisation of the selective laser melting process of a maraging steel. Optics & Laser Technology 65, 151–158. URL: https://www.sciencedirect.com/science/article/pii/S0030399214002011, doi:https://doi.org/10.1016/j.optlastec.2014.07.021.

Chadha, K., Tian, Y., Bocher, P., Spray, J.G., Aranas, C., 2020. Microstructure evolution, mechanical properties and deformation behavior of an additively manufactured maraging steel. Materials 13. URL: https://www.mdpi.com/1996-1944/13/10/2380, doi:10.3390/ma13102380.

Chen, W., Voisin, T., Zhang, Y., Forien, J.B., Spadaccini, C.M., McDowell, D.L., Zhu, T., Wang, Y.M., 2019. Microscale residual stresses in additively manufactured stainless steel. Nature Communications 10, 4338. URL: https://doi.org/10.1038/s41467-019-12265-8, doi:10.1038/s41467-019-12265-8.

Chen, Z.M., Mrovec, M., Gumbsch, P., 2013. Atomistic aspects of screw dislocation behavior in α-iron and the derivation of microscopic yield criterion. Modelling and Simulation in Materials Science and Engineering 21, 055023. URL: https://dx.doi.org/10.1088/0965-0393/21/5/055023, doi:10.1088/0965-0393/21/5/055023.

Cheng, B., Wei, F., Teh, W.H., Cheong, K.H., Lee, J.J., Chew, L.T., Lau, K.B., Ma, T.H.B., Ng, C.K., Wang, P., Ramamurty, U., Tan, C.C., 2023. High strength hadfield steel produced using laser powder bed fusion of mixed powders. Materials & Design 231, 112017. URL: https://www.sciencedirect.com/science/article/pii/S026412752300432X, doi:https://doi.org/10.1016/j.matdes.2023.112017.

Christian, J.W., 1983. Some surprising features of the plastic deformation of body-centered cubic metals and alloys. Metallurgical Transactions A 14, 1237–1256. URL: http://dx.doi.org/10.1007/BF02664806, doi:10.1007/bf02664806.

Conde, F., Escobar, J., Oliveira, J., Jardini, A., Bose Filho, W., Avila, J., 2019. Austenite reversion kinetics and stability during tempering of an additively manufactured maraging 300 steel. Additive Manufacturing 29, 100804. URL: https://www.sciencedirect.com/science/article/pii/S2214860418308030, doi:https://doi.org/10.1016/j.addma.2019.100804.

Cyr, E., Lloyd, A., Mohammadi, M., 2018. Tension-compression asymmetry of additively manufactured maraging steel. Journal of Manufacturing Processes 35, 289–294. URL: https://www.sciencedirect.com/science/article/pii/S1526612518311514, doi:https://doi.org/10.1016/j.jmapro.2018.08.015.

Dao, M., Asaro, R., 1993. Non-schmid effects and localized plastic flow in intermetallic alloys. Materials Science and Engineering: A 170, 143–160. URL: https://www.sciencedirect.com/science/article/pii/092150939390376P, doi:https://doi.org/10.1016/0921-5093(93)90376-P.

Daroju, S., Kuwabara, T., Knezevic, M., 2022. Experimental characterization and crystal plasticity modeling of dual-phase steels subjected to strain path reversals. Mechanics of Materials 168, 104293. URL: https://www.sciencedirect.com/science/article/pii/S016766362200076X, doi:https://doi.org/10.1016/j.mechmat.2022.104293.

Demir, A.G., Previtali, B., 2017. Investigation of remelting and preheating in slm of 18ni300 maraging steel as corrective and preventive measures for porosity reduction. The International Journal of Advanced Manufacturing Technology 93, 2697–2709. URL: https://doi.org/10.1007/s00170-017-0697-z, doi:10.1007/s00170-017-0697-z.

Du, C., Hoefnagels, J., Vaes, R., Geers, M., 2016. Block and sub-block boundary strengthening in lath martensite. Scripta Materialia 116, 117–121. URL: https://www.sciencedirect.com/science/article/pii/S1359646216300434, doi:https://doi.org/10.1016/j.scriptamat.2016.01.043.

Du, C., Maresca, F., Geers, M., Hoefnagels, J., 2018. Ferrite slip system activation investigated by uniaxial micro-tensile tests and simulations. Acta Materialia 146, 314–327. URL: https://www.sciencedirect.com/science/article/pii/S1359645418300107, doi:https://doi.org/10.1016/j.actamat.2017.12.054.

Eghtesad, A., Knezevic, M., 2020. High-performance full-field crystal plasticity with dislocation-based hardening and slip system back-stress laws: Application to modeling deformation of dual-phase steels. Journal of the Mechanics and Physics of Solids 134, 103750. URL: https://www.sciencedirect.com/science/article/pii/S0022509619305812, doi:https://doi.org/10.1016/j.jmps.2019.103750.

Fayazfar, H., Salarian, M., Rogalsky, A., Sarker, D., Russo, P., Paserin, V., Toyserkani, E., 2018. A critical review of powder-based additive manufacturing of ferrous alloys: Process parameters, microstructure and mechanical properties. Materials &

Design 144, 98–128. URL: https://www.sciencedirect.com/science/article/pii/S0264127518300972, doi:https://doi.org/10.1016/j.matdes.2018.02.018.

Feng, Z., Zecevic, M., Knezevic, M., 2021. Stress-assisted ($\gamma-\alpha'$) and strain-induced ($\gamma-\epsilon-\alpha'$) phase transformation kinetics laws implemented in a crystal plasticity model for predicting strain path sensitive deformation of austenitic steels. International Journal of Plasticity 136, 102807. URL: https://www.sciencedirect.com/science/article/pii/S0749641919309362, doi:https://doi.org/10.1016/j.ijplas.2020.102807.

Fischer, T., Dahlberg, C.F., Hedström, P., 2023. Sensitivity of local cyclic deformation in lath martensite to flow rule and slip system in crystal plasticity. Computational Materials Science 222, 112106. URL: https://www.sciencedirect.com/science/article/pii/S0927025623001003, doi:https://doi.org/10.1016/j.commatsci.2023.112106.

Franciosi, P., Berveiller, M., Zaoui, A., 1980. Latent hardening in copper and aluminium single crystals. Acta Metallurgica 28, 273–283. URL: https://www.sciencedirect.com/science/article/pii/0001616080901625, doi:https://doi.org/10.1016/0001-6160(80)90162-5.

Galindo-Nava, E., Rainforth, W., del Castillo, P.R.D., 2016. Predicting microstructure and strength of maraging steels: Elemental optimisation. Acta Materialia 117, 270–285. URL: https://www.sciencedirect.com/science/article/pii/S135964541630516X, doi:https://doi.org/10.1016/j.actamat.2016.07.020.

Gallardo-Basile, F.J., Naunheim, Y., Roters, F., Diehl, M., 2021. Lath martensite microstructure modeling: A high-resolution crystal plasticity simulation study. Materials 14. URL: https://www.mdpi.com/1996-1944/14/3/691, doi:10.3390/ma14030691.

Ghassemi-Armaki, H., Chen, P., Bhat, S., Sadagopan, S., Kumar, S., Bower, A., 2013. Microscale-calibrated modeling of the deformation response of low-carbon martensite. Acta Materialia 61, 3640–3652. URL: https://www.sciencedirect.com/science/article/pii/S135964541300181X, doi:https://doi.org/10.1016/j.actamat.2013.02.051.

Ghorbanpour, S., Alam, M.E., Ferreri, N.C., Kumar, A., McWilliams, B.A., Vogel, S.C., Bicknell, J., Beyerlein, I.J., Knezevic, M., 2020. Experimental characterization and crystal plasticity modeling of anisotropy, tension-compression asymmetry, and texture evolution of additively manufactured inconel 718 at room and elevated temperatures. International Journal of Plasticity 125, 63–79. URL: https://www.sciencedirect.com/science/article/pii/S074964191930347X, doi:https://doi.org/10.1016/j.ijplas.2019.09.002.

Ghorbanpour, S., Zecevic, M., Kumar, A., Jahedi, M., Bicknell, J., Jorgensen, L., Beyerlein, I.J., Knezevic, M., 2017. A crystal plasticity model incorporating the effects of precipitates in superalloys: Application to tensile, compressive, and cyclic deformation of inconel 718. International Journal of Plasticity 99, 162–185. URL: https://www.sciencedirect.com/science/article/pii/S0749641917303182, doi:https://doi.org/10.1016/j.ijplas.2017.09.006.

Gong, P., Wynne, B.P., Knowles, A.J., Turk, A., Ma, L., Galindo-Nava, E.I., Rainforth, W.M., 2020. Effect of ageing on the microstructural evolution in a new design of maraging steels with carbon. Acta Materialia 196, 101–121. URL: https://www.sciencedirect.com/science/article/pii/S135964542030464X, doi:https://doi.org/10.1016/j.actamat.2020.06.029.

Govindaraj, V., Hodgson, P., P Singh, R., Beladi, H., 2021. The effect of austenite reversion on the microstructure and mechanical properties of a 12cr–3ni–3mn–3cu-0.15nb–0.05c maraging stainless steel. Materials Science and Engineering: A 828, 142097. URL: https://www.sciencedirect.com/science/article/pii/S0921509321013617, doi:https://doi.org/10.1016/j.msea.2021.142097.

Groeber, M.A., Jackson, M.A., 2014. Dream.3d: A digital representation environment for the analysis of microstructure in 3d. Integrating Materials and Manufacturing Innovation 3, 56–72. URL: https://doi.org/10.1186/2193-9772-3-5, doi:10.1186/2193-9772-3-5.

Gröger, R., Bailey, A., Vitek, V., 2008a. Multiscale modeling of plastic deformation of molybdenum and tungsten: I. atomistic studies of the core structure and glide of $1/2\langle111\rangle$ screw dislocations at 0k. Acta Materialia 56, 5401–5411. URL: https://www.sciencedirect.com/science/article/pii/S1359645408005132, doi:https://doi.org/10.1016/j.actamat.2008.07.018.

Gröger, R., Racherla, V., Bassani, J., Vitek, V., 2008b. Multiscale modeling of plastic deformation of molybdenum and tungsten: Ii. yield criterion for single crystals based on atomistic studies of glide of $1/2\langle111\rangle$ screw dislocations. Acta Materialia 56, 5412–5425. URL: https://www.sciencedirect.com/science/article/pii/S1359645408005144, doi:https://doi.org/10.1016/j.actamat.2008.07.037.

Gröger, R., Vitek, V., 2005. Breakdown of the schmid law in bcc molybdenum related to the effect of shear stress perpendicular to the slip direction. Materials Science Forum 482. doi:https://doi.org/10.4028/www.scientific.net/MSF.482.123.

Gröger, R., Vitek, V., 2008. Multiscale modeling of plastic deformation of molybdenum and tungsten. iii. effects of temperature and plastic strain rate. Acta Materialia 56, 5426–5439. URL: https://www.sciencedirect.com/science/article/pii/S1359645408005156, doi:https://doi.org/10.1016/j.actamat.2008.07.027.

Gröger, R., Vitek, V., 2009. Temperature and strain rate dependent flow criterion for bcc transition metals based on atomistic analysis of dislocation glide. International Journal of Materials Research 100, 315–321. URL: https://doi.org/10.3139/146.110046, doi:doi:10.3139/146.110046.

Gröger, R., Vitek, V., Lookman, T., 2017. Mesoscale plastic texture in body-centered cubic metals under uniaxial load. Phys. Rev. Materials 1, 063601. URL: https://link.aps.org/doi/10.1103/PhysRevMaterials.1.063601, doi:10.1103/PhysRevMaterials.1.063601.

Gröger, R., 2014. Which stresses affect the glide of screw dislocations in bcc metals? Philosophical Magazine 94, 2021–2030. URL: https://doi.org/10.1080/14786435.2014.904058, doi:10.1080/14786435.2014.904058, arXiv:https://doi.org/10.1080/14786435.2014.904058.

Gröger, R., 2021. Symmetry-adapted single crystal yield criterion for non-schmid materials. International Journal of Plasticity 146, 103101. URL: https://www.sciencedirect.com/science/article/pii/S0749641921001704, doi:https://doi.org/10.1016/j.ijplas.2021.103101.

Gröger, R., Vitek, V., 2020. Single crystal yield criterion for chromium based on atomistic studies of isolated 1/2[111] screw dislocations. International Journal of Plasticity 132, 102733. URL: https://www.sciencedirect.com/science/article/pii/S0749641919308940, doi:https://doi.org/10.1016/j.ijplas.2020.102733.
Guennebaud, G., Jacob, B., et al., 2010. Eigen v3. http://eigen.tuxfamily.org.
Guo, L., Zhang, L., Andersson, J., Ojo, O., 2022. Additive manufacturing of 18% nickel maraging steels: Defect, structure and mechanical properties: A review. Journal of Materials Science & Technology 120, 227–252. URL: https://www.sciencedirect.com/science/article/pii/S1005030222001827, doi:https://doi.org/10.1016/j.jmst.2021.10.056.
Hall, A., Slunder, C., Institute, B.M., 1968. The Metallurgy, Behavior, and Application of the 18-percent Nickel Maraging Steels: A Survey. NASA SP, Technology Utilization Division, National Aeronautics and Space Administration. URL: https://books.google.com.sg/books?id=NLIgAAAAIAAJ.
Hirth, J.P., Lothe, J., Mura, T., 1983. Theory of dislocations. Journal of Applied Mechanics 50, 476.
Holm, E.A., Battaile, C.C., 2001. The computer simulation of microstructural evolution. JOM 53, 20–23. URL: https://doi.org/10.1007/s11837-001-0063-2, doi:10.1007/s11837-001-0063-2.
Hu, D., Guo, Z., Grilli, N., Tay, A., Lu, Z., Yan, W., 2024. Understanding the strain localization in additively manufactured materials: Micro-scale tensile tests and crystal plasticity modeling. International Journal of Plasticity 177, 103981. URL: https://www.sciencedirect.com/science/article/pii/S0749641924001086, doi:https://doi.org/10.1016/j.ijplas.2024.103981.
Hull, D., Bacon, D., 2011. Chapter 6 - dislocations in other crystal structures, in: Hull, D., Bacon, D. (Eds.), Introduction to Dislocations (Fifth Edition). fifth edition ed.. Butterworth-Heinemann, Oxford, pp. 109–136. URL: https://www.sciencedirect.com/science/article/pii/B9780080966724000062, doi:https://doi.org/10.1016/B978-0-08-096672-4.00006-2.
Jägle, E.A., Choi, P.P., Van Humbeeck, J., Raabe, D., 2014. Precipitation and austenite reversion behavior of a maraging steel produced by selective laser melting. Journal of Materials Research 29, 2072–2079. doi:10.1557/jmr.2014.204.
Jägle, E.A., Sheng, Z., Kürnsteiner, P., Ocylok, S., Weisheit, A., Raabe, D., 2017. Comparison of maraging steel micro- and nanostructure produced conventionally and by laser additive manufacturing. Materials 10. URL: https://www.mdpi.com/1996-1944/10/1/8, doi:10.3390/ma10010008.
Kannan, R., Nandwana, P., 2022. Texture evolution during processing and post-processing of maraging steel fabricated by laser powder bed fusion. Scientific Reports 12. URL: http://dx.doi.org/10.1038/s41598-022-09977-1, doi:10.1038/s41598-022-09977-1.
Keh, A.S., 1965. Work hardening and deformation sub-structure in iron single crystals deformed in tension at 298°k. The Philosophical Magazine: A Journal of Theoretical Experimental and Applied Physics 12, 9–30. URL: https://doi.org/10.1080/14786436508224942, doi:10.1080/14786436508224942, arXiv:https://doi.org/10.1080/14786436508224942.
Kempen, K., Yasa, E., Thijs, L., Kruth, J.P., Van Humbeeck, J., 2011. Microstructure and mechanical properties of selective laser melted 18ni-300 steel. Physics Procedia 12, 255–263. URL: https://www.sciencedirect.com/science/article/pii/S187538921100112X, doi:https://doi.org/10.1016/j.phpro.2011.03.033. lasers in Manufacturing 2011 - Proceedings of the Sixth International WLT Conference on Lasers in Manufacturing.
Kitahara, H., Ueji, R., Tsuji, N., Minamino, Y., 2006. Crystallographic features of lath martensite in low-carbon steel. Acta Materialia 54, 1279–1288. URL: https://www.sciencedirect.com/science/article/pii/S1359645405006701, doi:https://doi.org/10.1016/j.actamat.2005.11.001.
Kizhakkinan, U., Seetharaman, S., Raghavan, N., Rosen, D.W., 2023. Laser Powder Bed Fusion Additive Manufacturing of Maraging Steel: A Review. Journal of Manufacturing Science and Engineering 145, 110801. URL: https://doi.org/10.1115/1.4062727, doi:10.1115/1.4062727, arXiv:https://asmedigitalcollection.asme.org/manufacturingscience/article-pdf/145/11/110801/7032844/manu_145_11_110801.pdf.
Kljestan, N., McWilliams, B.A., Knezevic, M., 2024. Fatigue strength of an ultra-high strength low alloy steel fabricated via laser powder bed fusion. Materials Science and Engineering: A 896, 146269. URL: https://www.sciencedirect.com/science/article/pii/S0921509324002004, doi:https://doi.org/10.1016/j.msea.2024.146269.
Kocks, U., Argon, A., Ashby, M., 1975. Thermodynamics and Kinetics of Slip. Progress in materials science, Pergamon Press. URL: https://books.google.com.sg/books?id=B0AkMgEACAAJ.
Kocks, U.F., 1987. Unified Constitutive Equations for Creep and Plasticity. Springer Netherlands, Dordrecht. chapter Constitutive Behavior Based on Crystal Plasticity. pp. 1–88. URL: https://doi.org/10.1007/978-94-009-3439-9_1, doi:10.1007/978-94-009-3439-9_1.
Koester, A., Ma, A., Hartmaier, A., 2012. Atomistically informed crystal plasticity model for body-centered cubic iron. Acta Materialia 60, 3894–3901. URL: https://www.sciencedirect.com/science/article/pii/S1359645412002431, doi:https://doi.org/10.1016/j.actamat.2012.03.053.
Koumatos, K., Muehlemann, A., 2017. A theoretical investigation of orientation relationships and transformation strains in steels. Acta Crystallographica Section A 73, 115–123. URL: https://onlinelibrary.wiley.com/doi/abs/10.1107/S2053273316020350, doi:https://doi.org/10.1107/S2053273316020350, arXiv:https://onlinelibrary.wiley.com/doi/pdf/10.1107/S2053273316020350.
Kurdjumow, G., Sachs, G., 1930. Über den mechanismus der stahlhärtung. Zeitschrift für Physik 64, 325–343. URL: http://dx.doi.org/10.1007/BF01397346, doi:10.1007/bf01397346.
Lim, H., Battaile, C.C., Carroll, J.D., Boyce, B.L., Weinberger, C.R., 2015. A physically based model of temperature and strain rate dependent yield in bcc metals: Implementation into crystal plasticity. Journal of the Mechanics and Physics of Solids 74, 80–96. URL: https://www.sciencedirect.com/science/article/pii/S0022509614002014, doi:https://doi.org/10.1016/j.jmps.2014.10.003.
Lim, H., Weinberger, C.R., Battaile, C.C., Buchheit, T.E., 2013. Application of generalized non-schmid yield law to low-

temperature plasticity in bcc transition metals. Modelling and Simulation in Materials Science and Engineering 21, 045015. URL: https://dx.doi.org/10.1088/0965-0393/21/4/045015, doi:10.1088/0965-0393/21/4/045015.
Lindroos, M., Pinomaa, T., Ammar, K., Laukkanen, A., Provatas, N., Forest, S., 2022. Dislocation density in cellular rapid solidification using phase field modeling and crystal plasticity. International Journal of Plasticity 148, 103139. URL: https://www.sciencedirect.com/science/article/pii/S0749641921002072, doi:https://doi.org/10.1016/j.ijplas.2021.103139.
Liu, P., Wang, Z., Xiao, Y., Lebensohn, R., Liu, Y., Horstemeyer, M., Cui, X., Chen, L., 2020. Integration of phase-field model and crystal plasticity for the prediction of process-structure-property relation of additively manufactured metallic materials. International Journal of Plasticity 128, 102670. URL: https://www.sciencedirect.com/science/article/pii/S0749641919305017, doi:https://doi.org/10.1016/j.ijplas.2020.102670.
Liu, T., Liang, L., Raabe, D., Dai, L., 2023. The martensitic transition pathway in steel. Journal of Materials Science & Technology 134, 244–253. URL: https://www.sciencedirect.com/science/article/pii/S1005030222005655, doi:https://doi.org/10.1016/j.jmst.2022.06.023.
Lu, X., Zhang, X., Shi, M., Roters, F., Kang, G., Raabe, D., 2019. Dislocation mechanism based size-dependent crystal plasticity modeling and simulation of gradient nano-grained copper. International Journal of Plasticity 113, 52–73. URL: https://www.sciencedirect.com/science/article/pii/S074964191830264X, doi:https://doi.org/10.1016/j.ijplas.2018.09.007.
Macchi, J., Gaudez, S., Geandier, G., Teixeira, J., Denis, S., Bonnet, F., Allain, S.Y., 2021. Dislocation densities in a low-carbon steel during martensite transformation determined by in situ high energy x-ray diffraction. Materials Science and Engineering: A 800, 140249. URL: https://www.sciencedirect.com/science/article/pii/S0921509320313149, doi:https://doi.org/10.1016/j.msea.2020.140249.
Mackenzie, J.K., 1958. Second paper on statistics associated with the random disorientation of cubes. Biometrika 45, 229–240. URL: http://www.jstor.org/stable/2333059.
Mackenzie, J.K., Thomson, M.J., 1957. Some statistics associated with the random disorientation of cubes. Biometrika 44, 205–210. URL: http://www.jstor.org/stable/2333253.
Madec, R., Kubin, L.P., 2004. Dislocation interactions and symmetries in bcc crystals, in: Kitagawa, H., Shibutani, Y. (Eds.), IUTAM Symposium on Mesoscopic Dynamics of Fracture Process and Materials Strength, Springer Netherlands, Dordrecht. pp. 69–78.
Madec, R., Kubin, L.P., 2017. Dislocation strengthening in fcc metals and in bcc metals at high temperatures. Acta Materialia 126, 166–173. URL: https://www.sciencedirect.com/science/article/pii/S1359645416309764, doi:https://doi.org/10.1016/j.actamat.2016.12.040.
Maki, T., 2012. 2 - morphology and substructure of martensite in steels, in: Pereloma, E., Edmonds, D.V. (Eds.), Phase Transformations in Steels. Woodhead Publishing. volume 2 of *Woodhead Publishing Series in Metals and Surface Engineering*, pp. 34–58. URL: https://www.sciencedirect.com/science/article/pii/B9781845699710500028, doi:https://doi.org/10.1533/9780857096111.1.34.
Maresca, F., 2015. Multi-scale modeling of plasticity and damage of lath martensite in multi-phase steels. Ph.D. thesis. Mechanical Engineering. Proefschrift.
Maresca, F., Kouznetsova, V., Geers, M., 2014. Subgrain lath martensite mechanics: A numerical–experimental analysis. Journal of the Mechanics and Physics of Solids 73, 69–83. URL: https://www.sciencedirect.com/science/article/pii/S002250961400180X, doi:https://doi.org/10.1016/j.jmps.2014.09.002.
Marichal, C., Van Swygenhoven, H., Van Petegem, S., Borca, C., 2013. {110} slip with {112} slip traces in bcc tungsten. Scientific Reports 3, 2547. URL: https://doi.org/10.1038/srep02547, doi:10.1038/srep02547.
Matsukawa, Y., 2019. Crystallography of precipitates in metals and alloys: (2) impact of crystallography on precipitation hardening, in: Akitsu, T. (Ed.), Crystallography. IntechOpen, Rijeka. chapter 3. URL: https://doi.org/10.5772/intechopen.84273, doi:10.5772/intechopen.84273.
Mecking, H., Kocks, U., 1981. Kinetics of flow and strain-hardening. Acta Metallurgica 29, 1865–1875. URL: https://www.sciencedirect.com/science/article/pii/0001616081901127, doi:https://doi.org/10.1016/0001-6160(81)90112-7.
Mikula, J., Laskowski, R., Dai, L., Ding, W., Wei, M., Bai, K., Wang, K., Hariharaputran, R., Ahuwalia, R., Vastola, G., Zhang, Y.W., 2021. Advanced "digital twin"platform for powder-bed fusion additive manufacturing. Hitachi Technical Review 37.
Miles, R.E., 1965. On random rotations in R3. Biometrika 52, 636–639. URL: https://doi.org/10.1093/biomet/52.3-4.636, doi:10.1093/biomet/52.3-4.636, arXiv:https://academic.oup.com/biomet/article-pdf/52/3-4/636/963000/52-3-4-636.pdf.
Miodownik, M., 2007. 3 - monte carlo potts model, in: JANSSENS, K.G., RAABE, D., KOZESCHNIK, E., MIODOWNIK, M.A., NESTLER, B. (Eds.), Computational Materials Engineering. Academic Press, Burlington, pp. 47–108. URL: https://www.sciencedirect.com/science/article/pii/B9780123694683500034, doi:https://doi.org/10.1016/B978-012369468-3/50003-4.
Mooney, B., Kourousis, K.I., Raghavendra, R., 2019. Plastic anisotropy of additively manufactured maraging steel: Influence of the build orientation and heat treatments. Additive Manufacturing 25, 19–31. URL: https://www.sciencedirect.com/science/article/pii/S2214860418305542, doi:https://doi.org/10.1016/j.addma.2018.10.032.
Morito, S., Huang, X., Furuhara, T., Maki, T., Hansen, N., 2006. The morphology and crystallography of lath martensite in alloy steels. Acta Materialia 54, 5323–5331. URL: https://www.sciencedirect.com/science/article/pii/S1359645406005076, doi:https://doi.org/10.1016/j.actamat.2006.07.009.
Morito, S., Tanaka, H., Konishi, R., Furuhara, T., Maki, T., 2003. The morphology and crystallography of lath martensite in fe-c alloys. Acta Materialia 51, 1789–1799. URL: https://www.sciencedirect.com/science/article/pii/S1359645402005773, doi:https://doi.org/10.1016/S1359-6454(02)00577-3.
Morsdorf, L., Jeannin, O., Barbier, D., Mitsuhara, M., Raabe, D., Tasan, C., 2016. Multiple mechanisms of lath martensite plasticity. Acta Materialia 121, 202–214. URL: https://www.sciencedirect.com/science/article/pii/S1359645416306851,

doi:https://doi.org/10.1016/j.actamat.2016.09.006.
Motaman, S.A.H., Roters, F., Haase, C., 2020. Anisotropic polycrystal plasticity due to microstructural heterogeneity: A multi-scale experimental and numerical study on additively manufactured metallic materials. Acta Materialia 185, 340–369. URL: https://www.sciencedirect.com/science/article/pii/S1359645419308298, doi:https://doi.org/10.1016/j.actamat.2019.12.003.
Mutua, J., Nakata, S., Onda, T., Chen, Z.C., 2018. Optimization of selective laser melting parameters and influence of post heat treatment on microstructure and mechanical properties of maraging steel. Materials & Design 139, 486–497. URL: https://www.sciencedirect.com/science/article/pii/S0264127517310730, doi:https://doi.org/10.1016/j.matdes.2017.11.042.
Narayanan, S., McDowell, D.L., Zhu, T., 2014. Crystal plasticity model for bcc iron atomistically informed by kinetics of correlated kinkpair nucleation on screw dislocation. Journal of the Mechanics and Physics of Solids 65, 54–68. URL: https://www.sciencedirect.com/science/article/pii/S0022509614000143, doi:https://doi.org/10.1016/j.jmps.2014.01.004.
Nishiyama, Z., 1934. X-ray investigation of the mechanism of the transformation from face centered cubic lattice to body centered cubic. Sci. Rep. Tohoku Univ. 23, 637. URL: https://cir.nii.ac.jp/crid/1570854175128630400.
Nolze, G., Hielscher, R., 2016. Orientations – perfectly colored. Journal of Applied Crystallography 49, 1786–1802. URL: https://onlinelibrary.wiley.com/doi/abs/10.1107/S1600576716012942, doi:https://doi.org/10.1107/S1600576716012942, arXiv:https://onlinelibrary.wiley.com/doi/pdf/10.1107/S1600576716012942.
Patra, A., Zhu, T., McDowell, D.L., 2014. Constitutive equations for modeling non-schmid effects in single crystal bcc-fe at low and ambient temperatures. International Journal of Plasticity 59, 1–14. URL: https://www.sciencedirect.com/science/article/pii/S0749641914000667, doi:https://doi.org/10.1016/j.ijplas.2014.03.016.
Pinz, M., Benzing, J., Pilchak, A., Ghosh, S., 2022. A microstructure-based porous crystal plasticity fe model for additively manufactured ti-6al-4v alloys. International Journal of Plasticity 153, 103254. URL: https://www.sciencedirect.com/science/article/pii/S0749641922000389, doi:https://doi.org/10.1016/j.ijplas.2022.103254.
Qin, Q., Bassani, J.L., 1992. Non-schmid yield behavior in single crystals. Journal of the Mechanics and Physics of Solids 40, 813–833. URL: https://www.sciencedirect.com/science/article/pii/002250969290005M, doi:https://doi.org/10.1016/0022-5096(92)90005-M.
Quey, R., Kasemer, M., 2022. The neper/fepx project: Free / open-source polycrystal generation, deformation simulation, and post-processing. IOP Conference Series: Materials Science and Engineering 1249, 012021. URL: https://dx.doi.org/10.1088/1757-899X/1249/1/012021, doi:10.1088/1757-899X/1249/1/012021.
Queyreau, S., Monnet, G., Devincre, B., 2009. Slip systems interactions in α-iron determined by dislocation dynamics simulations. International Journal of Plasticity 25, 361–377. URL: https://www.sciencedirect.com/science/article/pii/S0749641908000107, doi:https://doi.org/10.1016/j.ijplas.2007.12.009.
Raabe, D., 1995. Simulation of rolling textures of b.c.c. metals considering grain interactions and crystallographic slip on 110, 112 and 123 planes. Materials Science and Engineering: A 197, 31–37. URL: https://www.sciencedirect.com/science/article/pii/0921509394097704, doi:https://doi.org/10.1016/0921-5093(94)09770-4.
Raabe, D., Ponge, D., Dmitrieva, O., Sander, B., 2009a. Designing ultrahigh strength steels with good ductility by combining transformation induced plasticity and martensite aging. Advanced Engineering Materials 11, 547–555. URL: https://onlinelibrary.wiley.com/doi/abs/10.1002/adem.200900061, doi:https://doi.org/10.1002/adem.200900061, arXiv:https://onlinelibrary.wiley.com/doi/pdf/10.1002/adem.200900061.
Raabe, D., Ponge, D., Dmitrieva, O., Sander, B., 2009b. Nanoprecipitate-hardened 1.5gpa steels with unexpected high ductility. Scripta Materialia 60, 1141–1144. URL: https://www.sciencedirect.com/science/article/pii/S1359646209001626, doi:https://doi.org/10.1016/j.scriptamat.2009.02.062. viewpoint set no. 45 "Nanostructured metals: Advances in Processing, Characterization and Applications.
Savage, D.J., Beyerlein, I.J., Knezevic, M., 2017. Coupled texture and non-schmid effects on yield surfaces of body-centered cubic polycrystals predicted by a crystal plasticity finite element approach. International Journal of Solids and Structures 109, 22–32. URL: https://www.sciencedirect.com/science/article/pii/S0020768317300021, doi:https://doi.org/10.1016/j.ijsolstr.2017.01.003.
Schmid, E., Boas, W., 1950. Plasticity of crystals. The Aeronautical Journal 54, 718–719. doi:10.1017/S0368393100116219.
Schnitzer, R., Zinner, S., Leitner, H., 2010. Modeling of the yield strength of a stainless maraging steel. Scripta Materialia 62, 286–289. URL: https://www.sciencedirect.com/science/article/pii/S1359646209007325, doi:https://doi.org/10.1016/j.scriptamat.2009.11.020.
Schroeder, W., Martin, K., Lorensen, B., 2006. The Visualization Toolkit (4th ed.). Kitware.
Schäfer, B.J., Song, X., Sonnweber-Ribic, P., ul Hassan, H., Hartmaier, A., 2019. Micromechanical modelling of the cyclic deformation behavior of martensitic sae 4150—a comparison of different kinematic hardening models. Metals 9. URL: https://www.mdpi.com/2075-4701/9/3/368, doi:10.3390/met9030368.
Sedighiani, K., Traka, K., Roters, F., Raabe, D., Sietsma, J., Diehl, M., 2022. Determination and analysis of the constitutive parameters of temperature-dependent dislocation-density-based crystal plasticity models. Mechanics of Materials 164, 104117. URL: https://www.sciencedirect.com/science/article/pii/S016766362100332X, doi:https://doi.org/10.1016/j.mechmat.2021.104117.
Seeger, A., 1981. The temperature and strain-rate dependence of the flow stress of body-centred cubic metals: A theory based on kink-kink interactions. International Journal of Materials Research 72, 369–380. URL: https://doi.org/10.1515/ijmr-1981-720601, doi:doi:10.1515/ijmr-1981-720601.
Seeger, A., 2001. Why anomalous slip in body-centred cubic metals? Materials Science and Engineering: A 319-321, 254–260. URL: https://www.sciencedirect.com/science/article/pii/S0921509301009583, doi:https://doi.org/10.1016/

S0921-5093(01)00958-3.
Seeger, A., 2004. Experimental evidence for the 110 ↔ 112 transformation of the screw-dislocation cores in body-centred cubic metals. physica status solidi (a) 201, R21–R24. URL: https://onlinelibrary.wiley.com/doi/abs/10.1002/pssa.200409031, doi:https://doi.org/10.1002/pssa.200409031, arXiv:https://onlinelibrary.wiley.com/doi/pdf/10.1002/pssa.200409031.
Shamsdini, S., Ghoncheh, M., Sanjari, M., Pirgazi, H., Amirkhiz, B.S., Kestens, L., Mohammadi, M., 2021. Plastic deformation throughout strain-induced phase transformation in additively manufactured maraging steels. Materials & Design 198, 109289. URL: https://www.sciencedirect.com/science/article/pii/S026412752030825X, doi:https://doi.org/10.1016/j.matdes.2020.109289.
Shchyglo, O., Du, G., Engels, J.K., Steinbach, I., 2019. Phase-field simulation of martensite microstructure in low-carbon steel. Acta Materialia 175, 415–425. URL: https://www.sciencedirect.com/science/article/pii/S1359645419304094, doi:https://doi.org/10.1016/j.actamat.2019.06.036.
Shmulevitsh, M., Meshi, L., Pinkas, M., Shneck, R.Z., 2015. Elastic consideration of the precipitation in model alloys of maraging steels: theory and experimental validation. Journal of Materials Science 50, 4970–4979. URL: http://dx.doi.org/10.1007/s10853-015-9044-7, doi:10.1007/s10853-015-9044-7.
Kwiatkowski da Silva, A., Souza Filho, I.R., Lu, W., Zilnyk, K.D., Hupalo, M.F., Alves, L.M., Ponge, D., Gault, B., Raabe, D., 2022. A sustainable ultra-high strength fe18mn3ti maraging steel through controlled solute segregation and α-mn nanoprecipitation. Nature Communications 13. URL: http://dx.doi.org/10.1038/s41467-022-30019-x, doi:10.1038/s41467-022-30019-x.
Suryawanshi, J., Prashanth, K., Ramamurty, U., 2017. Tensile, fracture, and fatigue crack growth properties of a 3d printed maraging steel through selective laser melting. Journal of Alloys and Compounds 725, 355–364. URL: https://www.sciencedirect.com/science/article/pii/S0925838817325537, doi:https://doi.org/10.1016/j.jallcom.2017.07.177.
Takata, N., Ito, Y., Nishida, R., Suzuki, A., Kobashi, M., Kato, M., 2023. Austenite reversion behavior of maraging steel additive-manufactured by laser powder bed fusion. Tetsu-to-Hagane 109, 201–214. doi:10.2355/tetsutohagane.TETSU-2022-066.
Takata, N., Nishida, R., Suzuki, A., Kobashi, M., Kato, M., 2018. Crystallographic features of microstructure in maraging steel fabricated by selective laser melting. Metals 8. URL: https://www.mdpi.com/2075-4701/8/6/440, doi:10.3390/met8060440.
Tan, C., Zhou, K., Kuang, M., Ma, W., Kuang, T., 2018. Microstructural characterization and properties of selective laser melted maraging steel with different build directions. Science and Technology of Advanced Materials 19, 746–758. URL: https://doi.org/10.1080/14686996.2018.1527645, doi:10.1080/14686996.2018.1527645, arXiv:https://doi.org/10.1080/14686996.2018.1527645.
Tang, M., Kubin, L., Canova, G., 1998. Dislocation mobility and the mechanical response of b.c.c. single crystals: A mesoscopic approach. Acta Materialia 46, 3221–3235. URL: https://www.sciencedirect.com/science/article/pii/S1359645498000068, doi:https://doi.org/10.1016/S1359-6454(98)00006-8.
Taylor, G.I., 1934. The mechanism of plastic deformation of crystals. part i.—theoretical. Proceedings of the Royal Society of London. Series A, Containing Papers of a Mathematical and Physical Character 145, 362–387. URL: https://royalsocietypublishing.org/doi/abs/10.1098/rspa.1934.0106, doi:10.1098/rspa.1934.0106, arXiv:https://royalsocietypublishing.org/doi/pdf/10.1098/rspa.1934.0106.
Trilinos Project Team, T., . The Trilinos Project Website.
Vishwakarma, J., Chattopadhyay, K., Santhi Srinivas, N., 2020. Effect of build orientation on microstructure and tensile behaviour of selectively laser melted m300 maraging steel. Materials Science and Engineering: A 798, 140130. URL: https://www.sciencedirect.com/science/article/pii/S0921509320311977, doi:https://doi.org/10.1016/j.msea.2020.140130.
Wassermann, G., 1935. Ueber den Mechanismus der [alpha]-[gamma]-Umwandlung des Eisens. Verlag Stahleisen.
Wei, S., Kumar, P., Lau, K.B., Wuu, D., Liew, L.L., Wei, F., Teo, S.L., Cheong, A., Ng, C.K., Zhang, B., Tan, C.C., Wang, P., Ramamurty, U., 2022. Effect of heat treatment on the microstructure and mechanical properties of 2.4 gpa grade maraging steel fabricated by laser powder bed fusion. Additive Manufacturing 59, 103190. URL: https://www.sciencedirect.com/science/article/pii/S2214860422005796, doi:https://doi.org/10.1016/j.addma.2022.103190.
Werner, M., 1987. Temperature and strain-rate dependence of the flow stress of ultrapure tantalum single crystals. physica status solidi (a) 104, 63–78. URL: https://onlinelibrary.wiley.com/doi/abs/10.1002/pssa.2211040105, doi:https://doi.org/10.1002/pssa.2211040105, arXiv:https://onlinelibrary.wiley.com/doi/pdf/10.1002/pssa.2211040105.
Xi, N., Ni, Z., Fang, X., Zhou, Y., Tang, K., Zhang, H., Huang, K., 2023. Role of δ-phase on mechanical behaviors of additive manufactured inconel 718: Detailed microstructure analysis and crystal plasticity modelling. International Journal of Plasticity 168, 103708. URL: https://www.sciencedirect.com/science/article/pii/S0749641923001924, doi:https://doi.org/10.1016/j.ijplas.2023.103708.
Yalcinkaya, T., Brekelmans, W.A.M., Geers, M.G.D., 2008. BCC single crystal plasticity modeling and its experimental identification. Modelling and Simulation in Materials Science and Engineering 16, 085007. URL: https://doi.org/10.1088/0965-0393/16/8/085007, doi:10.1088/0965-0393/16/8/085007.
Zecevic, M., Upadhyay, M.V., Polatidis, E., Panzner, T., Van Swygenhoven, H., Knezevic, M., 2019. A crystallographic extension to the olson-cohen model for predicting strain path dependence of martensitic transformation. Acta Materialia 166, 386–401. URL: https://www.sciencedirect.com/science/article/pii/S1359645419300047, doi:https://doi.org/10.1016/j.actamat.2018.12.060.
Zhao, Z., Wang, L., Kong, D., Liu, P., He, X., Ni, X., Zhang, L., Dong, C., 2022. Texture dependence on the mechanical properties of 18ni300 maraging steel fabricated by laser powder bed fusion. Materials Characterization 189, 111938. URL: https://www.sciencedirect.com/science/article/pii/S1044580322002200, doi:https://doi.org/10.1016/

j.matchar.2022.111938.
Zienkiewicz, O., Taylor, R., Fox, D., 2014. Chapter 3 - solution of nonlinear algebraic equations, in: Zienkiewicz, O., Taylor, R., Fox, D. (Eds.), The Finite Element Method for Solid and Structural Mechanics (Seventh Edition). seventh edition ed.. Butterworth-Heinemann, Oxford, pp. 57–74. URL: https://www.sciencedirect.com/science/article/pii/B978185617634700003X, doi:https://doi.org/10.1016/B978-1-85617-634-7.00003-X.

Appendix A. Kurdjumov-Sachs orientation relationship for tetragonality ratio $r = 1$.

During the austenite-martensite phase transformation, volume change and shearing mechanism are involved in the formation of martensitic phase. This gives rise to multiple martensitic variants with a specific orientation relationship with respect to the prior austenite grain, typically adhering to the Kurdjumov-Sachs orientation relationship. This can be mathematically writen by the notion of the planes and directions that are parallel

$$\mathcal{P}_i(111)_\gamma \| \mathcal{P}_i(011)_\alpha, \quad \mathcal{P}_i[10\bar{1}]_\gamma \| \mathcal{P}_i[11\bar{1}]_\alpha, \tag{A.1}$$

where $\mathcal{P}$ is the group of rotations ($i = 1...24$) specified in Appendix B.
The rotation matrices for the lattice transformation can be easily derived following the methodology proposed by (Koumatos and Muehlemann, 2017). Specifically, we define the following matrices:

$$\boldsymbol{R}_{45} = \begin{bmatrix} \sqrt{2}/2 & -\sqrt{2}/2 & 0 \\ \sqrt{2}/2 & \sqrt{2}/2 & 0 \\ 0 & 0 & 1 \end{bmatrix}, \tag{A.2}$$

$$\boldsymbol{R}_\alpha = \begin{bmatrix} u_\alpha^2 + (1-u_\alpha^2)\cos(\theta_\alpha) & u_\alpha v_\alpha(1-\cos(\theta_\alpha)) - w_\alpha \sin(theta_\alpha) & u_\alpha w_\alpha(1-\cos(\theta_\alpha)) + v_\alpha \sin(\theta_\alpha) \\ u_\alpha v_\alpha(1-\cos(\theta_\alpha)) + w_\alpha \sin(\theta_\alpha) & v_\alpha^2 + (1-v_\alpha^2)\cos(\theta_\alpha) & v_\alpha w_\alpha(1-\cos(\theta_\alpha)) - u_\alpha \sin(\theta_\alpha) \\ u_\alpha w_\alpha(1-\cos(\theta_\alpha)) - v_\alpha \sin(\theta_\alpha) & v_\alpha w_\alpha(1-\cos(\theta_\alpha)) + u_\alpha \sin(\theta_\alpha) & w_\alpha^2 + (1-w_\alpha^2)\cos(\theta_\alpha) \end{bmatrix}, \tag{A.3}$$

where

$$\begin{aligned} \theta_I &= -\text{acos}((\sqrt{(}3)\sqrt{(}r^2+1)+1)/(2\sqrt{(}r^2+2))) \\ \theta_{II} &= -\text{acos}((1+\sqrt{(}2)r)/(\sqrt{(}3)\sqrt{(}1+r^2))) \end{aligned}, \tag{A.4}$$

where for the specific case of the tetragonality ratio $r = 1$, the values become $\theta_I = -5.2644°$, $\theta_{II} = -9.7356°$. The rotation axis vectors are chosen as $\vec{u}_I = (u_I, v_I, w_I) = (1, 1, 1)$, and $\vec{u}_{II} = (-1, 1, 0)$ (Koumatos and Muehlemann, 2017). With these parameters the orientation relationship matrix of the first variant that satisfies the Kurdjumov-Sachs orientation relationship becomes:

$$\boldsymbol{O}_{\text{KS}_1} = \boldsymbol{R}_{45}\boldsymbol{R}_I\boldsymbol{R}_{II}, \tag{A.5}$$

which can be evaluated numerically

$$\boldsymbol{O}_{\text{KS}_1} = \begin{bmatrix} 0.741582 & -0.666667 & -0.074915 \\ 0.649830 & 0.741582 & -0.166667 \\ 0.166667 & 0.074915 & 0.983163 \end{bmatrix}. \tag{A.6}$$

This matrix is equivalent to the Euler angle representation with $\phi_1 = 335.8°$, $\Phi = 10.53°$, and $\phi_2 = 65.8°$. The orientation relationship matrix of the remaining variants can be calculated by applying the $\mathcal{P}$ group of rotations

$$\boldsymbol{O}_{\text{KS}_i} = \mathcal{P}_i\boldsymbol{O}_{\text{KS}_1}\mathcal{P}_i. \tag{A.7}$$

These rotations are then applied to each block within the local coordinate system of the prior austenite grain.

Appendix B. The group $\mathcal{P}_{24}$

The 24 elements of the group $\mathcal{P}_{24}$ that are necessary for calculating the rotation matrices in Appendix A and disorientation in Appendix E are listed below. These matrices represent rotations that map cube on itself.

$$
\begin{aligned}
\mathcal{P}_1 &= \begin{bmatrix} 1 & 0 & 0 \\ 0 & 1 & 0 \\ 0 & 0 & 1 \end{bmatrix}, \quad \mathcal{P}_2 = \begin{bmatrix} 0 & 0 & -1 \\ 0 & -1 & 0 \\ -1 & 0 & 0 \end{bmatrix}, \quad \mathcal{P}_3 = \begin{bmatrix} 0 & 0 & 1 \\ 1 & 0 & 0 \\ 0 & 1 & 0 \end{bmatrix}, \quad \mathcal{P}_4 = \begin{bmatrix} -1 & 0 & 0 \\ 0 & 0 & -1 \\ 0 & -1 & 0 \end{bmatrix}, \\
\mathcal{P}_5 &= \begin{bmatrix} 0 & 1 & 0 \\ 0 & 0 & 1 \\ 1 & 0 & 0 \end{bmatrix}, \quad \mathcal{P}_6 = \begin{bmatrix} 0 & -1 & 0 \\ -1 & 0 & 0 \\ 0 & 0 & -1 \end{bmatrix}, \quad \mathcal{P}_7 = \begin{bmatrix} 0 & 0 & -1 \\ 0 & 1 & 0 \\ 1 & 0 & 0 \end{bmatrix}, \quad \mathcal{P}_8 = \begin{bmatrix} 1 & 0 & 0 \\ 0 & -1 & 0 \\ 0 & 0 & -1 \end{bmatrix}, \\
\mathcal{P}_9 &= \begin{bmatrix} -1 & 0 & 0 \\ 0 & 0 & 1 \\ 0 & 1 & 0 \end{bmatrix}, \quad \mathcal{P}_{10} = \begin{bmatrix} 0 & 0 & 1 \\ -1 & 0 & 0 \\ 0 & -1 & 0 \end{bmatrix}, \quad \mathcal{P}_{11} = \begin{bmatrix} 0 & -1 & 0 \\ 1 & 0 & 0 \\ 0 & 0 & 1 \end{bmatrix}, \quad \mathcal{P}_{12} = \begin{bmatrix} 0 & 1 & 0 \\ 0 & 0 & -1 \\ -1 & 0 & 0 \end{bmatrix}, \\
\mathcal{P}_{13} &= \begin{bmatrix} 0 & 0 & 1 \\ 0 & -1 & 0 \\ 1 & 0 & 0 \end{bmatrix}, \quad \mathcal{P}_{14} = \begin{bmatrix} -1 & 0 & 0 \\ 0 & 1 & 0 \\ 0 & 0 & -1 \end{bmatrix}, \quad \mathcal{P}_{15} = \begin{bmatrix} 1 & 0 & 0 \\ 0 & 0 & -1 \\ 0 & 1 & 0 \end{bmatrix}, \quad \mathcal{P}_{16} = \begin{bmatrix} 0 & 0 & -1 \\ 1 & 0 & 0 \\ 0 & -1 & 0 \end{bmatrix}, \\
\mathcal{P}_{17} &= \begin{bmatrix} 0 & 1 & 0 \\ -1 & 0 & 0 \\ 0 & 0 & 1 \end{bmatrix}, \quad \mathcal{P}_{18} = \begin{bmatrix} 0 & -1 & 0 \\ 0 & 0 & 1 \\ -1 & 0 & 0 \end{bmatrix}, \quad \mathcal{P}_{19} = \begin{bmatrix} 0 & 0 & 1 \\ 0 & 1 & 0 \\ -1 & 0 & 0 \end{bmatrix}, \quad \mathcal{P}_{20} = \begin{bmatrix} -1 & 0 & 0 \\ 0 & -1 & 0 \\ 0 & 0 & 1 \end{bmatrix}, \\
\mathcal{P}_{21} &= \begin{bmatrix} 1 & 0 & 0 \\ 0 & 0 & 1 \\ 0 & -1 & 0 \end{bmatrix}, \quad \mathcal{P}_{22} = \begin{bmatrix} 0 & 0 & -1 \\ -1 & 0 & 0 \\ 0 & 1 & 0 \end{bmatrix}, \quad \mathcal{P}_{23} = \begin{bmatrix} 0 & 1 & 0 \\ 1 & 0 & 0 \\ 0 & 0 & -1 \end{bmatrix}, \quad \mathcal{P}_{24} = \begin{bmatrix} 0 & -1 & 0 \\ 0 & 0 & -1 \\ 1 & 0 & 0 \end{bmatrix},
\end{aligned}
\tag{B.1}
$$

Appendix C. Notes on rotation matrices

In this work, we have employed rotations through Eule angles ϕ, θ, ψ. Any rotation matrix for a general rotation can be decomposed into three matrices

$$\boldsymbol{R} = \boldsymbol{Q}_1 \boldsymbol{Q}_2 \boldsymbol{Q}_3, \tag{C.1}$$

where

$$\boldsymbol{Q}_1 = \begin{bmatrix} \cos\phi & \sin\phi & 0 \\ -\sin\phi & \cos\phi & 0 \\ 0 & 0 & 1 \end{bmatrix}, \boldsymbol{Q}_2 = \begin{bmatrix} 1 & 0 & 0 \\ 0 & \cos\theta & \sin\theta \\ 0 & -\sin\theta & \cos\theta \end{bmatrix}, \boldsymbol{Q}_3 = \begin{bmatrix} \cos\psi & \sin\psi & 0 \\ -\sin\psi & \cos\psi & 0 \\ 0 & 0 & 1 \end{bmatrix}. \tag{C.2}$$

Any second order tensor can then be rotated following $\boldsymbol{\sigma}' = \boldsymbol{R}\boldsymbol{\sigma}\boldsymbol{R}^T$. In order to rotate a forth order tensor, such as the tensor of elastic constants $\mathbb{C}$, we introduce the following matrix

$$\mathbf{T} = \begin{bmatrix} \mathbf{T}^{(1)} & 2\mathbf{T}^{(2)} \\ \mathbf{T}^{(3)} & \mathbf{T}^{(4)} \end{bmatrix}, \tag{C.3}$$

where

$$\begin{aligned} T_{ij}^{(1)} &= R_{ij}^2 \\ T_{ij}^{(2)} &= R_{i\mathrm{mod}(j+1,3)} R_{i\mathrm{mod}(j+2,3)} \\ T_{ij}^{(3)} &= R_{\mathrm{mod}(i+1,3)j} R_{\mathrm{mod}(i+2,3)j} \\ T_{ij}^{(4)} &= R_{\mathrm{mod}(i+1,3)\mathrm{mod}(j+1,3)} R_{\mathrm{mod}(i+2,3)\mathrm{mod}(j+2,3)} + R_{\mathrm{mod}(i+1,3)\mathrm{mod}(j+2,3)} R_{\mathrm{mod}(i+2,3)\mathrm{mod}(j+1,3)} \end{aligned}, \tag{C.4}$$

where the modulo function is defined as

$$\mathrm{mod(i,3)} = \begin{cases} i & i \leq 3 \\ i-3 & i > 3 \end{cases}. \tag{C.5}$$

The tensor of elastic constants can then be rotated by

$$\mathbf{C}' = \mathbf{T}\mathbf{C}\mathbf{A}\mathbf{T}^{-1}\mathbf{A}^{-1}, \tag{C.6}$$

where the Reuter's matrix

$$\mathbf{A} = \begin{bmatrix} 1 & 0 & 0 & 0 & 0 & 0 \\ 0 & 1 & 0 & 0 & 0 & 0 \\ 0 & 0 & 1 & 0 & 0 & 0 \\ 0 & 0 & 0 & 2 & 0 & 0 \\ 0 & 0 & 0 & 0 & 2 & 0 \\ 0 & 0 & 0 & 0 & 0 & 2 \end{bmatrix}, \tag{C.7}$$

is introduced due to the Voigt convention of strain where the engineering strain components are used instead of tensorial components.

Appendix D. Notes on analytical solutions of flow stress

In this section, an analytical solution for the flow stress is derived for the case without hardening. This solution can be used for benchmarking the written code in predicting the yield stress of a single crystal for different crystal orientations. The maximum value of the flow stress can be derived as a function of the strength components, temperature and strain rate:

$$\sigma_y = \chi \left(s_t \left[1 - \left(-\frac{kT}{G_0} \ln \left(\frac{\kappa}{2} \frac{\dot{\varepsilon}}{\dot{\gamma}_0} \right) \right)^{\frac{1}{q}} \right]^{\frac{1}{p}} + s_a \right), \tag{D.1}$$

where for [001]: $\chi = \sqrt{6}$, $\kappa = \frac{\sqrt{6}}{4}$, for [011]: $\chi = \sqrt{6}$, $\kappa = \frac{\sqrt{6}}{2}$ and for [111] loading direction $\chi = \sqrt{\frac{27}{2}}$, $\kappa = \frac{\sqrt{6}}{2}$. These are the corners of the stereographic triangle where for [001] exactly eight slip systems are active, for [011] four slip systems, and for [111] six slip systems. Below is a more detailed derivation for the [001] case, whereas the remaining points can be derived analogically:
Neglecting non-Schmid effects, the resolved shear stress is calculated

$$\tau^\alpha = \sigma \vec{v} \otimes \vec{v} : \vec{m}^\alpha \otimes \vec{n}^\alpha. \tag{D.2}$$

For the case of loading direction $\vec{v} = \big[001\big]$, it can be shown that the only non-zero product is for the slip systems 2, 3, 4, 6, 7, 8, 11, 12 (as listed in the first half of Table F.5). For each of these slip systems, $|\tau| = \frac{1}{\sqrt{6}}\sigma$. Plastic velocity gradient can be also calculated

$$\boldsymbol{L}^p = \boldsymbol{D}^p = \sum_\alpha \dot{\gamma}^\alpha \vec{m}^\alpha \otimes \vec{n}^\alpha = \dot{\gamma} \frac{8}{\sqrt{6}} \boldsymbol{I}. \tag{D.3}$$

Considering the flow stress value when $\dot{\sigma} = 0$ gives $\boldsymbol{D} - \boldsymbol{D}^p = 0$. Considering one loading direction with strain rate $\dot{\varepsilon}$ we can write

$$\dot{\varepsilon} = \frac{8}{\sqrt{6}} \dot{\gamma}. \tag{D.4}$$

Combining the equations of slip kinetics yields

$$\dot{\varepsilon} = \frac{8}{\sqrt{6}} \dot{\gamma}_0 \exp\left(\frac{\Delta G}{kT} \right), \quad \Delta G = G_0 \left[1 - \left(\frac{\frac{4}{\sqrt{6}}\sigma - s_a}{s_t} \right)^p \right]^q. \tag{D.5}$$

Now, the relationship between stress σ and strain rate $\dot{\varepsilon}$ can be derived, as presented in Eq.D.1.
Furthermore, it is realized that the following condition should be satisfied for obtaining a physical result

$$T < -\frac{G_0}{k \ln\left(\frac{\chi}{2} \frac{\dot{\varepsilon}}{\dot{\gamma}_0} \right)}. \tag{D.6}$$

Violation of this condition will lead to a situation in which the increment of slip is higher than the applied load increment.

Appendix E. Recursive algorithm for grain cluster identification

In this section, we describe the recursive algorithm for identifying the individual crystal clusters within the given misorientation limit $\Delta\theta_c$. These cluster are considered for the Hall-Petch effect where only the interfaces with the misorientation $\Delta\theta > \Delta\theta_c$ are considered to cause the pile-up of dislocations. The first step therefore requires calculation of the misorientation $\Delta\theta$.
The misorientation between two neighbouring crystals can be simply identified as a rotation that transforms one crystal into another. To illustrate, let us begin with the rotation matrices of two neighbouring crystals

$$\begin{aligned} \boldsymbol{R}_1(i) &= \begin{bmatrix} \mathcal{P}_i\vec{m}_1 & \mathcal{P}_i\vec{n}_1 & \mathcal{P}_i\vec{m}_1 \times \mathcal{P}_i\vec{n}_1 \end{bmatrix} \\ \boldsymbol{R}_2(i) &= \begin{bmatrix} \mathcal{P}_i\vec{m}_2 & \mathcal{P}_i\vec{n}_2 & \mathcal{P}_i\vec{m}_2 \times \mathcal{P}_i\vec{n}_2 \end{bmatrix}. \end{aligned} \tag{E.1}$$

In a crystal plasticity framework, these matrices can be established through the slip normal $\vec{n}$ and slip direction $\vec{m}$ vectors (only one pair is needed). In this case, the clusters can be re-calculated at each iteration taking into consideration grain rotation due to plastic deformation. The 24 matrices ($i = 1 \dots 24$) are then calculated considering the group $\mathcal{P}^{24}$ of rotations that map a cube on itself (Mackenzie and Thomson, 1957), (Mackenzie, 1958). These matrices are listed in Appendix B. Only 24 matrices are required (instead of 48) for calculating the misorientation $\Delta\theta$ as the crystal symmetry applies to both sides of grain boundary.

Algorithm 1: Recursive algorithm for cluster identification.

```
/* Loop through all cells of the cuboidal RVE                          */
id = 1 ;                                              /* Cluster index */
for i = 1 to nx do
    for j = 1 to ny do
        for k = 1 to nz do
            AssignIdx(id, i, j, k)
            id++

/* Function to assign cluster index                                    */
Function AssignIdx(id, i, j, k):
    if touched[(i,j,k)] then
        return
    clusterId[(i, j, k)] = id
    touched[(i, j, k)] = true
    /* Loop through the six possible directions of neighbouring cells  */
    ip = [1, −1, 0, 0, 0, 0]
    jp = [0, 0, 1, −1, 0, 0]
    kp = [0, 0, 0, 0, 1, −1]
    for p = 1 to 6 do
        if Δθ(i, j, k, p) < Δθ_c then
            /* Call the function itself                                */
            AssignIdx(id, i+ip(p), j+jp(p), k+kp(p), nx, ny, nz)
```

Output: $clusterId[(i, j, k)]$

The misorientation matrix for all possible states is then defined as

$$\boldsymbol{\Delta g}_{ij} = \boldsymbol{R}_2(j)^{-1}\boldsymbol{R}_1(i), \tag{E.2}$$

and the misorientation angle is calculated according to

$$\Delta\theta_{ij} = \cos^{-1}\left(\frac{\text{trace}\boldsymbol{\Delta g}_{ij} - 1}{2}\right). \tag{E.3}$$

Considering the symmetry operations, the smallest value value from the misorientations is chosen $\Delta\theta = \min\theta_{ij}$, also referred to as the disorientation. The misorientation in cubic crystals can go up to 180°, however the maximum value of disorientation is about $\approx 62.8°$ (Mackenzie, 1958).

Having calculated the smallest misorientation (disorientation), a recursive algorithm is constructed to identify individual clusters bounded by $\Delta\theta_c$. The pseudo-code of the algorithm is presented in Alg.1.

Each cell in the cuboidal RVE is assigned the calculated disorientation value $\Delta\theta$ in six different directions between the cell and its neighbours. The algorithm moves from cell to cell keeping the cluster id as long as the disorientation value in any direction is less than the critical value ($\Delta\theta < \Delta\theta_c$). If no neighbouring cell can be found to satisfy this condition, the cluster index is incremented by 1 and the algorithm continues on another unprocessed cell.

Given the algorithm is recursive and operates on a large grid size of 128^3 cells, the program may quickly run out of the stack space. In that case it is useful to increase the stack size by setting `ulimit -s unlimited`.

Appendix F. Directions associated with slip systems

Slip system direction and slip plane normal considered in the bcc model are presented in Table F.5.

Table F.5: The 24 slip systems of the bcc lattice.

α	not.	Slip system	α	not.	Slip system	α	Slip system	α	Slip system
1	B5	$(1\bar{1}0)[111]$	7	D4	$(\bar{1}01)[1\bar{1}1]$	13	$(1\bar{1}0)[\bar{1}\bar{1}\bar{1}]$	19	$(\bar{1}01)[\bar{1}1\bar{1}]$
2	B4	$(\bar{1}01)[111]$	8	D1	$(0\bar{1}\bar{1})[1\bar{1}1]$	14	$(\bar{1}01)[\bar{1}\bar{1}\bar{1}]$	20	$(0\bar{1}\bar{1})[\bar{1}1\bar{1}]$
3	B2	$(01\bar{1})[111]$	9	D6	$(110)[1\bar{1}1]$	15	$(01\bar{1})[\bar{1}\bar{1}\bar{1}]$	21	$(110)[\bar{1}1\bar{1}]$
4	A3	$(101)[\bar{1}11]$	10	C5	$(\bar{1}10)[\bar{1}\bar{1}1]$	16	$(101)[1\bar{1}\bar{1}]$	22	$(\bar{1}10)[11\bar{1}]$
5	A6	$(\bar{1}\bar{1}0)[\bar{1}11]$	11	C3	$(101)[\bar{1}\bar{1}1]$	17	$(\bar{1}\bar{1}0)[1\bar{1}\bar{1}]$	23	$(101)[11\bar{1}]$
6	A2	$(01\bar{1})[\bar{1}11]$	12	C1	$(0\bar{1}\bar{1})[\bar{1}\bar{1}1]$	18	$(01\bar{1})[1\bar{1}\bar{1}]$	24	$(0\bar{1}\bar{1})[11\bar{1}]$

Slip system direction and slip plane normal considered in the fcc model are presented in Table F.6.

Table F.6: The 12 slip system of the fcc lattice.

α	not.	$\vec{m}$	$\vec{n}$	α	not.	$\vec{m}$	$\vec{n}$
1	B5	$[1\bar{1}0]$	(111)	7	D4	$[\bar{1}01]$	$(1\bar{1}1)$
2	B4	$[\bar{1}01]$	(111)	8	D1	$[0\bar{1}\bar{1}]$	$(1\bar{1}1)$
3	B2	$[01\bar{1}]$	(111)	9	D6	[110]	$(1\bar{1}1)$
4	A3	[101]	$(\bar{1}11)$	10	C5	$[\bar{1}10]$	$(\bar{1}\bar{1}1)$
5	A6	$[\bar{1}\bar{1}0]$	$(\bar{1}11)$	11	C3	[101]	$(\bar{1}\bar{1}1)$
6	A2	$[01\bar{1}]$	$(\bar{1}11)$	12	C1	$[0\bar{1}\bar{1}]$	$(\bar{1}\bar{1}1)$

Appendix G. Fitting of non-Schmid coefficients

Given the atomistic simulation result data of critical resolved shear stress (CRSS) published by (Chen et al., 2013), the following functions y can be constructed for the purpose of calculating the weights of stress components $\vec{\eta}$ in Eq.23 which incorporates non-Schmid effects

$$y = f(\vec{\eta}, \tau_c, \chi, \Sigma), \tag{G.1}$$

where y is proportional to critical resolved shear stress, more specifically CRSS$/C_{44}$, $\vec{\eta} = (\eta_1, \eta_2, \eta_3)$ represents the coefficients in the effective resolved shear stress equation (see Eq.23), and τ_c is the critical value of the resolved shear stress. The values of χ represent the orientation of the maximum resolved shear stress plane with respect to the reference $(\bar{1}01)$ plane, and Σ represents the stress perpendicular to slip direction. In total, 37 data points from multiple figures by (Chen et al., 2013) representing the effects of various loading conditions of a single dislocation are collated and plotted in Fig.G.21 using the blue circles. The horizontal axis indicates the data point id consisting of a pair $[\chi, \Sigma]$, while the vertical axis represents the unitless ratio between the critical resolved shear stress and C_{44} elastic constant.

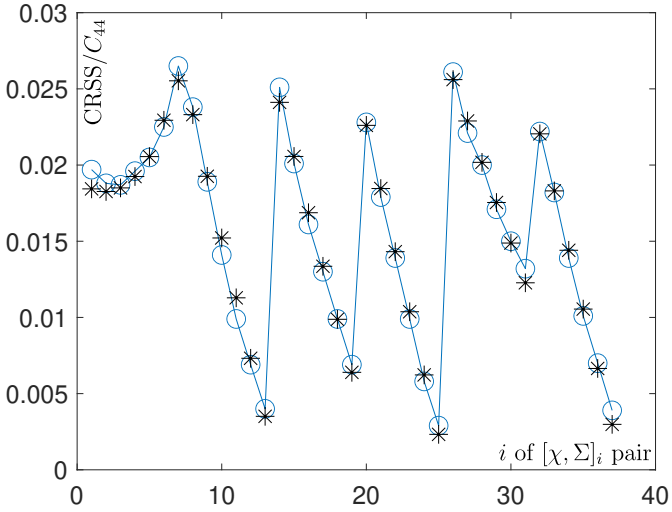


Figure G.21: Atomistic simulation data from (Chen et al., 2013) denoted by blue circles connected with lines and the least square fit of the Eq.23 effective yield criterion denoted by the asterix symbols.

The first seven points are representative of CRSS as a function of orientation of maximum resolved shear stress plane. The remaining data points illustrate the dependence of CRSS on the shear stress perpendicular to the slip direction for different orientation of the maximum resolved shear stress χ.
The coefficients $\vec{\eta}$ and τ_c of the effective yield criterion (Eq.23) can be found through the least-square method

$$\boldsymbol{J}^T \boldsymbol{J} \Delta\boldsymbol{\eta} = \boldsymbol{J}^T \Delta\boldsymbol{y}, \tag{G.2}$$

where $\Delta y_i = \text{CRSS}_i/C_{44} - f(\vec{\eta}_k, \tau_{c_k}, [\chi, \Sigma]_i)$, where $i = 1 \ldots 37$ data points, and $k = 0$ is the initial estimate. The Jacobian $\boldsymbol{J}$ is calculated from the derivatives of f with respect to $\vec{\eta}_k$. The solution is found iteratively $\vec{\eta}_{k+1} = \vec{\eta}_k + \Delta\vec{\eta}$ until the required tolerance is reached. The fitted results are presented in Fig.23 using the asterix symbols. The best fit values of the coefficients are found to be $\eta_1 = 0.4675$, $\eta_2 = 0.1034$, $\eta_3 = 0.5652$, and $\tau_c/C_{44} = 0.0237$.

Appendix H. Numerical implementation

In this section, we elaborate on a numerical scheme aimed at solving the governing equations outlined in Sec.5 and Sec.6. The scheme entails a description of the numerical discretization, encompassing the finite element implementation within the updated Lagrangian framework and the integration of material models. The finite element crystal plasticity model, developed in-house using C++, is constructed leveraging several existing open-source libraries, namely VTK (Schroeder et al., 2006), Trilinos (Trilinos Project Team) (utilized as an iterative solver for linear systems of equations), and Eigen3 (Guennebaud et al., 2010).

Appendix H.1. Finite element formulation within the updated-Lagrangian framework

The simulation domain denoted by Ω is subdivided into a finite number of elements, $\Omega = \cup_e \Omega^e$. First, we present the derivation within a single finite element domain Ω^e, which is subsequently integrated into the global system via the mesh topology matrix $\mathcal{A}$. Each domain Ω^e is in the general case depicted in its physical coordinates as a hexahedral shape, with its nodal points labelled as x_i^p, y_i^p, z_i^p. Employing bilinear shape functions and the iso-parametric formulation of the finite element, the shape functions expressed in their natural coordinates are written as follows

$$N_i = \frac{1}{8}\left(1 + a_i\xi_1\right)\left(1 + b_i\xi_2\right)\left(1 + c_i\xi_3\right), \tag{H.1}$$

where $\boldsymbol{a} = [-1,-1,-1,-1,1,1,1,1]$, $\boldsymbol{b} = [1,-1,-1,1,1,-1,-1,1]$, and $\boldsymbol{c} = [1,1,-1,-,1,1,1,-1,-1]$, while ξ_1, ξ_2, and ξ_3 represent the isoparametric coordinates.
The gradients of these shape functions with respect to the physical coordinates are expressed by

$$\boldsymbol{\nabla} N_i = \boldsymbol{J}_i^{-1} \boldsymbol{\nabla}_\xi N_i, \tag{H.2}$$

where $\boldsymbol{J} = \frac{\partial \boldsymbol{\xi}}{\partial \boldsymbol{x}}$ denotes the Jacobian matrix, representing the transformation between the physical and natural coordinates, and can be explicitly written as

$$\boldsymbol{J} = \begin{bmatrix} \sum_i \frac{\partial N_i}{\partial \xi_1} x_i^p & \sum_i \frac{\partial N_i}{\partial \xi_1} y_i^p & \sum_i \frac{\partial N_i}{\partial \xi_1} z_i^p \\ \sum_i \frac{\partial N_i}{\partial \xi_2} x_i^p & \sum_i \frac{\partial N_i}{\partial \xi_2} y_i^p & \sum_i \frac{\partial N_2}{\partial \xi_1} z_i^p \\ \sum_i \frac{\partial N_i}{\partial \xi_3} x_i^p & \sum_i \frac{\partial N_i}{\partial \xi_3} y_i^p & \sum_i \frac{\partial N_i}{\partial \xi_3} z_i^p \end{bmatrix}. \tag{H.3}$$

We collate the shape functions of all nodes into a matrix in the following format

$$\boldsymbol{N} = \begin{bmatrix} N_1 & 0 & 0 & N_2 & 0 & 0 & ... & N_8 & 0 & 0 \\ 0 & N_1 & 0 & 0 & N_2 & 0 & ... & 0 & N_8 & 0 \\ 0 & 0 & N_1 & 0 & 0 & N_2 & ... & 0 & 0 & N_8 \end{bmatrix}, \tag{H.4}$$

along with the strain matrix defined by $\boldsymbol{B} = \boldsymbol{L}\boldsymbol{N}$, where the differential operator $\boldsymbol{L}$ is represented by

$$\boldsymbol{L} = \begin{bmatrix} \frac{\partial}{\partial x} & 0 & 0 \\ 0 & \frac{\partial}{\partial y} & 0 \\ 0 & 0 & \frac{\partial}{\partial z} \\ 0 & \frac{\partial}{\partial y} & \frac{\partial}{\partial z} \\ \frac{\partial}{\partial x} & 0 & \frac{\partial}{\partial z} \\ \frac{\partial}{\partial x} & \frac{\partial}{\partial y} & 0 \end{bmatrix}. \tag{H.5}$$

The displacement field approximation can now be presented as a linear combination of the product of nodal values $\boldsymbol{\delta}$ and shape functions $\boldsymbol{N}$

$$\boldsymbol{u} \approx \sum N_i(\boldsymbol{x})\delta_i(t) = \boldsymbol{N}\boldsymbol{\delta}. \tag{H.6}$$

Here, $\boldsymbol{\delta} = \begin{bmatrix} u_1 & v_1 & w_1 & u_2 & v_2 & w_2 & ... & u_8 & v_8 & w_8 \end{bmatrix}^T$ contains the displacement vectors (u_i, v_i, w_i) in all nodes of the hexahedral finite element, $i = 1...8$.

This approximation is utilized in solving the linear momentum conservation equation to achieve mechanical equilibrium. Neglecting inertial forces and assuming that loads are applied slowly, the governing equation simplifies into

$$\boldsymbol{\nabla} \cdot \boldsymbol{\sigma} + \rho \boldsymbol{b} = \boldsymbol{0}. \tag{H.7}$$

Here, $\boldsymbol{\sigma}$ represents the Cauchy stress and $\boldsymbol{b}$ denotes the volume body forces. In the updated-Lagrangian formulation, Eulerian-like variables are utilized, however, they are expressed in terms of material coordinates. Regarding boundary conditions, it is assumed that $\boldsymbol{\sigma}(\boldsymbol{X}, t)\boldsymbol{n} = \boldsymbol{t}$ on Γ_t, $\boldsymbol{u}(\boldsymbol{X}, t) = \bar{\boldsymbol{u}}(\boldsymbol{X}, t)$ on Γ_u and $\Omega = \Omega_0$ in $t = 0$.

The finite element approximation of the linear momentum equation can be derived beginning with a test function $\tilde{\boldsymbol{\zeta}}(\boldsymbol{x})$ approximated as $\tilde{\boldsymbol{\zeta}} \approx \boldsymbol{N}\boldsymbol{\zeta}$, taking the dot product with the linear momentum conservation equation and integrating it over the domain of a finite element Ω^e. This process is outlined in the following steps

$$\int_{\Omega^e} \boldsymbol{N}\boldsymbol{\zeta} \cdot \boldsymbol{\nabla} \cdot \boldsymbol{\sigma} d\Omega^e + \int_{\Omega^e} \boldsymbol{N}\boldsymbol{\zeta} \cdot \rho \boldsymbol{b} d\Omega^e = 0, \tag{H.8}$$

$$\int_{\Omega^e} \boldsymbol{\nabla} \left(\boldsymbol{N}\boldsymbol{\zeta} \cdot \boldsymbol{\sigma} \right) d\Omega^e - \int_{\Omega^e} \boldsymbol{\nabla} \left(\boldsymbol{N}\boldsymbol{\zeta} \right) \cdot \boldsymbol{\sigma} + \int_{\Omega^e} \boldsymbol{N}\boldsymbol{\zeta} \cdot \rho \boldsymbol{b} d\Omega^e = 0. \tag{H.9}$$

By applying the Gauss's theorem, it can be shown that for an arbitrary test function, the equations can be rearranged to derive

$$\int_{\Gamma} \boldsymbol{N}\boldsymbol{\zeta} \cdot \boldsymbol{t} d\Gamma - \int_{\Omega^e} \boldsymbol{\nabla} \left(\boldsymbol{N}\boldsymbol{\zeta} \right) \cdot \boldsymbol{\sigma} d\Omega^e + \int_{\Omega^e} \boldsymbol{N}\boldsymbol{\zeta} \cdot \rho \boldsymbol{b} d\Omega^e = 0, \tag{H.10}$$

$$\int_{\Omega^e} \boldsymbol{\nabla} \boldsymbol{N} \cdot \boldsymbol{\sigma} d\Omega^e = \int_{\Omega^e} \boldsymbol{N} \cdot \rho \boldsymbol{b} d\Omega^e + \int_{\Gamma} \boldsymbol{N} \cdot \boldsymbol{t} d\Gamma, \tag{H.11}$$

which can be using the earlier notation conveniently rewritten into the Voigt form

$$\int_{\Omega^e} \boldsymbol{B}\{\boldsymbol{\sigma}\} d\Omega^e = \int_{\Omega^e} \boldsymbol{N} \cdot \rho \boldsymbol{b} d\Omega^e + \int_{\Gamma} \boldsymbol{N} \cdot \boldsymbol{t} d\Gamma, \tag{H.12}$$

from which the internal and external forces can be easily identified acting on a single finite element

$$\begin{aligned} \boldsymbol{f}^{int} &= \int_{\Omega^e} \boldsymbol{B}^T \{\boldsymbol{\sigma}\} d\Omega^e \\ \boldsymbol{f}^{ext} &= \int_{\Omega^e} \boldsymbol{N} \cdot \boldsymbol{b} d\Omega^e + \int_{\partial\Omega} \boldsymbol{N} \cdot \boldsymbol{t} d\partial\Omega \end{aligned}. \tag{H.13}$$

This equation reveals the internal and external forces acting on a single finite element, leading to the condition $\boldsymbol{f}^{ext} = \boldsymbol{f}^{int}$ which indicates a system which has reached mechanical equilibrium. Any deviation from this equilibrium can be denoted by a residual $\boldsymbol{r} = \boldsymbol{f}^{ext} - \boldsymbol{f}^{int}$.

To satisfy the equilibrium condition, it is necessary to find the solution (in this case in terms of displacement field) which satisfies $\boldsymbol{r} = \boldsymbol{f}^{ext} - \boldsymbol{f}^{int} = \boldsymbol{0}$. This non-linear equation can be first expanded into a Taylor series, and considering the linear terms of this expansion, a Newton-Raphson method can be derived, converging to the solution through a sequence of its linearized steps

$$\boldsymbol{r}(\boldsymbol{\delta}) \approx \boldsymbol{r}(\boldsymbol{\delta}_0) + \boldsymbol{r}'(\boldsymbol{\delta}_0)\Delta\boldsymbol{\delta} = \boldsymbol{0}. \tag{H.14}$$

Noticing that $\{\boldsymbol{\sigma}\} = \{\boldsymbol{C}\}\boldsymbol{B}\boldsymbol{\delta}$, and $\boldsymbol{r}' = -\boldsymbol{f}^{int'}$, the equations can be written in the form below (explicitly stating they are derived for an element e)

$$\Delta\boldsymbol{\delta}^e \int_{\Omega^e} \boldsymbol{B}^T \{\boldsymbol{C}\} \boldsymbol{B} d\Omega^e = \boldsymbol{f}_e^{ext} - \boldsymbol{f}_e^{int}. \tag{H.15}$$

Due to the tediousness of explicitly integrating the integral, a simpler approximation using the Gauss quadrature formula is introduced, expressed in three-dimensional space as

$$\int_{-1}^{1}\int_{-1}^{1}\int_{-1}^{1} f(\boldsymbol{\xi})d\boldsymbol{\xi} \approx \sum_{i}\sum_{j}\sum_{k} w_i w_j w_k f(\boldsymbol{\xi}(i,j,k)) \det \boldsymbol{J}. \tag{H.16}$$

Applying this approximation to Eq.H.15 yields the following expression

$$\Delta\boldsymbol{\delta}^e \underbrace{\sum_{i}\sum_{j}\sum_{k} \boldsymbol{B}^T \{\boldsymbol{C}\}_{ijk} \boldsymbol{B} \det \boldsymbol{J} w_i w_j w_k}_{\text{element stiffness matrix } \boldsymbol{k}^e} = \boldsymbol{f}_e^{ext} - \boldsymbol{f}_e^{int}, \tag{H.17}$$

where the term on the left side can be identified as the element stiffness matrix $\boldsymbol{k}^e$.
Individual elements are assembled into the global system of equations through the mesh topology (connectivity) matrix $\mathcal{A}^e$, giving the global stiffness matrix $\boldsymbol{K}$ and the global force vector $\boldsymbol{F}$

$$\begin{aligned} \boldsymbol{K} &= \sum_e \mathcal{A}^e \boldsymbol{k}^e \\ \boldsymbol{F}^{\#} &= \sum_e \mathcal{A}^e \boldsymbol{f}_e^{\#} \end{aligned}. \tag{H.18}$$

The increment in nodal values of the displacement field $\Delta\boldsymbol{\delta}$ can be calculated by solving a linear system of equations $\boldsymbol{K}\Delta\boldsymbol{\delta} = \boldsymbol{F}^{ext} - \boldsymbol{F}^{int} = \boldsymbol{R}$.
By subdividing the total external load increment into a number of loadsteps, the finite element mesh coordinates are updated from the initial Ω_0 configuration through a sequence of steps Ω_k until the final configuration Ω, and thus the mesh deforms with the flow of material.

Appendix H.2. Integration of the constitutive model

To determine the internal forces $\boldsymbol{F}^{int}$, it is necessary to obtain the values of stress $\boldsymbol{\sigma}$ at each iteration, as described in Eq.H.13. The stress is derived from the constitutive models outlined in Sections 5 and 6. The discretization of these constitutive model equations employs a semi-implicit scheme, wherein a set of nonlinear equations is formulated to solve for the slip increment $\Delta\gamma^\alpha$. Below, a discretized set of equations is presented wherein the beginning of the time increment is denoted by t and the end of the time increment by τ, with $\Delta t = \tau - t$.
The objective of solving the material model is to predict the plastic deformation gradient $\boldsymbol{F}^p(\tau)$, stress $\boldsymbol{\sigma}(\tau)$, and internal variables $\alpha_i(\tau)$ (such as dislocation densities) at the end of the time increment τ, given the total deformation gradient $\boldsymbol{F}(t)$, $\boldsymbol{F}(\tau)$, plastic deformation gradient $\boldsymbol{F}^p(t)$, stress $\boldsymbol{\sigma}(t)$, and other internal variables $\alpha_i(t)$ at the beginning of the time increment t. The non-linear set of equations is solved using the Newton-Raphson method while this process is iteratively executed within the larger Newton-Raphson loop discussed in the previous section to ensure mechanical equilibrium. The resulting set of equations can be expressed as follows

$$\Delta\gamma^\alpha = f(\Delta\gamma^\alpha). \tag{H.19}$$

Expanding with the proposed constitutive model for bcc crystals we obtain a more explicit form of the non-linear equations

$$f^\alpha(\Delta\gamma(\tau)^\alpha) = \Delta\gamma(\tau)^\alpha - \dot{\gamma}_0 \Delta t \exp\left\{ -\frac{G_0 \left(1 - \left(\frac{\tau^\alpha(\Delta\gamma(\tau)) - s_a^\alpha(\Delta\gamma(\tau))}{s_t}\right)^p\right)^q}{kT} \right\} = 0. \tag{H.20}$$

Beginning with an initial estimate $\Delta\gamma^{\alpha} = \Delta\gamma^{\alpha}_{i=0}$, every Newton-Raphson iteration i can begin with the update of the plastic deformation gradient following

$$\boldsymbol{F}_i^P = \left(\boldsymbol{I} + \sum_{\alpha} \Delta\gamma_i^{\alpha}\right) \boldsymbol{F}^p(t), \tag{H.21}$$

followed by the elastic deformation gradient

$$\boldsymbol{F}_j^e = \boldsymbol{F}(\tau)\boldsymbol{F}_j^p, \tag{H.22}$$

and dislocation density

$$\rho_i^{\alpha} = \rho(t)^{\alpha} + \left(\kappa_1 \sqrt{\sum_{\beta\neq\alpha} \rho^{\beta}(t)} - \kappa_2 \rho^{\alpha}(t)\right) |\Delta\gamma_i^{\alpha}|, \tag{H.23}$$

from which the athermal strength $s^{\alpha}_{a_i}$ and the resolved shear stress τ_i^{α} can be calculated. The non-linear Eq.H.20 is solved using the Newton-Raphson method, where the shear increments are updated following $\Delta\gamma^{\alpha}_{j+1} = \Delta\gamma_j - J^{-1}_{\alpha\beta} f_j^{\beta}$ until the satisfied accuracy is reached and $f^{\alpha}(\Delta\gamma^{\alpha}_{j+1}) \approx 0$. As this step will consistently violate the mechanical equilibrium that has been predicted in the previous step, it is repeated for the updated value of stress but for the same time step Δt until the satisfactory tolerance is reached in mechanical equilibrium and $\|\boldsymbol{r}\| < \epsilon$. Analogically, the same algorithm is used for solving the fcc plasticity. The pseudo-codes of the algorithms outlined here are presented in Appendix I.

Appendix I. Pseudo-code for solving the governing elasto-plastic equations

The pseudo-code for solving the material model is presented in Alg.2. Due to the strongly non-linear nature of the constitutive equations, the solution is seeked through a sequence of linearized steps derived from the Newton-Raphson method. The input consists of the known value of the deformation gradient at the end of the time step $\boldsymbol{F}(\tau)$, and the values of plastic deformation gradient $\boldsymbol{F}^p(t)$, stress $\boldsymbol{\sigma}(t)$ and other internal variables $\alpha_i(t)$ at the beginning of the time step. The objective of the algorithm is to update these variables from t to τ, where $\tau - t = \Delta t$ is the time increment. The algorithm is constructed such that the set of non-linear equations is written as a function of the slip increments $\Delta\gamma^\alpha$ on individual slip systems α.

Algorithm 2: Pseudo-code for the constitutive model

Input: $\boldsymbol{F}(\tau)$, $\boldsymbol{F}^p(t)$, $\boldsymbol{\sigma}(t)$, $\alpha_i(t)$

/* Initial guess of amount of dislocation slip */

1 $\Delta\gamma_i^\alpha = \Delta\gamma_*^\alpha$

/* Newton-Raphson loop */

2 **while** $\epsilon < TOL$ **do**

3 $\quad f_i =$ `NonlinEq(`$\Delta\gamma_i$`)`

4 $\quad J_{kl} =$ (`NonlinEq(`$\Delta\gamma_k$`) - NonlinEq(`$\Delta\gamma_k + h_l$`)` $)/h_l$; $h_{l=k} = h$, othewrise $h_l = 0$.

5 $\quad \Delta\gamma_{i+1} = \Delta\gamma_i - \beta J_{kl}^{-1} f_l$

6 $\quad \epsilon = \|\Delta\gamma_{i+1} - \Delta\gamma_i\|$

7

/* Non-linear equation to be solved $f(x_i) = 0$ */

8 **Function** `NonlinEq(`$\vec{x}$`):`

9 $\quad \boldsymbol{F}^P = (\boldsymbol{I} + \sum_\alpha x^\alpha)\, \boldsymbol{F}^p(t)$; /* Update plastic deformation gradient */

10 $\quad \boldsymbol{F}^e = \boldsymbol{F}(\tau)\boldsymbol{F}^p$; /* Update elastic deformation gradient */

11 $\quad \boldsymbol{E}^e \leftarrow \boldsymbol{F}^e$; /* Update Green-Lagrange strain */

12 $\quad \boldsymbol{S}^{\mathrm{2PK}} \leftarrow \boldsymbol{E}^e$; /* Update second Piola-Kirchhoff stress */

13 $\quad \tau^\alpha \leftarrow \boldsymbol{S}^{\mathrm{2PK}}$; /* Update resolved shear stress */

14 $\quad f^\alpha = x^\alpha - \dot{\gamma}_0 \Delta t \exp\left\{ -\frac{G_0\left(1-\left(\frac{\tau^\alpha - s_a^\alpha}{s_t}\right)^p\right)^q}{kT} \right\}$

15 $\quad$ **return** f^α

Output: $\boldsymbol{F}^p(\tau)$, $\boldsymbol{\sigma}(\tau)$, $\alpha_i(\tau)$

The numerical version of the Newton-Raphson method for calculating the slip system increments $\Delta\gamma^\alpha$ is outlined in Alg.2 between lines 2 and 6. In some cases, a parameter $\beta \in \langle 0, 1\rangle$ may be introduced to improve the convergence characteristics by decreasing the step size. The more specific set of the non-linear equations in the form of a constitutive model (in this case, the model for bcc plasticity) is presented between lines 7 and 15. Note that the variables without t or τ represent the intermediate values as the solution converges to satisfy $f(\Delta\gamma^\alpha) = 0$. Once the required tolerance is reached, the final values are calculated. While the updated value of stress will satisfy the consistency conditions for plastic flow, it may not satisfy the mechanical equilibrium. In that case, the procedure needs to be repeated for an updated $\boldsymbol{u}$ which is outlined in Alg.3, but for the same time step Δt.

The pseudo-code for solving the equations of mechanical equilibrium at one loadstep is presented in Alg.3. Each loadstep is solved on the updated domain Ω which requires re-assembly of the stiffness matrix $\boldsymbol{K}$ as the mesh geometry has changed. Each loadstep is subdivided into a number of linear Newton-Raphson steps where the results converge to satisfy the mechanical equilibrium at the end of the loadstep. In this work, a modified Newton-Raphson method is used (Zienkiewicz et al., 2014), which does not update the tangent stiffness matrix at each Newton-Raphson iteration. Each loadstep consists of the given displacement constrain $\boldsymbol{u}^\Gamma$, and domain shape Ω. The Newton-Raphson method iterates until the force or displacement

norm is below the desired tolerance. The system of linear equations is solved using an iterative solver available in the open-source package Trilinos (Trilinos Project Team).

Algorithm 3: Mechanical equilibrium solver at one loadstep.

(1) Assemble stiffness matrix $\boldsymbol{K}$
(2) Assemble external forces $\boldsymbol{F}^{ext}$
/* Solve the non-linear problem using the modified Newton-Raphson method with the stiffness matrix $\boldsymbol{K}$: */
while *1* **do**
  (3) Calculate internal forces $\boldsymbol{F}^{int} = \mathcal{A}_i \int_{\Omega_i} \boldsymbol{B}^T \boldsymbol{\sigma} d\Omega_i$
  (4) Calculate forces due to prescribed displacement constraints $\boldsymbol{F}^{con} = \boldsymbol{K}_i \left(\boldsymbol{u}_i - \boldsymbol{u}_i^{\Gamma}\right)$
  (5) Assemble residual $\boldsymbol{R} = \boldsymbol{F}^{ext} + \boldsymbol{F}^{con} - \boldsymbol{F}^{int}$
  if $\|\boldsymbol{R}\| - \|\boldsymbol{R}^{i-1}\| < \varepsilon$ **then**
    break
  (6) Eliminate columns and rows of $\boldsymbol{K}\Delta\boldsymbol{u} = \boldsymbol{R}$ system corresponding to $\boldsymbol{u}^{\Gamma}$
  (7) Solve $\boldsymbol{K}\Delta\boldsymbol{u} = \boldsymbol{R}$ using an iterative solver
  /* Update displacement field moving closer to satisfying the mechanical equilibrium. */
  (8) $\boldsymbol{u}$ += $\Delta\boldsymbol{u}$
  (9) Calculate deformation gradient $\boldsymbol{F}(\tau) \leftarrow \boldsymbol{u}$
  /* Update stress for given material model (see Alg.2). */
  Input: $\boldsymbol{\sigma}(t)$, $\boldsymbol{F}(\tau)$, $\boldsymbol{F}^p(t), \alpha_i(t)$
  Output: $\boldsymbol{\sigma}(\tau)$, $\boldsymbol{F}^p(\tau)$, $\alpha_i(\tau)$
(10) Continue with the next loadstep ...

Appendix J. Effect of temperature and strain-rate

For comprehensive coverage, we briefly outline the predicted stress-strain curve results across varying loading rates and temperatures. To maintain brevity, we focus on three loading rates ($10^{-3}s^{-1}$, $10^{-4}s^{-1}$, $10^{-5}s^{-1}$) and two temperatures (300K, 77K), sufficient for offering the insights into the stress-strain trends. For an in-depth examination of the exponential kinetic law (refer to Eq.11) concerning temperature and loading rates, we recommend consulting the extensive analysis conducted by (Sedighiani et al., 2022).
The stress-strain curves, depicted in Fig.J.22, showcase results at high temperatures in red and at low temperatures in blue. Different style of curve is used to distinguish among different strain rates.

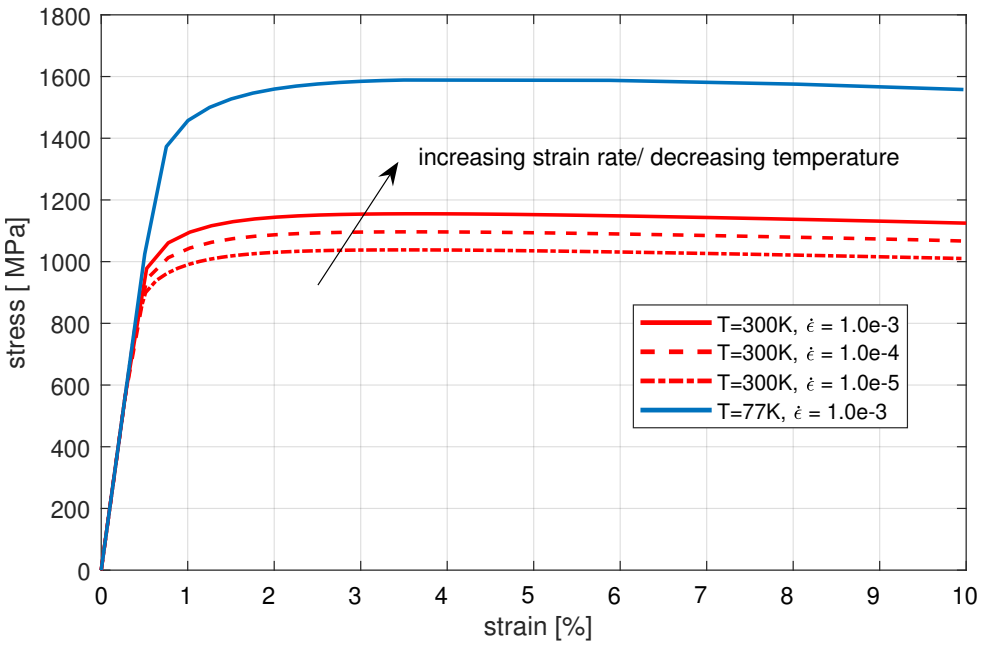


Figure J.22: Stress-strain curves presenting the effect of strain rate loading and temperature.

As anticipated, heightened loading rates and decreased temperatures correspond to elevated flow stress levels. No significant alterations were observed in stress or dislocation density patterns compared to prior sections.

Appendix K. Heat treated RVEs

A complete set of the simulation RVEs with a varying volume fraction of austenite at 5%, 10%, 15% , and 20% is presented below, depicting the changes in von-Mises stress, total dislocation density and lattice orientation at 10% of strain.

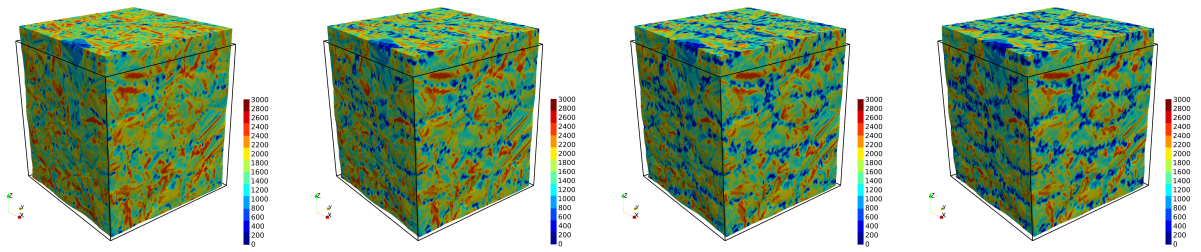


Figure K.23: Von-Mises stress [MPa] in RVEs with a varying volume fraction of austenite.

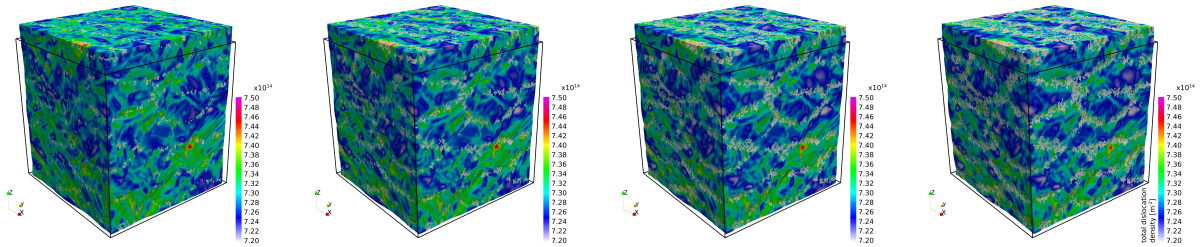


Figure K.24: Total dislocation density $\sum_\alpha \rho^\alpha$ [m^{-2}] in RVEs with a varying volume fraction of austenite.

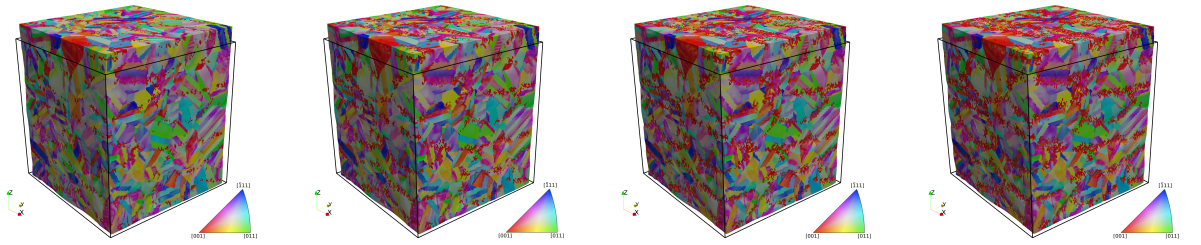


Figure K.25: Lattice orientation in RVEs with a varying volume fraction of austenite.